ResearchGate

See discussions, stats, and author profiles for this publication at: https://www.researchgate.net/publication/259465128

The Physical Oceanography of Long Island Sound

Chapter · January 2014

DOI: 10.1007/978-1-4614-6126-5

CITATIONS
10

READS
569

1 author:

James O'Donnell
University of Connecticut
99 PUBLICATIONS **3,259** CITATIONS

SEE PROFILE

Some of the authors of this publication are also working on these related projects:

ELIS Dredged Material Disposal SEIS View project

Estuary Plumes View project

All content following this page was uploaded by James O'Donnell on 27 December 2013.

The user has requested enhancement of the downloaded file.

Chapter 3
The Physical Oceanography of Long Island Sound

James O'Donnell, Robert E. Wilson, Kamazima Lwiza, Michael Whitney, W. Frank Bohlen, Daniel Codiga, Diane B. Fribance, Todd Fake, Malcolm Bowman and Johan Varekamp

3.1 Introduction

The ecology and geochemistry of Long Island Sound (LIS) are strongly influenced by the physical processes that determine the spatial structure and temporal evolution of the temperature (T), salinity (S), and DO concentrations and the distribution of the sediments. Much has been learned about these processes in the last decade through a combination of theoretical work, process studies, and the analysis of archived observations. The first wide-ranging summary of physical processes in LIS was published in 1956 by the Peabody Museum of Natural History at Yale University. Though the collection of papers mainly addressed biological oceanography, the chapter by Riley (1956) described the basic structure of the hydrography, tides, and currents, and much of his insight remains relevant. For the more general reader, Koppelman et al. (1976) provided a broad overview of the geological origin and geomorphology of LIS and summarized major characteristics of weather and climate. There has not been an extensive review of the literature since then. Reviews of the physical processes in neighboring water bodies are available.

J. O'Donnell (✉) · M. Whitney · W. F. Bohlen · T. Fake
Department of Marine Sciences, University of Connecticut, Groton, CT 06340, USA
e-mail: james.odonnell@uconn.edu

R. E. Wilson · K. Lwiza · M. Bowman
School of Marine and Atmospheric Sciences, Stony Brook University, Stony Brook, NY 11794, USA

D. Codiga
Graduate School of Oceanography, University of Rhode Island, Narragansett, RI 02882, USA

D. B. Fribance
Department of Marine Science, Coastal Carolina University, Conway, SC 29528, USA

J. Varekamp
Earth and Environmental Sciences, Wesleyan University, Middletown, CT 06459, USA

J. S. Latimer et al. (eds.), *Long Island Sound*, Springer Series on Environmental Management, DOI: 10.1007/978-1-4614-6126-5_3,
© Springer Science+Business Media New York 2014

In particular, the hydrography and circulation of the Middle Atlantic Bight are summarized by Mountain (2003) and Lentz (2008). A review of Block Island Sound (BIS) and Rhode Island Sound physical oceanography is given by Codiga and Ullman (2010) and corroborated and augmented with recent observations by Ullman and Codiga (2010). The physical processes in the Hudson River are summarized by Geyer and Chant (2006).

We begin with a description of the characteristics of the phenomena that have significant influence on the hydrography and circulation: the freshwater discharge, the wind and wave climate, and the tides. In Sect. 3.2, we then describe the evolution (on time scales longer than tidal) and structure of the *T*, *S*, and density distributions in the Sound using a broad array of datasets. The magnitude and structure of the residual circulation are summarized in Sect. 3.3 and evidence for seasonal variations is summarized in Sect. 3.4. In Sect. 3.5, we discuss the effects of wind on sea level and circulation. In Sect. 3.6, we review recent observational and theoretical work on the physical processes that influence the duration and extent of hypoxia. Hypoxia, low concentrations of DO, develops in the deeper waters of the western Sound every summer and the impacted region spreads eastward as summer progresses. The data records resulting from water quality monitoring programs are now several decades long and in Sect. 3.7, we summarize some characteristics of long-term changes that can be detected. In Sect. 3.8, we outline the characteristics and magnitude of the response of the Sound to severe storms and comment on the likely impact of climate change. In the final section, we summarize and comment on the main results of the review.

3.1.1 Freshwater and Saltwater Sources

LIS is often described as an estuary because it is significantly fresher than the adjacent shelf water of southern New England. But it is an atypical mid-latitude estuary in several ways. First, it is unusual that the largest freshwater tributary discharges into the estuary near the main connection to the ocean. Gay et al. (2004) summarized the long-term average discharge of the seven rivers entering the Sound (see Table 3.1). The Connecticut River is the dominant source of fresh water and contributes 75 % of the total gauged discharge. Gay et al. (2004) also pointed out that there is a distinct seasonality to the flow rates. Since the extensive watershed of the Connecticut River includes the mountains in New Hampshire and Vermont, which accumulate precipitation as snow and ice throughout the winter, there is a large freshet in the spring. Figure 3.1 shows that the mean monthly flow in March, April, and May all exceed the annual average flow and the mean April discharge is more than twice the average.

The mechanisms that lead to dispersal of the effluent from the Connecticut River are quite complex. This was the subject of a series of reports by Garvine (1974, 1975 and 1977). With ship surveys and drogue studies, he showed that a large area of ELIS was covered by a thin (2 m) surface layer of brackish water that

Table 3.1 Principal rivers entering LIS as Gauged by the USGS

USGS site name	USGS site number	Gauged area, square miles	1931–2003 mean flow (m^3/s)	1995–2001 mean flow (m^3/s)
Housatonic River at Stevenson, CT	01205500	1544	84	79
Naugatuck River, Beacon Falls, CT	00196500	115	14	15
Quinnipiac River at Wallingford, CT	01184000	9660	7	6
Connecticut River, Thompsonville, CT	01127500	89	545	508
Yantic River at Yantic, CT	01127000	404	5	5
Quinebaug River at Jewett City, CT	01122500	713	37	37

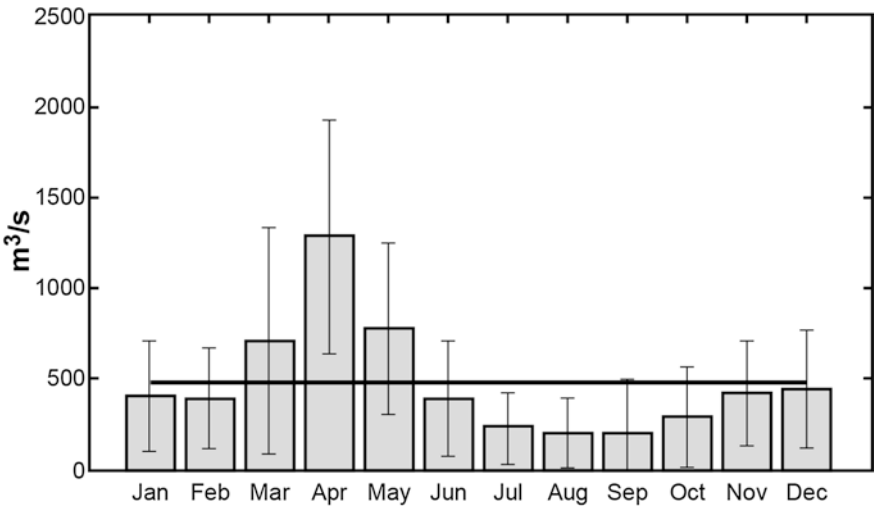

Fig. 3.1 Mean and standard deviation of the mean monthly discharge in the Connecticut River measured at Thompsonville, CT. The horizontal line shows the long-term mean

was separated from the Sound water by a line of foam and detritus, referred to as a front. This river plume was observed to be strongly influenced by the tidal flow in the Sound. On the ebb tide, the front was located to the east of the river mouth and to the west on the flood. During high flows, the front could be tracked almost to The Race. O'Donnell (1997) and O'Donnell et al. (1998, 2008a, b) have made detailed measurements of the structure and motion of water near the front and the mixing rates between the plume and Sound. It is likely that these near field processes affect the distribution and fate of the river water, but the small scales and transient character have made their inclusion in Sound-scale models impossible.

There is substantial inter-annual variation in the discharge of the river that is driven by regional scale meteorological variability, and Whitney (2010) has shown that the Connecticut and several other rivers of the eastern United States correlate with the North Atlantic Oscillation (NAO) index (Hurrell 1995). Using the same record, O'Donnell et al. (2010) showed that the day of the year by which 50 % of the annual discharge has passed the gauge, the "center of volume flow," has become earlier at a rate of 9 $\pm$ 2 days/century. It is consistent with the analysis of unregulated New England rivers and streams reported by Hodgkins et al. (2003) that the fresh water stored in the winter ice and snow pack arrives at the ocean through the Connecticut River earlier than in the past and is, therefore, likely to be a consequence of regional meteorological fluctuations rather than changes in watershed management.

A second unusual feature of the Sound is its connection to the estuary of the Hudson River by a tidal strait known as the East River. This causes the Sound to have two connections to the ocean and allows Hudson River water to enter the Sound. The magnitude and variability of the volume and salt fluxes through the East River to the Sound are not well established. The characteristics of the barotropic tidal flow have been described by Jay and Bowman (1975) who showed that the flow in the East River is determined by the phase and amplitude of the sea level imposed at the ends by the ocean and LIS tides, and by frictional processes at the seabed. Wong (1991) considered a broader range of frequencies and showed that though the East River filtered out tidal frequency oscillations, meteorologically forced motions at low frequencies propagated with little damping.

Blumberg and Pritchard (1997) combined direct current measurements and the results of a sophisticated three-dimensional numerical model to estimate the volume flux through the East River. They reported a net westward (toward New York Harbor) mean volume flux of 310 m^3/s that was the difference between an eastward transport of surface water of 260 m^3/s and lower layer flow of 570 m^3/s. The model results (see Fig. 3.2) also showed that these upper and lower layer transports had substantial variation (150 m^3/s) with maxima in the winter. The variations in the two layers are negatively correlated with the result that the net westward transport only varies by 50 m^3/s.

Gay et al. (2004) developed a salt budget model for LIS that exploited an extensive archive of *S* measurements to estimate salt fluxes through the East River and The Race that were consistent with the *S* data and the Blumberg and Pritchard (1997) results. They concluded that salt was transported out of LIS into New York Harbor at a rate of 11,000 kg/s. This tends to freshen the western end of the Sound. Crowley (2005) also developed a circulation model that assimilated *S* and *T* observations in the Sound and used it to estimate the salt flux and freshwater flux. Her estimate of the average salt flux over the period April through September 1988 was 16,000 kg/s and the average freshwater flux was 150 m^3/s. This is a substantial flux, comparable to that of the major rivers except the Connecticut.

The model and analyses of Crowley (2005) also further our understanding of the relative importance of mechanisms contributing to the longitudinal flux of salt in LIS. She found, for example, that westward salt flux associated with the Stokes transport dependent on the phase relationship between tidal surface elevation and

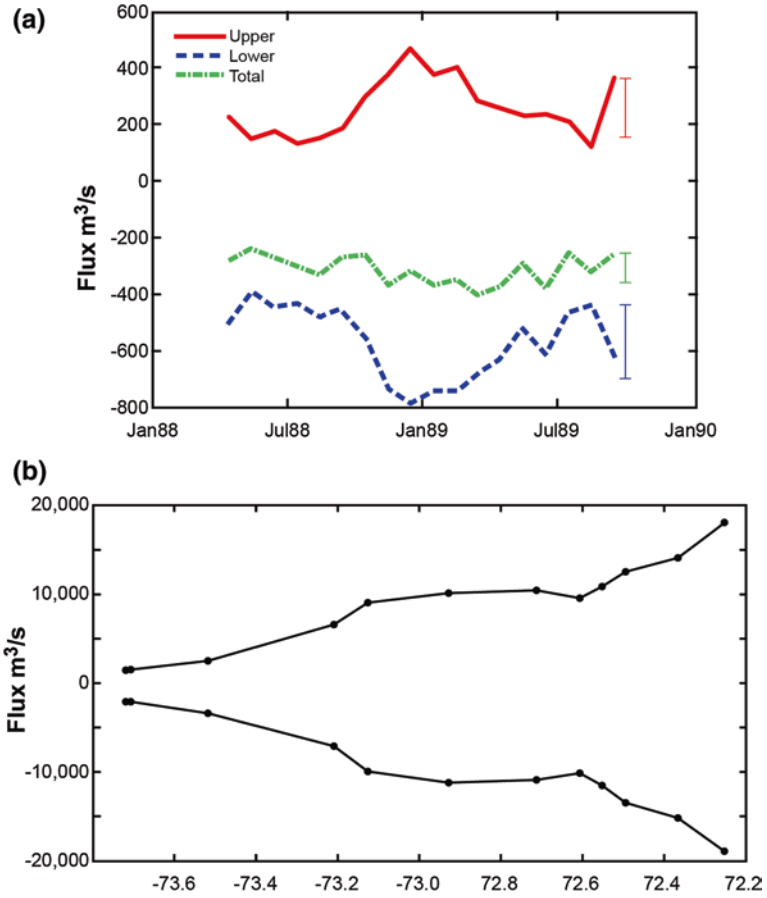

Fig. 3.2 **a** Seasonal variation of the volume fluxes through the East River from the model of Blumberg and Pritchard (1997). *Blue* shows the lower layer transport to the east and the *red* shows the counter flow in the surface layer. *The green* line shows the net transport. **b** The mean (April–September) volume exchange as a function of distance along the Sound. Redrawn from Crowley (2005)

tidal current made a substantially larger contribution to the total westward salt flux than the gravitational circulation. In a typical estuary, the upstream Stokes transport tends to be balanced by a downstream barotropic transport. In LIS, because of the unique boundary condition at the western end, that is not the case.

The largest volume exchange between LIS and surrounding water bodies occurs at the eastern boundary of the Sound through The Race. Riley (1956) used salt and drift pole observations to argue that the volume exchange in the eastern Sound was approximately 15,000 m^3/s. This estimate ignored shear flow dispersion by tidal currents. Gay et al. (2004) allowed both dispersion and advection, and found that the exchange flow required to balance the salt budget was 25 % of Riley's estimate. Using 2 years of direct current observations from a vertically profiling acoustic current meter mounted on a ferry

that crossed the eastern Sound approximately eight times a day during a 3-year interval (see Codiga 2007), the annual mean nontidal volume exchange was estimated by Codiga and Aurin (2007) to be 22,700 ± 5,000 m^3/s. Codiga and Aurin (2007) suggested the low value of Gay et al. (2004) was a consequence of their parameterization of the variation of the transport coefficients using a power law dependence on freshwater inputs, or the inadequate representation of the lateral variations. The along-Sound variation of the positively and negatively directed volume fluxes in the model of Crowley (2005) is shown in Fig. 3.2b. At the western end of the domain, the fluxes are comparable to those of Blumberg and Pritchard (1997). At the eastern end, the values are much larger, 17,000 m^3/s which is closer to the Riley (1956) estimate than that of Gay et al. (2004). Figure 3.2b also shows that along-Sound volume fluxes decrease rapidly from east to west in the eastern Sound and are only ~10,000 m^3/s at −72.6°. Mau et al. (2008) and Hao (2008) recently developed models that followed the approach of Crowley (2005) and assimilated *S* and *T* measurements to predict the subtidal currents, fluxes, and values at the eastern end of the Sound. These also show general agreement with the Riley (1956) and Codiga and Aurin (2007) estimates. However, since the observations of Codiga and Aurin (2007) are in a region of rapid spatial variation in volume transport, and since there is an absence of salt flux estimates with which to evaluate the assimilative models, much remains to be learned about the flow and rates of exchange of materials between the Sound and adjacent waters.

Additional uncertainties in the freshwater budget of the Sound arise from lack of information about the rates of evaporation and precipitation. The maps of annual evaporation and precipitation rates in New England created by Krug et al. (1990) by integrating a diverse array of measurements suggest that there is a net delivery of fresh water at a rate of 0.5 m/year in coastal Connecticut. Assuming this rate applies over LIS leads to an approximate volume flux of 50 m^3/s. Using well level measurements and a groundwater flow model, Buxton and Smolensky (1999) estimated that the delivery of fresh water to the Sound from deep and shallow aquifer systems was 109 m^3/s. The magnitudes of these two sources are comparable to the discharge from the Housatonic River and 10–20 % of that of the Connecticut River. In their salt budget, Gay et al. (2004) assumed that the precipitation-evaporation fluxes were approximately in balance and that the groundwater flux was small. Though uncertainties of this magnitude may be tolerable for some purposes, the waters of New York Harbor, the New England shelf, and subsurface aquifers contain solutes (e.g., nitrate) at much different concentrations than those in the Sound and the volume exchanges consequently play a much larger role in those budgets. The improvement of estimates of these fluxes through direct measurement deserves attention.

3.1.2 Wind and Waves

Stress generated by wind at the surface of the ocean has a major influence on the circulation and rate of vertical mixing. Winds also generate surface gravity waves that influence sediment resuspension and the magnitude of the bottom stress on lower frequency motions (Signell et al. 2000; Wang et al. 2000). LIS

lies in the westerlies but there is a distinct seasonality to the statistical characteristics of winds (Isemer and Hasse 1985). Using all long-term land station data archived by the National Climatic Data Center (NCDC, see http://www.ncdc.noaa.gov/oa/ncdc.html), Klink (1999) showed that the monthly mean surface wind velocity vectors in southern New England were directed to the southeast in winter and to the northeast in summer with much lower speeds. Lentz (2008) analyzed records of wind observations from five National Data Buoy Center (NDBC) buoys and six bottom attached towers and masts spanning the Middle Atlantic Bight (MAB). He reported seasonal trends in velocity that were consistent with Klink's continent-scale pattern. Additionally, his analysis of the wind stress revealed a MAB-wide annual mean of 0.02–0.03 Nm^{-2} directed toward the southeast with an annual amplitude cycle 0.03–0.04 Nm^{-2} in the same direction. This reinforces the mean across-shelf stress in the winter and opposes it in the summer. He also showed that the stresses at the buoys were more than twice those estimated at the coastal sites.

In the area of LIS, there are few long series of wind measurements. The longest record available in the NCDC archive is at Bridgeport (Sikorsky Memorial Airport), which has been in operation since 1942 and is located close to the shore and near the center of LIS (see Fig. 3.3a). Most analyses of the response of the Sound to winds have used this dataset or measurements at another regional airport. They assumed that the velocity can be extrapolated over water, and then estimated the wind stress with a bulk formula like that of Large and Pond (1981). Recently, over water observations have become available from the Long Island Sound Integrated Coastal Observing System (LISICOS) (http://lisicos.uconn.edu) at the Execution Rocks (EXRK), western and central Long Island Sound (WLIS and CLIS) buoys. The locations of these buoys are shown in Fig. 3.3a. Howard-Strobel et al. (2006) presented wind roses using the CLIS buoy observations. Here we summarize a more extensive record and provide a comparison of the statistical character of wind forcing over the central and western Sound.

Figures 3.3b and c show the annual mean wind stress vector components computed from hourly measurements of velocity at Sikorsky Airport (Bridgeport) and the WLIS and CLIS buoys for the period January 1, 2004 to December 30, 2009. The red symbols show the mean and 68 % confidence interval at the CLIS buoy assuming a three-day autocorrelation time scale (see Emery and Thompson 1997). The blue and green symbols show the components at the WLIS buoy and Bridgeport. The seasonal cycle is clear in the components of all three records. The monthly mean wind stress is weak from April to September and has a maximum magnitude in February of 0.07 Nm^{-2} toward the southeast at the CLIS buoy. Note that the amplitude of the cycle at the CLIS site is 0.04 Nm^{-2}, in agreement with the intra-annual variations in the MAB estimated by Lentz (2008). The means and the amplitude of the annual cycle at the WLIS buoy and Bridgeport are approximately 60 and 30 %, respectively, of the value at the CLIS buoy. The annual means, shown in Fig. 3.3a by the red arrows, are dominated by the winter conditions, which are shown in blue. Note that the orientations of the vectors (~125 *T*) at the three sites are consistent. They are also consistent with the southeasterly directed means computed throughout the MAB by Lentz (2008). However, the CLIS and

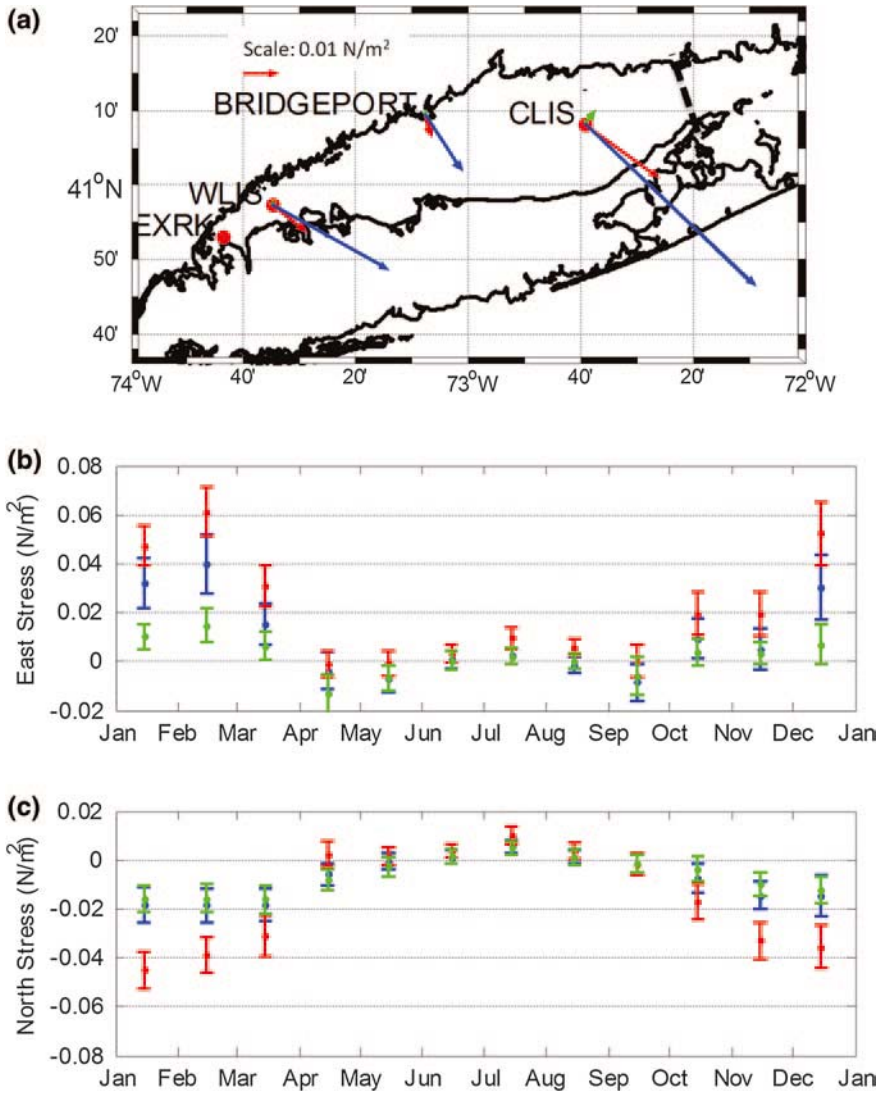

Fig. 3.3 **a** A map of the coastline of LIS showing the locations of the EXRK, WLIS and CLIS buoys, and Bridgeport Airport. The *red*, *blue*, and *green* vectors show the annual, the winter, and summer mean stress vectors. The *dashed line* shows the approximate track of the Bridgeport-Port Jefferson Ferry. **b** and **c** show the monthly mean east and north stress components for the period January 2004–December 2009 together with their 68 % confidence interval at Bridgeport, CT (*green*), WLIS (*blue*), and CLIS (*red*)

WLIS magnitudes, 0.026 and 0.012 Pa, are significantly different. It appears that the wind forcing of the central Sound at seasonal time scales is equivalent to that of the MAB shelf. It is also clear that the waters of the western Sound experience less stress as estimated by the parameterizations developed for ocean conditions.

The spatial scale over which the boundary layer adjusts to the surface stress imposed by the water remains unclear since there are few direct measurements of stress variation. Lentz (2008) noted that the stations closer to shore in the MAB showed reduced mean wind velocities and suggested that scale for the influence of land was less than 10 km. Our finding that the energy in the across-Sound stress at the buoy further from shore (CLIS) is much larger than that at the WLIS buoy is consistent with his result.

Mooers et al. (1976) demonstrated that synoptic scale weather systems dominate the variability in the wind, pressure, and precipitation in the MAB and that they can drive significant currents in LIS. Figure 3.4a and c show the winter and summer autospectra, $S_{\tau_{xr}}$, of the along-Sound (70° *T*) projection of the wind stress vector, τ_{xr}, estimated from velocity measurements at the CLIS (red) and WLIS (blue) buoys for the period 2004–2009 using the parameterization of Large and Pond (1981). The spectra, $S_{\tau_{yr}}$, of the across-Sound wind stress component, τ_{yr}, in winter and summer are shown in Fig. 3.4b and d. The spectra were computed using the Welch method (see Emery and Thompson 1997) with a Hanning window

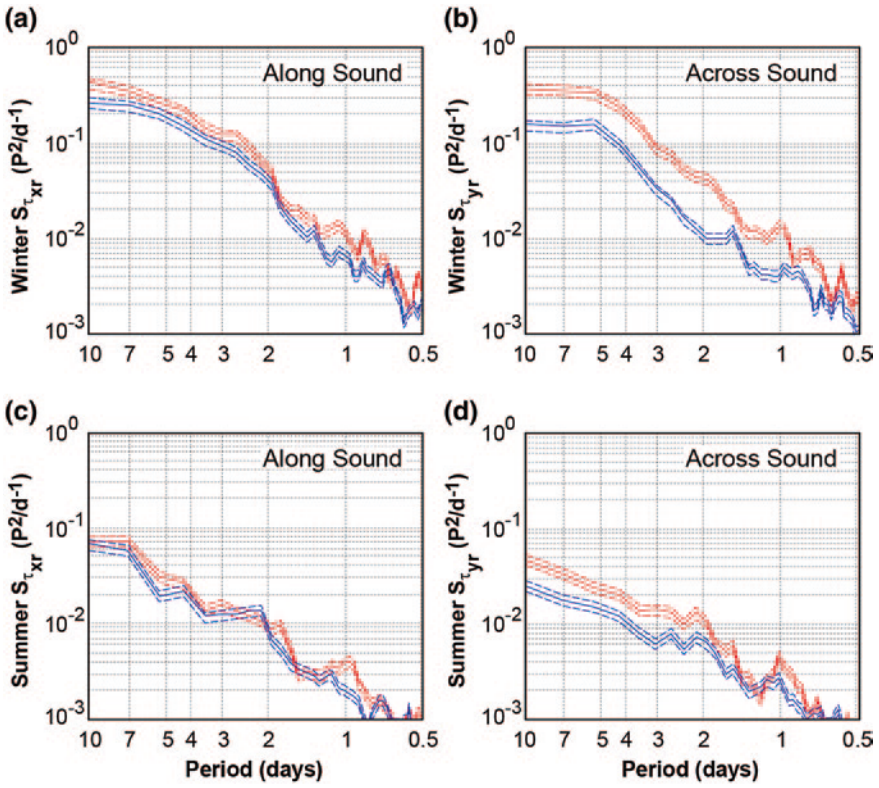

Fig. 3.4 The spectra of along- and across-Sound stress components. **a** and **b** Show the winter time spectra for the along-Sound components. **c** and **d** Show the same quantities for summer. In all graphs, *blue* represents the WLIS and *red* the CLIS spectra

and all possible 512 h nonoverlapping segments with less than 5 % data loss and no data gaps longer than 2 h. Short gaps were filled by linear interpolation. The spectra have a bandwidth of 0.47 days^{-1} and 62° of freedom.

All spectra show that energy in the 2–10 day (synoptic) band is an order of magnitude higher than at shorter periods as is typical in the mid-latitudes. By comparing Fig. 3.4a–d, it is clear that the magnitude of $S_{\tau_{xr}}$ at CLIS (red) and WLIS (blue) during both summer and winter is more alike than for $S_{\tau_{yr}}$. The width of the Sound appears to have a greater effect on the across-Sound wind stress. The stress fluctuations at the WLIS buoy are generally a factor of two to four less energetic than those at the CLIS buoy, with the exception of $S_{\tau_{xr}}$ in the summer (Fig. 3.4c) when they are of comparable magnitude. In the synoptic band, the coherence between the WLIS and CLIS buoys (not shown) is also high, greater than 0.6, as is to be expected since the synoptic weather systems are much larger scale than the separation of the buoys. At shorter periods, the coherence drops to less than 0.3. We conclude that though the mean and long-period fluctuations in the wind stress over the Sound are spatially coherent with larger amplitudes near CLIS, a large fraction of the variance at and below the daily period is not. The study of processes that are sensitive to high frequency variations in the wind (e.g., sea breezes) and their consequences will require local observations to resolve the spatial variability in this frequency range.

Figure 3.5 shows the frequency distribution of wind direction observed at LaGuardia Airport, New York during July and August using data from 1960 to 2010. There are three distinctive summertime wind direction regimes. The predominant direction is centered on approximately 180°. This is associated with

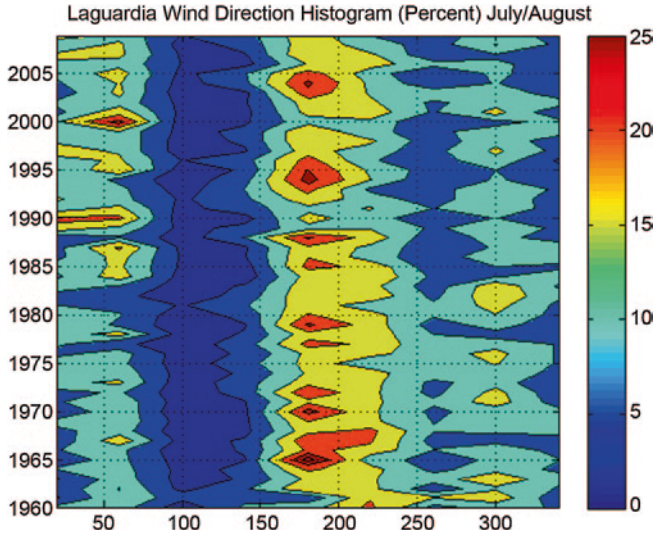

Fig. 3.5 LaGuardia Airport wind direction histogram for July and August for 1960–2010

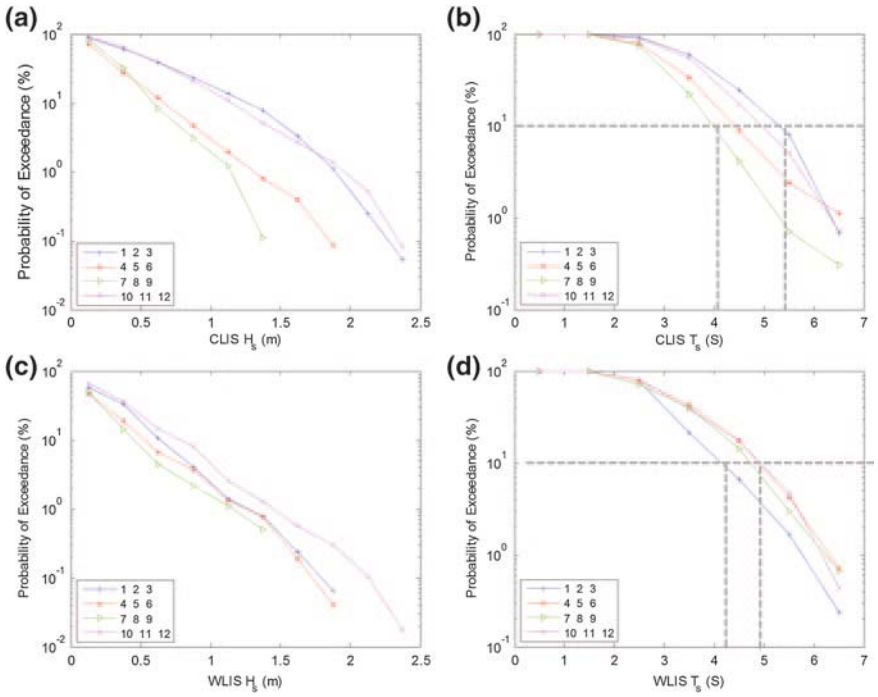

Fig. 3.6 Seasonal variation in the probability of exceedance, expressed as a percentage, for significant wave heights and periods at the CLIS, **a** and **b**, and WLIS sites, **c** and **d**. Data from January to March is shown by *blue lines* and '+' symbols; October–December by *magenta* with 'x' symbols; April-June by *red lines* and '*' symbols; and July to September by *green lines* and *triangles*

summertime ridge and trough systems. These winds are interrupted by intervals of wind from the northeast and northwest. Analyses of available NOAA historical daily weather maps indicate that northeast winds over the western Sound in the summer are typically associated with hybrid systems with low pressure to the southeast of the Sound and a high to the northwest. Northwest winds arise when a low is to the northeast of the Sound and a high is to the southwest.

There are few published observations of the characteristics of the wave height and period in LIS. Bokuniewicz and Gordon (1980a and b) and Signell et al. (2000) have made estimates of the wave-induced bottom currents using the predictions of fetch limited wave models to interpret patterns of sedimentation, but direct measurements with which to evaluate the performance of the models have been limited. Rivera Lemus (2008) provided a brief summary of the wind and wave climatology using a year-long interval of data from the LISICOS CLIS buoy. However, a much longer record has been established and we describe the observations from 6 years of observations of a three-axis directional wave gauge at the CLIS buoy and a single axis sensor at WLIS. Here we briefly summarize

statistics of the observations and outline a simple explanation for the structure and variability.

To summarize the data, we define $f_H\left(H_{s,j};\, M_i\right)$ as the fraction of hourly significant wave height observations obtained during the set of months $M_{i\in[1:12]}$, in the interval $H_{s,j} - \delta H < H_s < H_{s,j} + \delta H$. We then estimate the probability that an observation will exceed $H_{s,j}$ as $P\left(H_{s,j};\, M_i\right) = 1 - \sum_{k=1}^{j} f_H\left(H_{s,k};\, M_i\right)$. The probability that the significant wave period will exceed is computed in an analogous manner. The probability of exceedance, $P\left(H_{s,j};\, M_i\right)$ for $M_{i=\{1,2,3\}}$, expressed as a percentage, for significant wave height during January–March at CLIS is shown by the blue line in Fig. 3.6a. The distribution closely follows that for $M_{i=\{10,11,12\}}$, October–December, which is plotted in magenta. The spring and summer distributions at CLIS are also similar to each other. Note that even with 6 years of data, there are few estimates of high H_s values and extrapolation is frequently employed to estimate the probability of very large values for engineering design applications. It is clear from the data, however, that the frequency of large waves is much higher in the October–March period. In fact, for much of the range of H_s, the probability of exceeding a particular value is a factor of 10 higher in the winter. $P\left(H_{s,j};\, M_i\right)$ for WLIS is shown in Fig. 3.6c. It does not display as strong a seasonal variation as observed at CLIS though the probability of exceeding a particular H_s is at least a factor of two larger in October–December than in June–August.

The probability of exceedance of the significant wave period, $P\left(T_{s,j};\, M_i\right)$, is shown in Fig. 3.6b and d for CLIS and WLIS, respectively. At CLIS, the seasonal variation is similar to that displayed in the H_s graph. In the summer, June–August, T_s is less than 4 s in 90 % of observations and in winter, January–March, the periods generally are longer with 90 % of observations less than 5.3 s. At WLIS (see Fig. 3.6d) only $P\left(T_{s,j};\, M_i\right)$ for January–March is anomalous and wave periods are shorter than in the summer.

A short example of the time series of wind stress vector components and H_S from the LISICOS buoys during December 2007 is shown in Fig. 3.7a and b. The black line in Fig. 3.7b shows the evolution of H_S at CLIS and the red line shows the variation of H_S at WLIS. Examination of the wave heights series in Fig. 3.7b reveals high correlation. However, there are intervals when the wave heights are almost identical. Some examples are indicated by arrows in Fig. 3.7b. At other times H_s at WLIS is only half of that at CLIS. As has been shown previously, the components of the wind stress at WLIS and CLIS are clearly coherent with each other at longer periods, so it is not immediately obvious why there are differences in the wave heights at the two buoys. The gray points in Fig. 3.8a show the relationship between the mean significant wave height, $\bar{H} = (H_{SW} + H_{SC})/2$, and the along-Sound component of the wind stress at CLIS, τ_{xr}, using all observations between January 2004 and December 2009. The error bars show the median and 68th percentile range of $\bar{H}$ in 0.05 Nm^{-2} intervals of stress. Though there is considerable scatter in the data, the trend is for $\bar{H}$ to increase symmetrically with the magnitude of τ_{xr}. Figure 3.8b shows the dependence of the difference in wave height, $\Delta H = H_{SC} - H_{SW}$, on τ_{xr}. As in Fig. 3.8a, the data are shown by the gray dots,

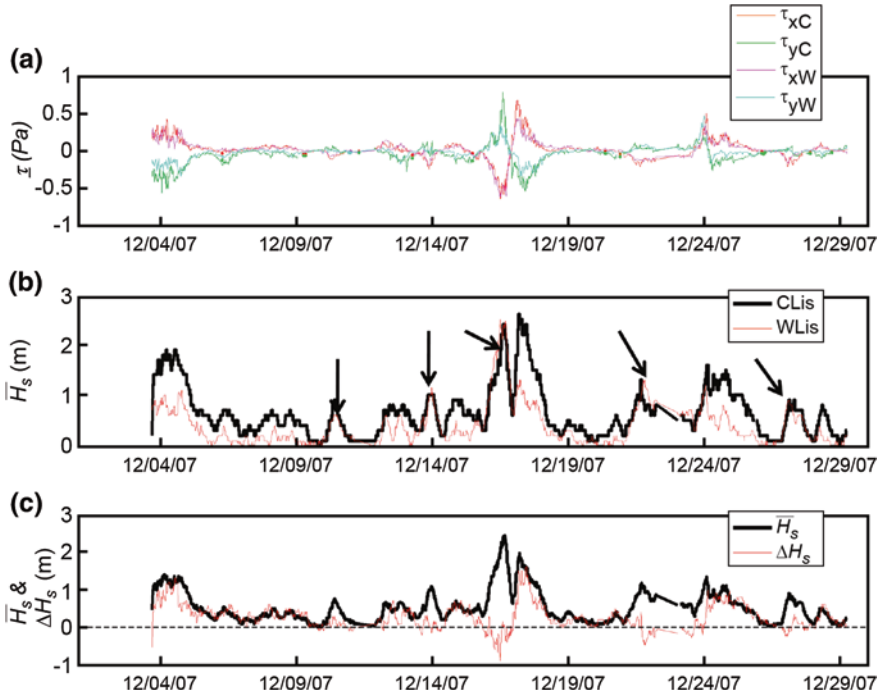

Fig. 3.7 **a** Time series observations of along (*red*) and across (*green*) stress at the CLIS buoy. The *magenta* and *blue lines* $\bar{H}_s = (H_{SW} + H_{SC})/2$ how the corresponding quantities at the CLIS site. **b** The significant wave height at CLIS (*black*) and WLIS (*red*). **c** The average (*black*) and difference (*red*) in the wave heights at CLIS and WLIS

and the median and 68th percentile intervals are shown by the error bars. Though positive along-Sound wind stress observations are more common, it is clear in Fig. 3.8b that wave heights are larger at CLIS when stress is positive (i.e., the wind is from the west southwest). During periods of strong winds, the waves in CLIS can be 1 m larger than at WLIS. In contrast, when the stress is negative (i.e., winds from the east northeast), the waves are the same. Figure 3.8c shows the influence of the across-Sound wind stress, τ_{yr}, on ΔH. Strong winds from the south are infrequent in southern New England, so most of the data in Fig. 3.8c is for $\tau_{yr} < 0$ It is clear, however, that $|\Delta H|$ increases with $|\tau_{yr}|$ and that the wave height at CLIS increases relative to WLIS with the magnitude of the across-Sound stress component.

Like the wind at short periods, the wave climate in WLIS is quite different from that in the central Sound. There is also significant seasonal variation that has higher amplitude in the central Sound. Waves generally have larger amplitude and longer period in the central Sound, especially in winter. In the western Sound, waves are largest when the winds are easterly (with a negative, or westward, along-Sound stress component) and H_s is comparable to that in the central Sound. As pointed out by Bokuniewicz and Gordon (1980a, b), (Signell

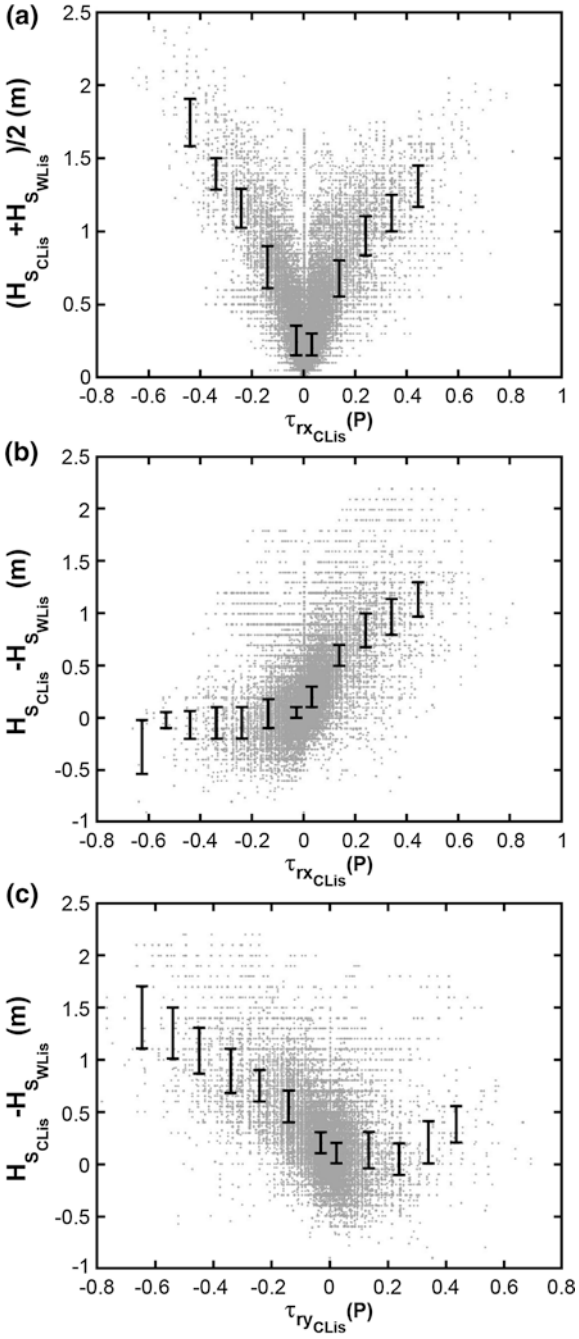

Fig. 3.8 **a** The *gray* points show mean of the significant wave height at WLIS and CLIS, dependence on the along-Sound component of the wind stress at CLIS, τ_{xr}, using all observations between January 2004 and December 2009. The error bars show the median and 68th percentile range of $\bar{H}$ in 0.05 Nm^{-2} intervals of stress. **b** The dependence of the difference between the significant wave height observations at CLIS and WLIS, $H_{SC} - H_{SW}$, on the mean along-Sound component of the wind stress. **c** The dependence of the $H_{SC} - H_{SW}$ on the mean across-Sound component of the wind stress at CLIS

et al. 2000), and Rivera Lemus (2008), the dependence of waves on wind in LIS is largely consistent with the fetch limitation theory of Sverdrup and Munk (1946) and Bretschneider (1952). The difference between the response of wave in the western and central Sound is also consistent with this idea. When the wind is from the east, the fetch at both buoys is large and the wave statistics are similar. For all other directions, the fetch at the WLIS buoy is much smaller than at CLIS and so are the waves.

3.1.3 Tides

The dominant cause of motion of water in the Sound is the barotropic pressure gradient force created by sea level fluctuations on the adjacent continental shelf. Observations of sea level made by Le Lacheur and Sammons (1932), Redfield (1950), and Koppleman et al. (1976) showed that the amplitude of sea level fluctuations at the semidiurnal frequency increased by a factor of three from The Race in the east to Kings Point in the west. A simple mathematical model developed by Redfield (1950) suggested that this was because the length of the Sound was close to a quarter of the wavelength of the semidiurnal tidal wave and, therefore, the basin was near resonant at the semidiurnal frequency. The first comprehensive description of the tides in LIS was summarized by Swanson (1976) and his results were broadly consistent with the simple theory. Ianniello (Ianniello 1977a and b) extended the model approach adopted by Redfield (1950) to include the effects of the main characteristics of the basin geometry and predicted the along-Sound variation and vertical structure of the laterally averaged current and sea level amplitudes. Using the model, he investigated the impact of several plausible assumptions about the structure of the vertical eddy viscosity on the structure of the tidal currents, but the data available were inadequate to eliminate any of the possibilities. However, Ianniello's model showed that the mean flow driven by periodic tides might have comparable magnitude to that expected to be driven by baroclinic pressure gradients. This approach was extended to include the effects of lateral depth variations on the vertically averaged flow by Li and O'Donnell (1997 and 2005). Recently, Winant (2007) unified these theories in a concise framework that describes the three-dimensional circulation driven by barotropic tides.

Swanson's (1976) description of the variation of phase in the western Sound and the East River, and the demonstration of the effect of winds on sea level predictions using harmonic analysis, prompted the development of the much more sophisticated two-dimensional numerical models of Murphy (1979) and Kenefick (1985). Though these models were very successful in simulating sea level variations, current observations were only available in a few locations and were inadequate to critically assess the predictions of the spatial structure of the velocity amplitudes. The numerical approach to the solution of the vertically averaged equations was extended by Bogden and O'Donnell (1998) to include the capability to assimilate current meter observations to predict tidal and meteorologically

forced circulation in a segment of the central Sound. Using models and observations, they demonstrated the existence of significant across-Sound structure in the vertically averaged circulation that they attributed to wind forcing. Practical demands for predictions of the transport and fate of materials in the Sound, together with the development of acoustic Doppler current profilers (ADCPs), prompted the development of three-dimensional circulation models (see Valle-Levinson and Wilson 1994a and b; Valle-Levinson et al. 1995; Schmalz 1993; Blumberg et al. 1999; and Signell et al. 2000).

Recently, Hao (2008) extended the study of Crowley (2005) and Wilson et al. (2005) who implemented the Regional Ocean Modeling System (ROMS) (see Shchepetkin and McWilliams 2005) for the Sound and reported the results of a comprehensive analysis of the dynamics of the tidal circulation. Hao (2008) applied scaling arguments based on the three parameters introduced by Winant (2007) in his barotropic theory for frictional tidal flow in basins with topography: the basin aspect ratio $\alpha = \frac{B}{L}$, a friction parameter $\delta = \left(\frac{2K}{\omega H^2}\right)^{1/2}$, which is the ratio of the amplitude of the periodic boundary layer thickness to water column depth, and the ratio of basin length to tidal wavelength $\kappa = \frac{\omega L}{\sqrt{gH}}$. Using these parameters and scales appropriate for LIS, she argued that the longitudinal and lateral tidal-period momentum balances were fundamentally different. The lateral tidal-period balance was between acceleration, Coriolis force associated with the vertically sheared longitudinal current, and barotropic pressure gradient. This leads to tidal-period lateral circulation that is clockwise on flood and anti-clockwise on ebb as shown in Fig. 3.9. Since this circulation pattern may result in a transport of DO from the shallow, nearshore areas to the hypoxic deep water of the western Sound, these predictions deserve careful comparison with observations in the near future.

Bennett et al. (2010) reported observations of the vertical structure of the principal tidal constituents in LIS using long deployments of ADCPs at 11 sites and the analysis approach of Pawlowicz et al. (2002). They identified the tidal constituents that were dominant at each station and described their vertical structure. The results were presented in tables that should be used in the future to evaluate models and guide improvements to realistic simulations. Figure 3.10 shows the locations of the current meters and the near surface and near bottom major and minor axes of the M2 (lunar semidiurnal) tidal current ellipses, the largest harmonic at all sites. In the eastern Sound (see Fig. 3.10a), the observation reveals strong M2 major axis amplitudes oriented along the axis of the Sound at the surface and parallel to isobaths near the bottom. At the ADCP, labeled m03 in Fig. 2.10a, the near surface major axis amplitude of the M2 was 0.9 m/s. The other semidiurnal constituents, N2, S2, and L2, were 0.19, 0.12, and 0.08 m/s, respectively. The superposition of these harmonics leads to a large spring-neap variation, which Valle-Levinson and Wilson (1994a) described at a site slightly to the south of station M3. They also proposed that the relative importance of turbulent stresses in the tidal dynamics was substantially different at spring and neap stages.

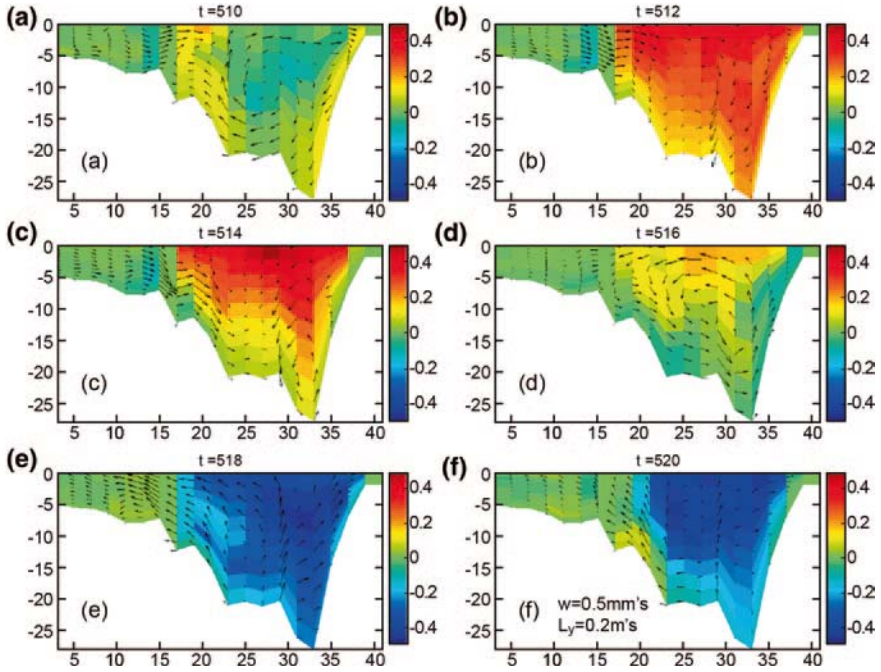

Fig. 3.9 Evolution of predicted along-Sound velocity component (*color shading*) and the velocity vector components in the across-Sound plane (*arrows*) in the central Sound at spring tide. **a** shows the flow at simulation hour and **b**–**f** show the structure at 2 hour intervals. The velocity units are m/s and the scale for the vectors is shown in panel (**f**)

At the stations shown in Fig. 3.10a, the phase variation in the M2 constituent in the horizontal is very small with currents at the shallower sites leading those in deeper water, a consequence of the increased relative importance of bottom friction. The variation in the M2 phase among the near surface records at stations M02, M03, and M06 is only 6°. However, at station M05 in the shallow water north of Long Sand Shoal, the M2 phase is advanced at all depths by 20° or 40 min. The observed weak phase variation along the Sound is consistent with the idea that the tide is almost a standing wave.

In the western Sound, the M2 constituent is also the dominant harmonic, and the major and minor axes of the near surface and bottom M2 ellipses are shown in Fig. 3.10b. Note that the scale is different from Fig. 3.10a and that the current amplitude is much smaller. At the ADCP labeled fb03, for example, the major axis amplitudes for M2 and N2 at the surface are 0.28 and 0.06 m/s. Bennett (2010) showed that this reduction in the amplitude of the semidiurnal constituents is largely consistent with a simple vertically averaged, frictional linear long wave model with channel convergence that represents the major geometric characteristics of the Sound. The maximum phase difference in the M2 constituent at the surface between the ADCP at location bw, in CLIS, and the western stations shown in Fig. 3.10b is only 40° or 80 min.

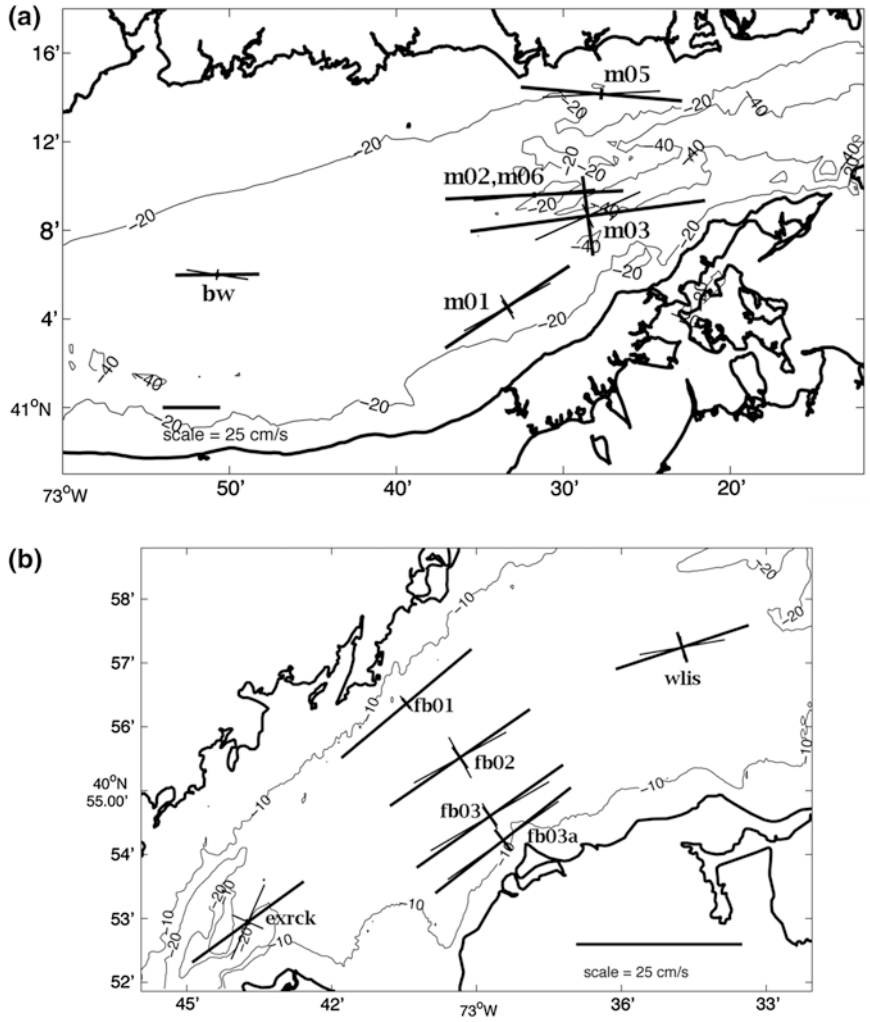

Fig. 3.10 Map of the coastline and bathymetry of **a** eastern and **b** western LIS showing the major and minor axes of the M2 tidal current ellipse at the surface (*thick lines*) and near the bottom (*thinner lines*). Note that the velocity scale is shown in the lower left corner of **a** and in the lower right of **b** and the bathymetric contours are at 10 and 20 m

The vertical structure of the principal harmonics was also described by Bennett et al. (2010) and they compared their results to the predictions of the model of Ianniello (1977a) using several alternate formulations of the vertical structure of the eddy diffusion coefficient. They found all were inconsistent with the observations. Codiga and Rear (2004) found similar results at sites in the approaches to BIS. They demonstrated that the most plausible explanation for the vertical structure was a modification of the planetary vorticity by horizontal shear in the residual currents. Whether it requires an unsteady closure model, a more realistic

geometry, or inclusion of residual vorticity effects to simulate the vertical structure of the tides, is an important and unresolved question.

Figure 3.11a–d show the vertical structure of the M2 tidal ellipse parameters (semi-major axis amplitude, phase, orientation, and ellipticity, respectively) as defined by Pawlowicz et al. (2002) at the WLIS station, computed using four different deployment intervals. The profiles computed from data acquired during the more highly stratified seasons, when the surface to bottom density difference exceeded 1 σ_T, are shown in red and those from less stratified conditions for are shown in black for comparison. Though the magnitudes of the uncertainties are comparable to the differences between the more and less stratified amplitudes, it is evident that the vertical gradient of the major axis amplitude is significantly enhanced during the more stratified intervals. The profiles in Fig. 3.11b also show changes to the vertical structure of the phase. During the less stratified periods, the phase difference between the top and bottom bin averages approximately 20°, and the gradient is almost uniform. During the more stratified intervals, however, the phase changes approximately 25° in the lower half of the water column, whereas it remains uniform in the upper half. Figure 3.10c and d show that during times of higher stratification, the orientation is closer to zero in the lower water column and that the ellipticity increases substantially at the bottom. These characteristics are also evident at other stations. The theory for the structure of tidal currents that are influenced by turbulent friction, the Coriolis acceleration, and stratification has been reviewed by Soulsby (1990) and shown to be useful in areas far from shore by, for example, Codiga and Rear (2004). The most comprehensive analytic theory for the three-dimensional structure of tides in channels was recently developed by Winant (2007); however, Bennett (2010) found that its predictions were inconsistent with her observation in LIS. Since the Winant (2007) theory is based on

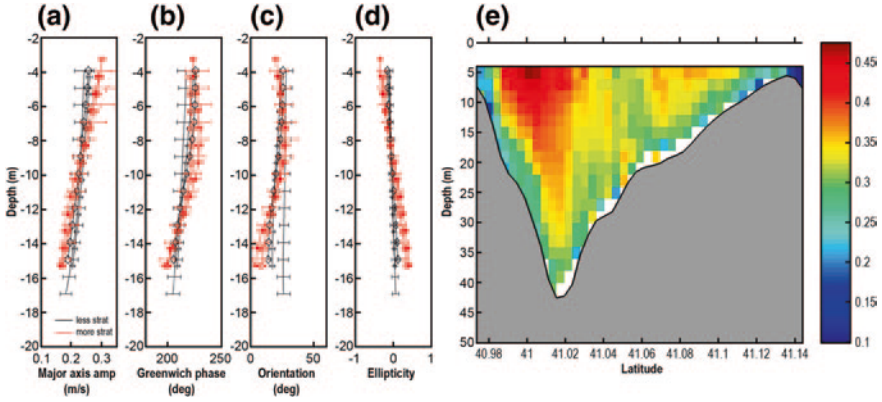

Fig. 3.11 The vertical structure of the M2 ellipse characteristics at the WLIS site computed using data from four separate deployments. Shown in panel **a** is the major axis amplitude, **b** the phase relative to Greenwich, **c** the orientation of the ellipse, and **d** the ellipticity (minor axis amplitude/major axis amplitude). The *red lines* show results from measurements acquired during more highly stratified, a surface to bottom density difference in excess of 1 σ_T, intervals. **e** the lateral and vertical structure of the M2 amplitude at the Bridgeport-Port Jefferson Ferry section

constant eddy coefficient turbulent closure and simple channel geometry, it seems likely that the complexity of the real geometry must be resolved and a sophisticated closure adopted as in the model of Hao (2008) for the tidal flow to be fully understood.

Observations from the vessel-mounted 600 kHz ADCP aboard the Bridgeport to Port Jefferson Ferry (see map in Fig. 3.24) provide a description of the structure of both longitudinal and lateral tidal currents in a lateral section in the central basin. Figure 3.11e shows the structure of amplitude of the M2 constituent of the component of current normal to the section for 2 m bins obtained from a harmonic analysis of a 22-day record segment; the center of the first bin is at approximately 5 m. Currents are surface intensified with significant lateral shear associated with depth variations. The corresponding structure of phase of the M2 constituent (not shown) indicates clear phase advance near the bottom and in the shallows on the channel flanks.

Tidal period fluctuations in the magnitude of vertical stratification in estuaries can result from differential advection of the mean along-Sound horizontal density gradient by vertically sheared along-Sound tidal currents. Simpson et al. (1990) referred to this effect as tidal straining and pointed out its influence on vertical mixing. A combination of current profile observations and density structure measurements has revealed that this mechanism is active in the eastern Sound. Figure 3.12a and c show the vertical structure of the M2 phase average of

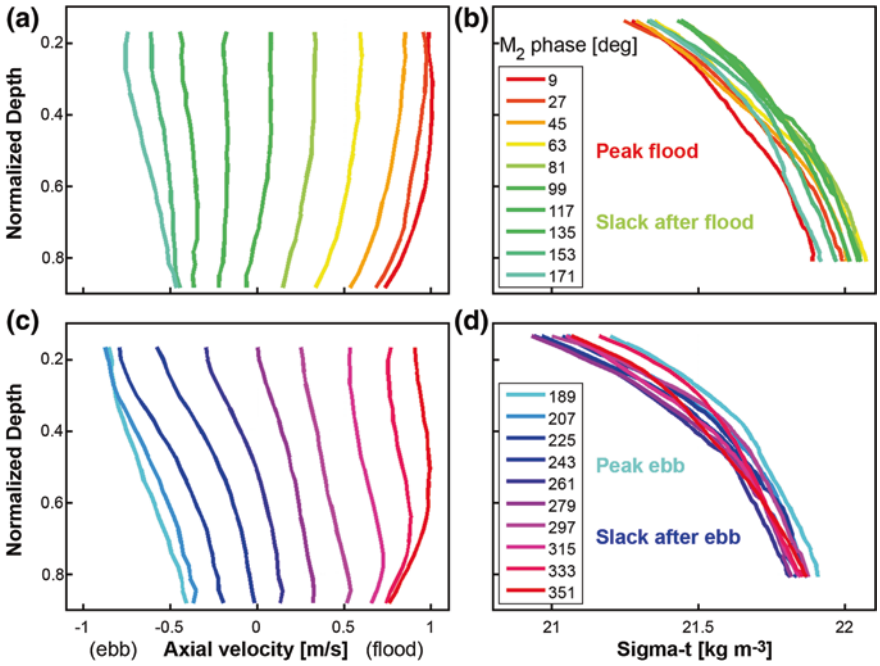

Fig. 3.12 **a** and **c** show the vertical structure of the M_2 phase averaged current in the direction 260° at station R08 in Fig. 3.23a. Zero phase is at maximum flood and colors represent phase values listed in the legends. Depths are normalized to the water depth. **b** and **d** show phase averaged density profiles

multiple years of current observations projected in the direction 260°. This direction best matches the alignment of tidal current ellipses. The measurements were obtained by Codiga (2007) using a ferry-mounted current profiler in an area midway between New London and Orient Point (near station R08 in Fig. 3.23a) where the water depth is 59 m. M2 phase averaged density profiles of several weeks of hourly ascents of a moored CTD profiler deployed by Codiga et al. (2002) at a site 46 m deep and approximately 4 km east of R08 are shown in Fig. 3.12b and d.

The velocity profiles show that the high amplitude tidal currents (~1 m/s) result in a sheared bottom boundary layer reaching as far as 20–30 m off the seafloor, about half the total water depth. The red lines in Fig. 3.12a and c show that during flood, the velocity is weakly sheared in the upper water column, and there is a subsurface velocity maximum below which the shear is strongest. In contrast, during and after ebb (blue-shaded lines), the velocity is sheared throughout the water column, in the opposite sense from deep flood conditions, with peak shears in the upper water column. The density profiles (Fig. 3.12b and d) show higher values after flood as is to be expected due to advection of the axial gradient. The slopes of the density profiles demonstrate that, while stratification in the deeper part of the water column varies modestly over the tidal cycle, the upper water column stratification is significantly enhanced during and after ebb (Fig. 3.12d) relative to the other half of the cycle (Fig. 3.12b). This is clear evidence that tidal straining is active. The quantitative implications of these cycles in shear and stratification on vertical fluxes and residual horizontal transport are very important topics for future investigation.

A completely unanticipated and unexplained result of the work of Bennett et al. (2010) was the discovery of high amplitude overtides in the western part of the basin. For example, near Execution Rocks (location exrck in Fig. 3.10b), the M6 was found to be approximately 25 % of the M2 amplitude. Figure 3.13 shows the along-Sound distribution of the ratio of the amplitude of the N2 and S2 to the M2 as black and red lines, respectively. Throughout the Sound, they remain at approximately 20 %. Since these constituents are close in frequency, friction and geometric effects should affect them in the same way and the ratios should, therefore, be constant. The ratio of the M4 to the M2 amplitude is shown in blue. It is also almost uniform and though it can be modified by a variety of nonlinear dynamical processes, either their effects cancel out or are small. The ratio of the M6 to M2 is similar to that of the M4 to the M2 in the eastern Sound, but it is significantly amplified at the three western Sound stations. This difference in the distribution of the characteristics of the overtides is likely due to the spatial variation in the magnitude of the nonlinear terms in the estuarine dynamics and kinematics, and their simulation is therefore a very sensitive metric of the performance of models. Bennett (2010) evaluated the predictions of the theory proposed by Parker (1984) for the consequences of quadratic bottom friction and advection of momentum in the dynamic balance, and of finite amplitude elevation changes in the conservation of volume equation, on the generation and propagation of overtides in the long wave model. The model was unable to simulate the observed structure.

Evidently, the recent observations of the structure of characteristics of the tides in LIS have posed new modeling challenges. Can models simulate the horizontal and

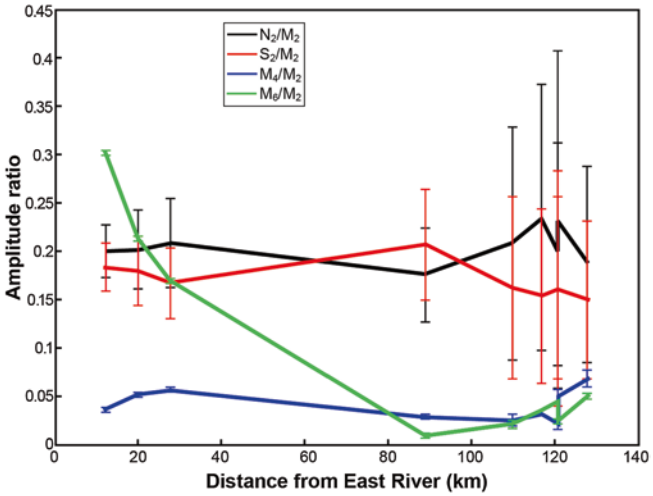

Fig. 3.13 The along-Sound structure of the amplitudes of the vertically averaged tidal current constituents scaled by the M2 amplitude. The green line shows the M6 and the blue line shows the M4

vertical variation in the characteristics of tides and the influence of stratification? If so, can they then predict the structure of the overtides, which are likely to be sensitive to the more subtle mechanisms in the models? It is important to improve our understanding of tidal currents by critical comparison of models and observations because their amplitudes far exceed those of the residual circulation, particularly in ELIS, such that tidal asymmetries may be an important influence on subtidal flow.

3.2 The Structure and Variability of the Hydrography

As in all estuaries, the hydrography and the circulation in the Sound are intrinsically coupled. The structure of the density field modifies the pressure gradient field set by sea level variations and strongly influences the circulation, particularly at low frequencies. The density-driven circulation generally leads to a transport of river water to the ocean and salt water toward land. Vertical gradients in density inhibit vertical mixing rates of heat, salt, and momentum and thereby modify the rates of transport. Since the Sound is shallow, pressure effects on density can be neglected and so the density variations are controlled by T and S. T is influenced by heat energy exchange with the atmosphere, solar radiation, and exchange with the adjacent ocean. Note that the magnitude of the exchange with the shelf at seasonal and annual scales is uncertain. Salinity (S) is controlled by the discharge of rivers and exchange with the ocean, and though precipitation-evaporation and inputs from aquifers have been assumed to play a secondary role, this is uncertain. Both the T and S budgets are modulated at seasonal scales, and these are manifested in observations of the distributions in the Sound.

The first comprehensive characterization of the structure and evolution of the *S* and *T* fields in LIS was reported by Riley (1952 and 1956). Using several years of ship surveys, he established the basic spatial trends and the range of seasonal variability. The State of Connecticut's Department of Environmental Protection (CTDEP) beginning in 1991 built on the surveys reported by Welsh and Eller (1991) and developed an extensive dataset with which to describe the seasonal and inter-annual variability of *S*, *T*, and the density fields. Kaputa and Olsen (2000) describe the program and review the first decade of results. Henceforth, we refer to this as the CTDEP dataset. It can be accessed at http://lisicos.uconn.edu/dep_portal.php. Subsequently, Gay et al. (2004) used the *S* data to develop a salt budget and estimate residence times and exchange rates with BIS. Lee and Lwiza (2005) characterized the inter-annual variability in *T* and *S*, and Whitney (2010) used the data to examine the influences of river discharge fluctuations.

Figure 3.14 shows the distribution of station locations in the CTDEP dataset. The green symbols show the locations of the stations sampled at monthly intervals throughout the year and at twice that frequency in the summer. Sampling at

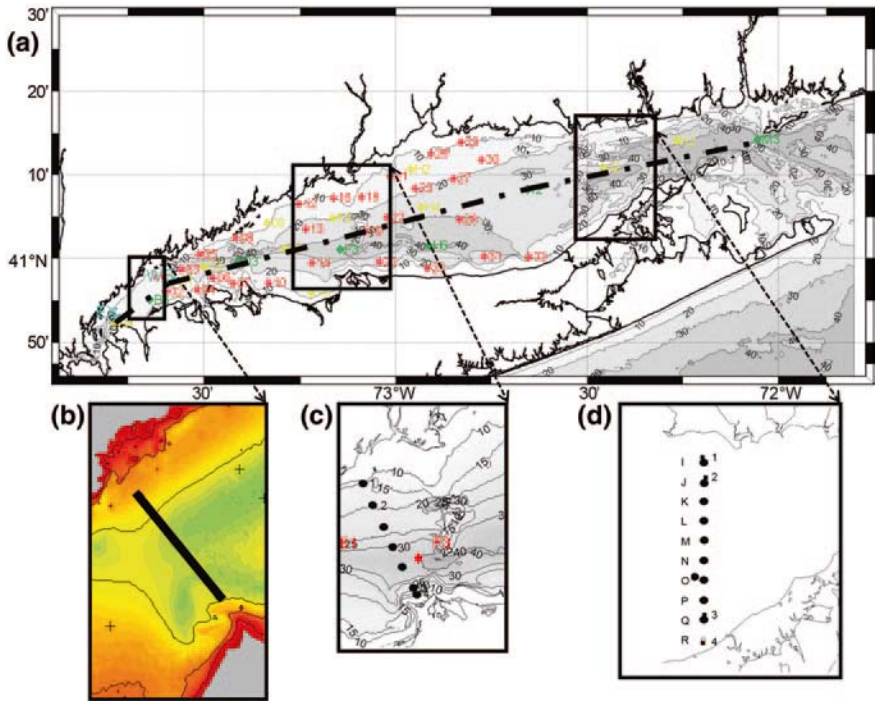

Fig. 3.14 **a** Map of LIS showing the bathymetry (depths in m) and the locations of the CTDEP hydrographic survey stations. **b** The coastline and cruise track used in the observation program described by Bennett (2010). **c** and **d** Show the stations used by O'Donnell and Bohlen (2003). The *thick dot-dash line* shows the along-Sound location for the vertical sections shown in Figs. 3.14, 3.15, 3.16, and 3.33

the seven stations, shown in green, began in 1991. The westernmost station in the East River, A2, was terminated in 1995. Year round sampling at the stations shown in yellow began in 1994. Another station, N3, not shown in the figure, was occupied in BIS from 1995 to 2002. Though there is inconsistency in the sampling interval and the high frequency fluctuations in the Sound are aliased, this dataset reveals the broad character of mean structures and the spatial and seasonal cycles of the S, T, and density, σ_T, distributions. The application of objective analysis, often referred to as OA (see Wilkin et al. 2002), to the estimation of the seasonal cycles from this data archive requires approximation of the space–time correlation function and the measurement noise for each variable. These statistics may depend upon location and time, and so are very difficult to estimate. Ad hoc approximations for the characteristics of the correlation functions are common. Lee and Lwiza (2008), for example, mapped the monthly evolution of the DO concentration in LIS with OA and used the sample station spacing as an estimate of the width of the correlation function. This is a common approach. If the sampling plan was developed to resolve the field with a limited number of stations, then choosing the correlation scale as the separation would be consistent. Further, the general appearance of contour maps is often insensitive to the details of the shape of the correlation function, though the characteristics of small-scale structures and estimates of gradients can be very sensitive to the assumptions adopted. The central value of the OA method is that it provides uncertainty estimates as well as the mapped field. The uncertainty estimates are very sensitive to the correlation function and noise levels chosen. Additional effort to refine the estimates of these statistics is, therefore, warranted. In the contour maps we present here using the CTDEP dataset, we follow the ad hoc approach of Lee and Lwiza (2008). Specifically, we assume that the covariance function at $\overrightarrow{x_0}$ is the form

$$C\left(x,y,z;\overrightarrow{x_0}\right) = \left\{ n^2 I\left(x,y,z\right) + \sigma^2 \exp\left\{ -\left(\frac{x-x_0}{L_x}\right)^2 - \left(\frac{y-y_0}{L_y}\right)^2 - \left(\frac{z-z_0}{L_Z}\right)^2 \right\} \right\}$$

where s^2 and n^2 are the signal and noise variances; x,y, and z are lags in the along-Sound, across-Sound, and vertical directions; and $L_{\{x,y,z\}}$ are the decorrelation length scales. The function $I\left(x,y,z\right)$ models the correlation structure of the noise and we assume $I\left(|x|>0,|y|>0,|z|>0\right)=0$ and $I\left(0,0,0\right)=1$, i.e., noise is uncorrelated in space and time. We then assume $L_x = 25\,\text{km}$, $L_y = 5\,\text{km}$, and $L_z = 5\,\text{m}$, and $n^2 = 100$. Note that the data are averaged by month at each station when more than one profile is available, which implicitly assumes that the correlation in time is a step function with a half width of 15 days. This is an assumption that should be reconsidered.

The vertical and along-Sound patterns of the monthly averaged S during April, August, and December are shown in Fig. 3.15. The section follows the black dashed line through stations A4, C1, I2, and M3. Note that the three-dimensional OA procedure allows data from all available stations to contribute to the structure. The horizontal axis is shown as distance along the dashed line from Execution Rocks (A4). Throughout the year, the lowest S is in the western Sound (25.0–27.0) and the

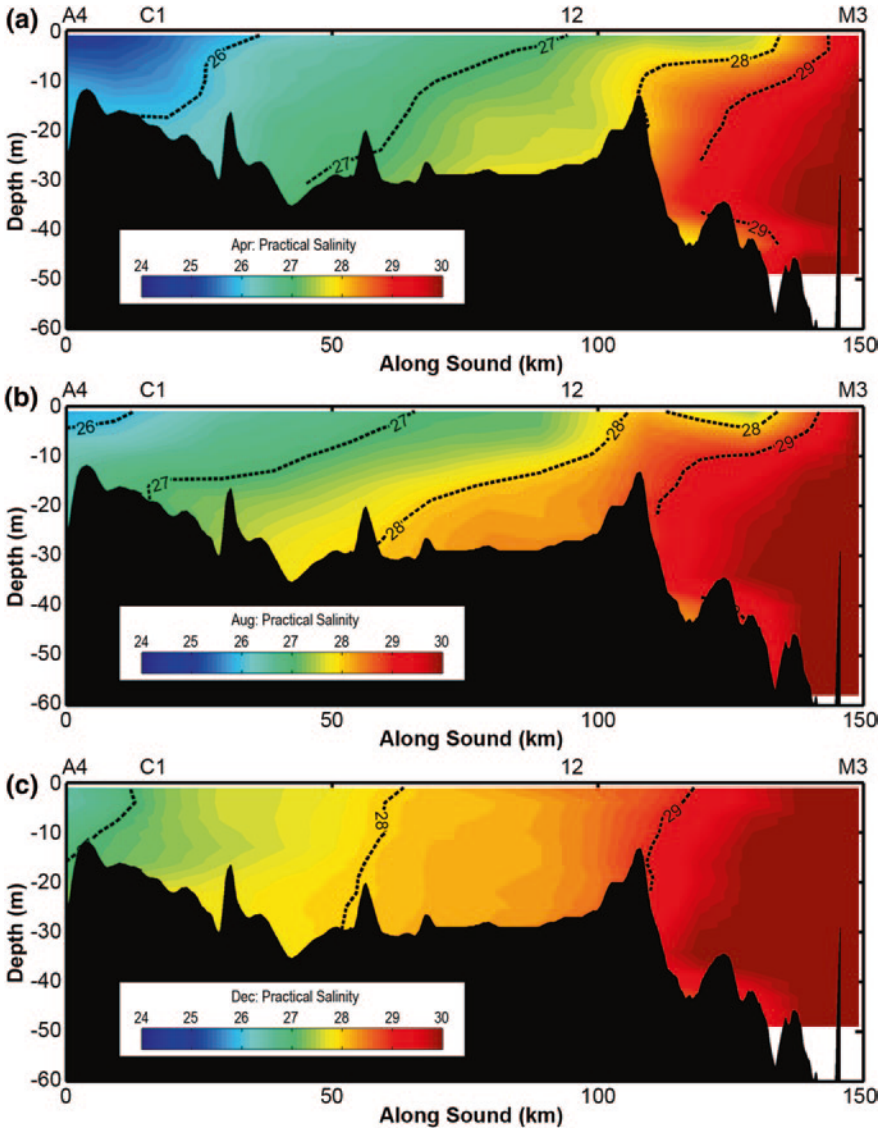

Fig. 3.15 The structure of the salinity distribution along the *dot-dash line* in Fig. 3.14 computed from the CTDEP survey data using data collected in **a** April, **b** August, and **c** December

highest values are at the eastern boundary (29.5–31.0). The amplitude of the annual cycle of S variations is approximately 1.5 at all stations. Throughout the Sound, the minimum S occurs in May, and the highest values are in November. In addition to this simple yearly oscillation, there are more subtle variations in the vertical and horizontal gradients in S. Comparison of the locations of the 26 and 29 contours in the April and August, and August and December S distributions of Fig. 3.15 demonstrates that the horizontal gradients are largest in April and lowest in December.

In the spring, the freshwater that discharges from the Connecticut River and the Hudson River appears to freshen the whole Sound. Though the S in eastern Sound is reduced, the western Sound is reduced slightly more and the horizontal gradient is enhanced. Between April and August, S increases throughout the Sound and the 27 and 28 contours move westward. The slope of the isohalines in the western Sound indicates that salt stratification persists there throughout the year though in December they have a steeper slope as a consequence of increased mixing.

The evolution of the monthly average T field is shown in Fig. 3.16. Note that the color scales are different in each frame since the magnitude of the annual cycle (22 °C) is much greater than the range due to the spatial structure. In January (not shown), the average T is near zero. By April, the water warms to between 5 and 7 °C with the warmest water in the western Sound surface waters. The near surface waters warms through the summer to more than 22 °C throughout much of the Sound and a thermocline develops approximately 10 m below the surface. In August, the bottom waters reach 20 °C. A region of high horizontal T gradients develops near the Mattituck Sill (at 100 km in Fig. 3.16) where the deeper waters are influenced by exchange with BIS and the continental shelf. Insolation is reduced in the fall and the wind stress associated with synoptic scale atmospheric patterns becomes greater, leading to cooling and vertical mixing in the Sound. By December, the T of the Sound falls to 7–10 °C and the isotherms are almost vertical. Note that the coldest water is in the western Sound.

The net effect of the fresh water and heating on the evolution of the density field, σ_T, is displayed in Fig. 3.17. Comparison of the location of the $\sigma_T = 21$ isopycnal in December and April shows that it moves between 40 and 60 km eastward in the spring due to warming and increased river discharge. By August, significant vertical stratification develops throughout most of the Sound, as shown by the reduced slope of the isopycnals, and density reaches a minimum with the $\sigma_T = 21$ isopycnal restricted to the eastern part of the Sound. The vertical structure of density shows a broad pycnocline centered at 10 m depth.

It is evident that both the vertical and horizontal density gradients are enhanced in August; however, the magnitude of the changes is not clearly revealed in the cross sections. In Fig. 3.18, we show the evolution of a finite difference estimate of the monthly mean stratification at 10 m below the surface, $\Phi(-10) = -\frac{\partial \rho}{\partial z}\Big|_{z=-10} = \frac{\rho(z=-15)-\rho(z=-5)}{10}$, at stations A4, C2, F3, H4, I2, and K2 which lie along the central axis of the Sound (see Fig. 3.14). Stratification is at a minimum at all stations in October–January. It begins to increase slowly in February at stations A4, C2, F3, H4, and I2, but accelerates in April and reaches a maximum in July. The highest stratification, $\Phi(-10) = 0.15\,\mathrm{kg/m^4}$, occurs at H4 with values closer to $0.1\,\mathrm{kg/m^4}$ elsewhere. At station K2, in the eastern Sound, the rapid development of stratification begins in February, and the peak is reached in April. The behavior at M3 is similar (not shown) though the maximum is only half of that at K2.

If the equation of state for seawater is approximated in a layer $z_L \le z \le z_T$ as $\rho(S,T,P) = \rho\left(\bar{S},\bar{T},0\right) + \alpha\left(\bar{S},\bar{T}\right)\left(T-\bar{T}\right) - \beta\left(\bar{S},\bar{T}\right)(S-\bar{S})$ where $\bar{S}(t)$ and $\bar{T}(t)$ are the average S and T in the layer for a particular month, then the stratification

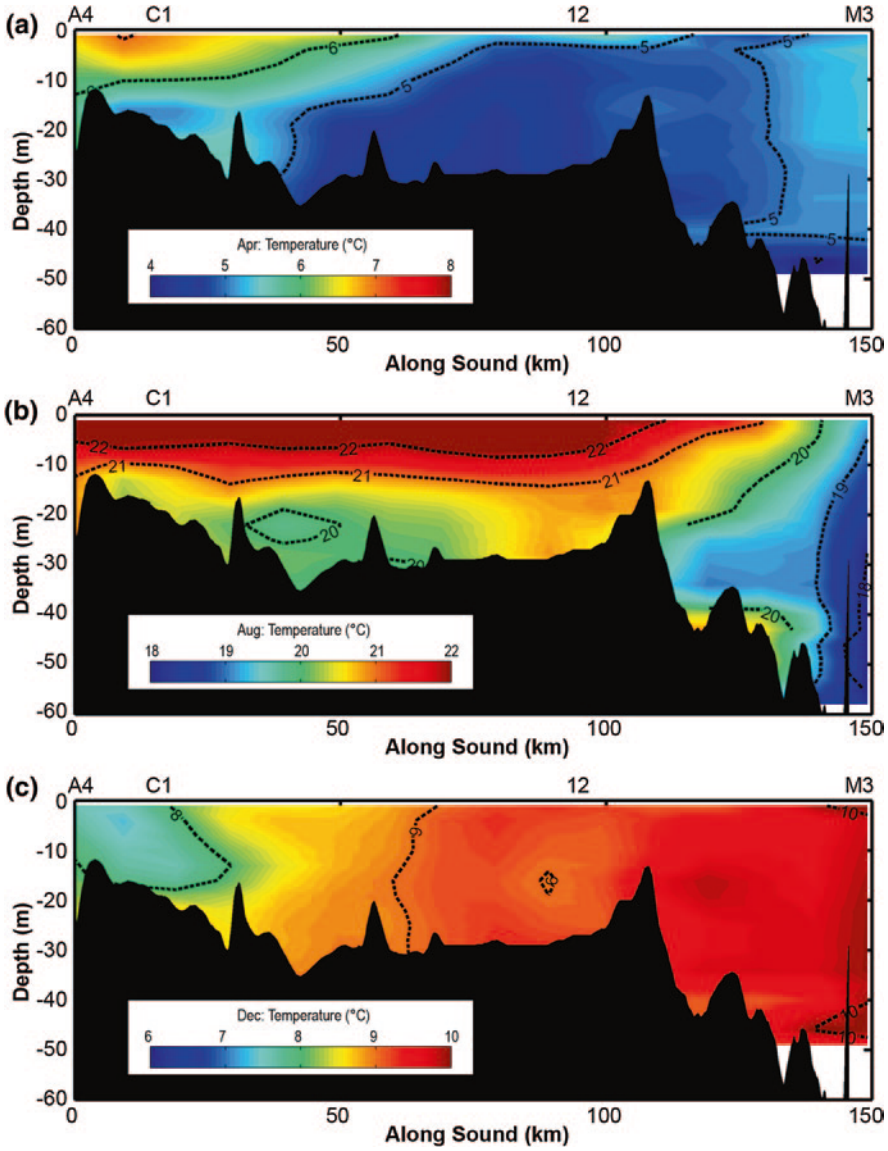

Fig. 3.16 The structure of the temperature distribution along the *dot-dash line* in Fig. 3.14 computed from the CTDEP survey data using data collected in **a** April, **b** August, and **c** December

can be approximated $\Phi(z) = -\alpha\left(\bar{S},\bar{T}\right)\left.\frac{\partial T}{\partial z}\right|_z + \beta\left(\bar{S},\bar{T}\right)\left.\frac{\partial S}{\partial z}\right|_z$ where α and β are the thermal expansion and haline contraction coefficients estimated following McDougall (1987). Using the notation $\langle\bar{T}\rangle$ and $\langle\bar{S}\rangle$ to represent the annual averages of the layer average T and S, then $\Phi(z)$ can be approximated as the sum of the thermal, Φ_T, and haline, Φ_s, effects as $\Phi = \Phi_T(T) + \Phi_s(S) = -\alpha\left(\langle\bar{S}\rangle,\bar{T}\right)\left.\frac{\partial T}{\partial z}\right|_z + \beta\left(\bar{S},\langle\bar{T}\rangle\right)\left.\frac{\partial S}{\partial z}\right|_z$.

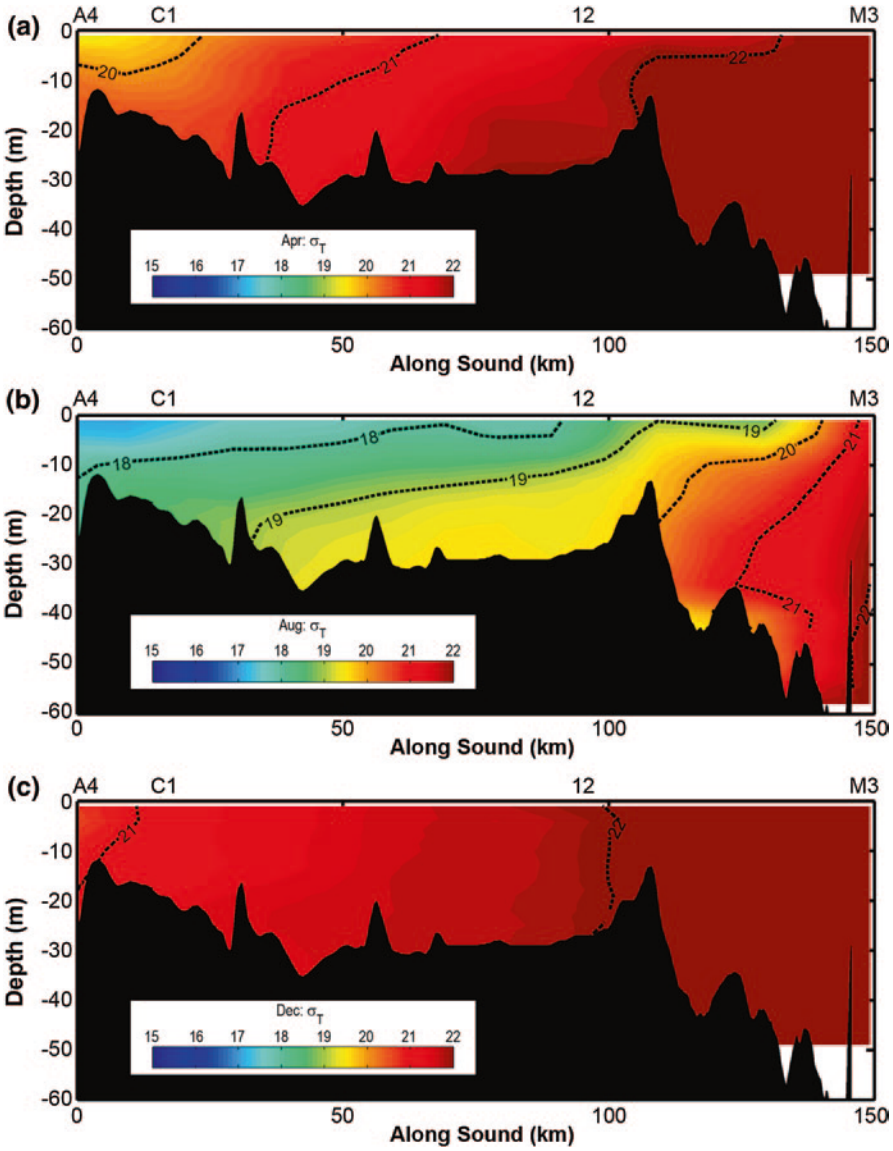

Fig. 3.17 The structure of the density (σ_T) distribution along the *dot-dash line* in Fig. 3.14 computed from the CTDEP survey data using data collected in **a** April, **b** August, and **c** December

Numerical experiments demonstrate the error due to the neglect of the T dependence of the haline expansion coefficient, and the S dependence of the thermal expansion coefficient is < 5 %.

To reveal the roles of warming and freshwater inflow variations on stratification at stations A4, C2, F3, H4, I2, and K2, Fig. 3.18 shows the annual cycle of the Φ_T as green lines and Φ_s as red lines. Since the red lines overlie the black lines from January

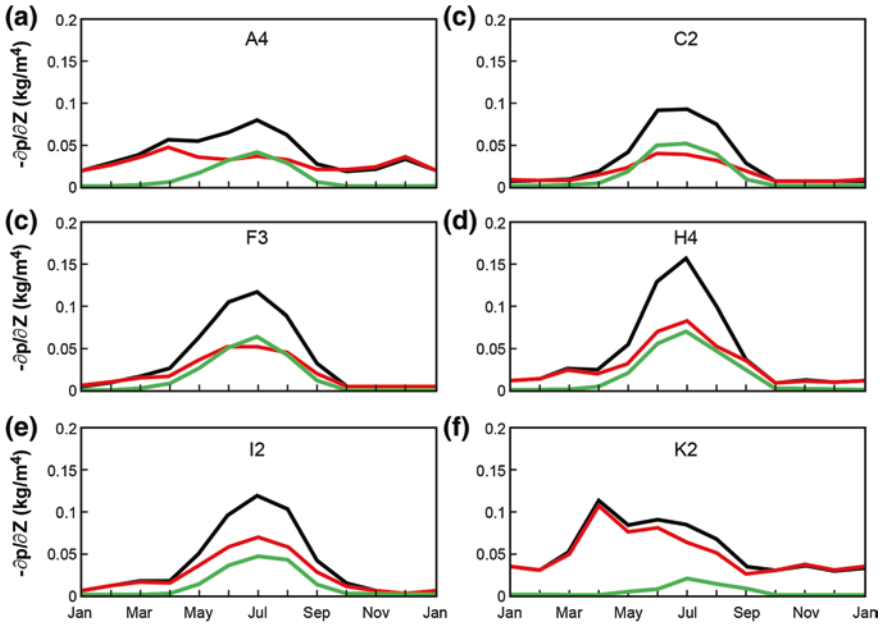

Fig. 3.18 Time evolution of the vertical stratification (*black line*) at CTDEP stations **a** A4, **b** C2, **c** F3, **d** H4, **e** I2, and **f** K2. The *red* and *green lines* show the approximate contributions of salinity and temperature to variations to the stratification, respectively

to April at each station, it is clear that it is the increase in freshwater discharge (see Fig. 3.1) that is responsible for the initial stratification enhancement. At Station A4, at the western end of the Sound near the East River, the freshwater effect peaks in April and then diminishes through the rest of the year. A similar pattern occurs at stations K2 and M3, which are located in the eastern Sound near the Connecticut River. At the other stations, the peak of the freshwater-induced stratification (Φ_s) is delayed until July, likely as a consequence of the time required to transport it. During the May to September interval, the contribution of the thermal effect on stratification is significant at all stations. It peaks in July when the magnitude of the effect equals that of salt at all stations except K2 and M3, which are deeper and, presumably, more influenced by exchange with BIS and the continental shelf. In late summer and fall, both the effects of salt and heat drop and by October stratification reaches its minimum level, which is solely due to the *S* structure. This situation persists until January.

Pritchard (1956) proposed that the modification to the pressure field created by spatial gradients in density was a key component of the force balance that determines the circulation in estuaries. Wilson (1976) applied the basic idea to estimate the vertical structure of the axial circulation in LIS using observations obtained during a series of cruises. The horizontal baroclinic pressure gradient at level z can be expressed $H_B(z) = \frac{g}{\rho_0} \int_z^0 \frac{\partial \rho}{\partial x} dz$ where $g = 9.8$ m/s is the acceleration of gravity

at the surface of the earth and $\rho_0 = 1{,}000\,\mathrm{kg/m^3}$ is a reference density. Note that the force is $-\rho H_B$ and is directed toward the region of lower density.

Since the vertical structure of the horizontal gradient is weak, the temporal pattern is similar at all depths and magnitude of H_B increases linearly with distance below the surface. The solid lines in Fig. 3.19 show the annual evolution of $H_B(z = -20\ \mathrm{m})$ estimated using a finite difference approximation between stations A4 and C1 (blue), C1 and I2 (red), and I2 and M3 (magenta). All values are positive, indicating the baroclinic pressure gradient force is directed to the west, and have a magnitude of order $10^{-5}\ \mathrm{m/s^2}$. The mean values in the eastern and western ends of the Sound are comparable and approximately four times larger than in CLIS, between C1 and I2. Wilson (1976) found a similar pattern in his more limited dataset. However, the seasonal evolution of H_B in the east and west is quite different. Between A4 and C1 (solid blue line), there is an enhancement of the gradient in April, a minimum in July–August, and an increase until January. In contrast, the gradient between I2 and M3 (solid magenta line) at the eastern end of the Sound varies with a comparable amplitude but with a maxima in June–August and minima in the winter. In CLIS, between C1 and I2, the seasonal cycle appears to be weaker and in phase with the variations in ELIS.

To assess the cause of the variability, we divide the variations in the baroclinic pressure gradient into two components, $H_B(z) = H_{BT}(z) + H_{BS}(z)$, where $H_{BS}(z) = \frac{g}{\rho_0}\int_z^0 \beta\left(\bar{S},\langle\bar{T}\rangle\right)\frac{\partial S}{\partial x}dz$ is the contribution resulting from variations in S and $H_{BT}(z) = -\frac{g}{\rho_0}\int_z^0 \alpha\left(\langle\bar{S}\rangle,\bar{T}\right)\frac{\partial T}{\partial x}dz$ is the effect of T. In Fig. 3.19, the dashed lines show $H_{BS}(z = -20\,\mathrm{m})$ for the three sections using the color code defined above. The

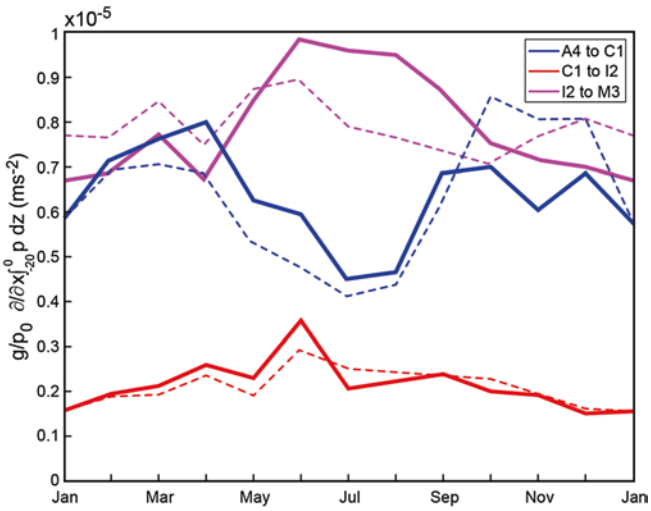

Fig. 3.19 The annual evolution of the horizontal baroclinic pressure gradient between CTDEP stations A4 and C1 (*blue*), C1 and I2 (*red*), and I2 and M3 (*magenta*). The *dashed line* shows the approximate contribution of salinity variations

differences between the solid and dashed lines represent the effect of T. During intervals in which the dashed line falls above the solid line on the graph, the horizontal T gradient acts to oppose the effects of the S gradient. Since the lines of the same color are close together, it is clear that the baroclinically driven flow is dominantly controlled by the S variations. Though the vertical T gradient is largest during the summer in the central Sound, the T effect on $H_B\,(z)$ is modest (see red lines). In ELIS (magenta lines), the dashed line is above the solid line between September and May when atmospheric cooling reduces T in the central Sound more than in the deeper waters of the eastern Sound (see Fig. 3.16). A similar behavior is evident in the western Sound (blue lines) during September–January where the shallow waters cool more rapidly.

There are few reports describing observation of the across-Sound structure of the S, T, density, and pressure gradients, though Riley (1956) noted the lateral gradients in surface properties and Hardy (1972) showed hydrographic casts along a north to south section in the eastern Sound in which significantly fresher water occupied an upper water column layer that deepened toward Long Island. Even early numerical models show substantial lateral shear in the mean flow (Murphy 1979). Recent theoretical work (e.g., Kasai et al. 2000 and Valle-Levinson 2008) suggests that the magnitude of vertical friction and the width of the estuary control the degree of lateral variation in estuaries, so periods of weak vertical stratification in the wider areas of the Sound are likely to exhibit significant across-Sound gradients.

To remove the influence of tidal frequency variations from cross-Sound surveys, several sections must be observed for at least a whole tidal cycle. This approach has been employed by O'Donnell and Bohlen (2003) and Bennett (2010) at the three locations shown in Fig. 3.14b, c, and d. Bennett (2010) describes the observations and analysis of data collected during two 25 h intervals between March 5 and 8, 2005 and July 31 and August 1, 2005 along the line indicted in Fig. 3.14b. In the March experiment, they visited four equally spaced stations with a profiling conductivity, T, and depth (CTD) sensor, and in the summer they employed an undulating towed vehicle and achieved much higher spatial resolution. Figure 3.20a and b show the mean vertical structure of the S and T fields observed in July when viewed looking eastward with the coast of Connecticut on the left and Long Island on the right. The S exhibits a maximum of 26.2 at the center of the section at the bottom and a top to bottom difference of 0.8. The isohalines slope slightly downward to the south. The pattern of the isotherms in Fig. 3.20b shows a similar structure with a maximum of 23 °C at the surface and a 5 °C vertical variation. There is no appreciable slope to the isotherms. The winter situation is illustrated in Fig. 3.20c and d. Here the maximum S is 26.1 psu, and it is located at the bottom on the northern side of the section. The minimum is 25.5 psu and is at the surface near the Long Island shore. The steeply sloping isohalines show that the vertical gradients are weak but the horizontal gradients are relatively large. Bennett (2010) reported a similar structure in March 2006.

At a section further to the east, O'Donnell and Bohlen (2003) surveyed the S, T, and velocity fields during three two-day sampling programs along a section with seven stations near Stratford Shoals (see Fig. 3.14b) during the interval July 20 to August 6, 1995. The mean structure of the S, T, and density (σ_T) is shown in Fig. 3.21 a–c. The horizontal isolines indicate that the across-Sound gradients in

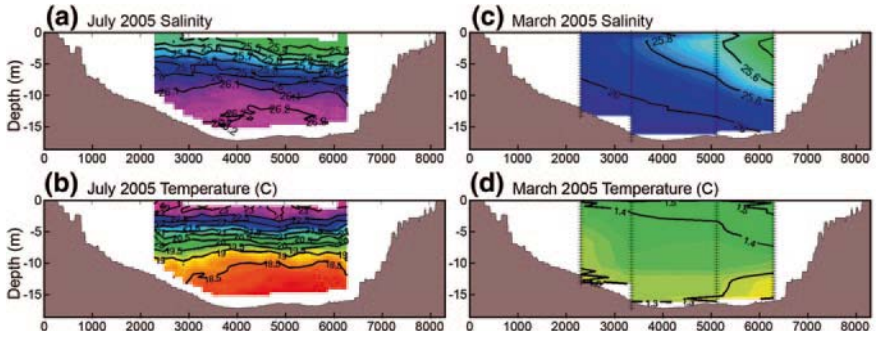

Fig. 3.20 Across-Sound sections of the **a** salinity and **b** temperature observed along line shown in Fig. 3.13b during July 2005 by Bennett (2010). **c** and **d** Show the same properties observed in March 2005. Adapted from Bennett (2010)

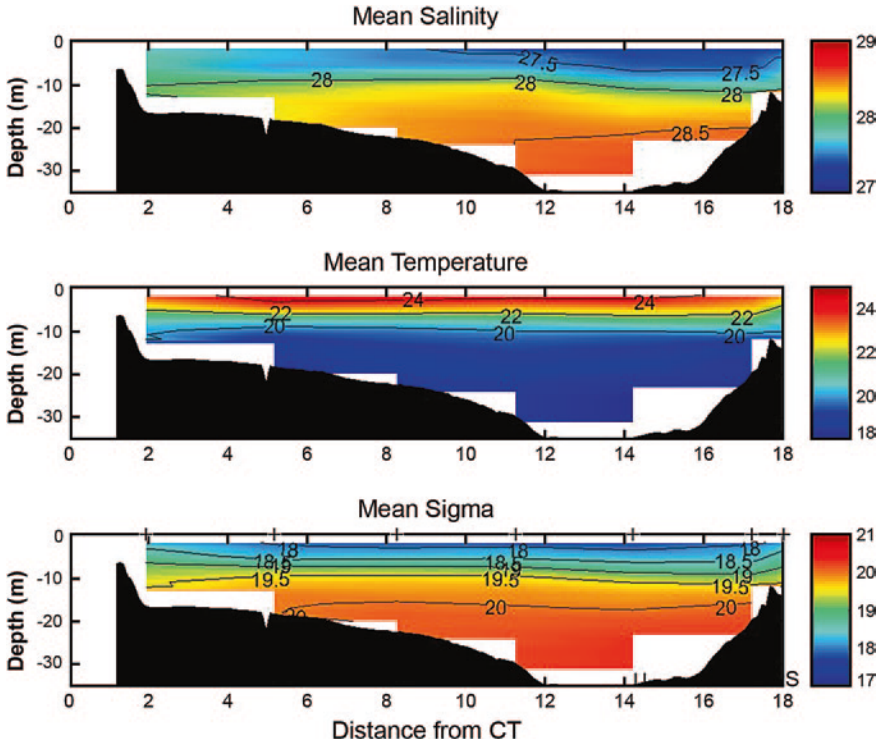

Fig. 3.21 The vertical and across-Sound structure near Stratford Shoals (see Fig. 3.13c) of the mean salinity (*top frame*), temperature (*middle frame*), and density (σ_T) during the interval, July 20-August 6, 1995. Note that the Connecticut coast is on the left and the '+' symbols at the top of 18c show the station locations. Adapted from O'Donnell and Bohlen (2003)

all three properties appear to be very weak. This is consistent with summer observation of Bennett (2010) shown in Fig. 3.20a and b.

In a survey earlier the same year (April 26 to May 6, 1995) that visited 10 stations along a section near Hammonassett Point (see Fig. 3.14d), O'Donnell and Bohlen (2003) found the mean structure of the S, T, and σ_T fields shown in Fig. 3.22 a–c. These show significant across-Sound gradients. Though the mouth of the Connecticut River, the largest source of fresh water to the Sound, is only 10 km to the east of the northern end of the section, the freshest water ($S \sim 21$) is found on the southern end. Unfortunately, observations were inadequate to determine whether this structure persists throughout the year or whether it is only a feature of the spring hydrography as suggested by the Bennett et al. (2010) observations.

The first persistent observations to reveal the mean and seasonal variability of the lateral structure of the near surface S field in the eastern Sound were obtained by the New London to Orient Point Ferry observation system described by Codiga (2007) and made available at http://www.po.gso.uri.edu/~codiga/foster/getdata.htm. Salinity and other properties were measured in water pumped from an intake in the vessel hull approximately 2.5 m below the water surface and recorded every 30 s together with the ship's position. When

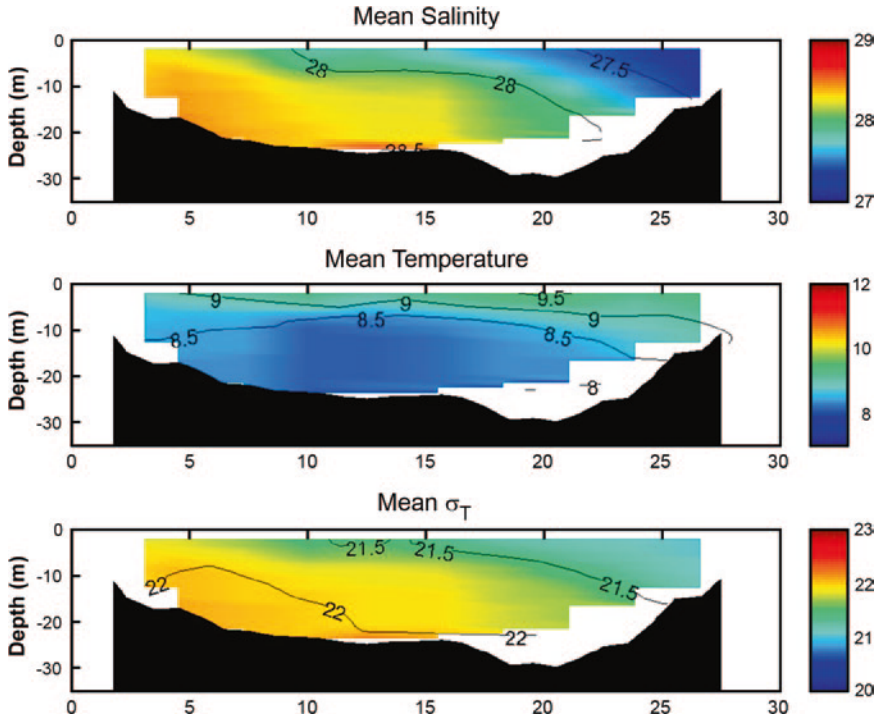

Fig. 3.22 The across-Sound structure near Hammonassett Point (see Fig. 3.13d) of the mean salinity (*top frame*), temperature (*middle frame*), and density (σ_T) during the interval April 26–28, 1995. Adapted from O'Donnell and Bohlen (2003)

operating, the ferry transits the Sound approximately eight times a day between 0700 and 2300. In Fig. 3.23a, we show the coastline and bathymetry of the eastern Sound in the vicinity of the ferry's track. The dashed line shows a convenient across-Sound coordinate and the solid line indicates the boundary of bins Codiga and Aurin (2007) used to average their measurements. These are labeled R01-R17, with the numbers increasing to the south. The southernmost segment, in Plum Gut, is labeled G01. Using s01 and s17 to represent the surface S in bins R01 and R17, we compute the time series of the five day average across-Sound S difference as $\delta s_{\{01-17\}} =< s01 - s17 >$, and the standard deviation as $\sigma s_{\{01-17\}} =< (s01 - s17)^2 >^{1/2}$. In Fig. 3.23b, we show the evolution of $\delta s_{\{01-17\}} \pm \sigma s_{\{01-17\}}$ for the interval July 2005 to September 2006. Note that there is a data gap between January and March of 2006 and that $\delta s_{\{01-17\}}$ is less sensitive to the instrument drift that makes long-term measurements of S difficult. The long-term mean monthly discharge, together with the 68th percentile interval, in the Connecticut River is displayed in Fig. 3.23c. The discharge during the interval of the ferry surveys is also shown. Note that the Connecticut River discharge is well above the long-term average during October 2005 and May–July 2006. The National Climatic Data Centers monthly precipitation index for southern New Hampshire (http://www7.ncdc.noaa.gov/CDO/cdo) shows that this is a consequence of anomalous precipitation in the watershed.

The principal result of this analysis is that $\delta s_{\{01-17\}} > 0$, i.e., the freshest water was at the southern shore throughout the fall of 2005 and in the spring of 2006 when the discharge in the Connecticut River was low, less than $500 m^3/s$. This suggests that the observations of low S water at the southern end of the Hammonassett Point

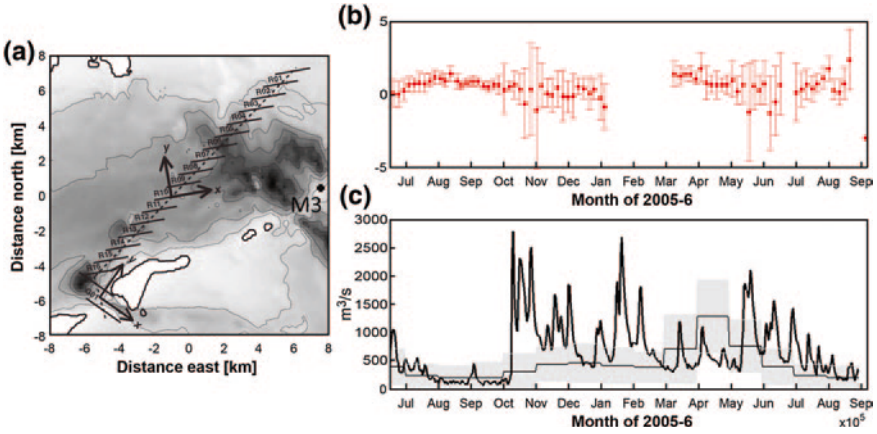

Fig. 3.23 **a** The coastline and bathymetry of eastern LIS showing boundaries of averaging intervals for the salinity observations shown in panel (**b**), from Codiga and Aurin (2007). **b** shows the evolution of the salinity difference across the section, $\delta s_{\{01-17\}} \pm \sigma s_{\{01-17\}}$ for the interval July 2005 to September 2006. The daily average discharge in the Connecticut River at Thompsonville is shown in (**c**) by the *solid black line* for the same period. The long-term mean discharge is shown by the histogram with one standard deviation shown in *gray*

section by O'Donnell and Bohlen (2003) were not anomalous, but a robust feature of the eastern Sound hydrography. When the discharge was anomalously high in the fall of 2005 and summer of 2006, $\sigma s_{\{01-17\}}$ became very large and, therefore, the sign of the gradient is uncertain. The aerial surveys of the river plume front of the Connecticut River by Garvine (1974) showed that the plume could extend to the eastern end of the Sound during ebb tide and high discharge conditions. It is therefore plausible that the ferry schedule leads to aliasing of the tidal frequency fluctuations in the S field during periods of high discharge in the Connecticut River. The observation of the variability of the subsurface hydrographic structure and the development of a quantitative understanding of the response of the hydrography to discharge variability are important tasks for the future.

The evolution of the vertical structure of the S,T, and density fields at sites in the central (between stations 19 and 20 in Fig. 3.14) and eastern Sound (near K2 in Fig. 3.14) has been described by Codiga et al. (2002) using a CTD system that profiles most of the water column at hourly intervals. They found that the density profile took a broad range of shapes, commonly being weakly stratified throughout the water column or having stronger stratification in a layer 10–20 m deep overlying weaker stratification. Less commonly, it consisted of a well-mixed layer overlying stratification. At the CLIS site, during a spring 2002 deployment, the transition from nearly vertically uniform to stratified conditions occurred in a relatively smooth fashion over several weeks, while in contrast the breakdown of stratification during the summer-fall deployment occurred in a series of abrupt mixing episodes associated with storm events. During the simultaneous summer-fall deployments in the central and eastern Sound, the density stratification was effectively eliminated within hours at both sites in response to certain strong storm events, but restratification was complete within about a day at the eastern site and within about 2 days at the central site. The response to other wind events was different at the two sites, consistent with the earlier demonstration that local winds at different sites in the Sound are not coherent on short time scales.

The important dynamic influence of the S and T fields arises through their influence on density and horizontal pressure gradients. The magnitude of the acceleration due to the along-Sound baroclinic pressure gradient in both the western and eastern ends of the Sound, shown in Fig. 3.19, is on the order of $0.5 \times 10^{-5}\mathrm{m/s^2}$. The magnitudes of the corresponding across-Sound quantities are at least comparable. These are large values. If, as in the model of Hansen and Rattray (1965), the divergence of the vertical turbulent momentum flux was required to balance H_B in a layer of 20 m depth, then using an eddy viscosity magnitude of $10^{-3}\mathrm{m^2/m^2/s}$, an along-estuary residual velocity at the surface of approximately $H_b \frac{D^2}{A_z} = 10^{-5} \times 10^3 \times \frac{20^2}{5} \sim 10\,\mathrm{cm/s}$ would be required. Since H_B varies by 50 % over the year, the magnitude of the seasonal variation in the residual circulation should be 5 cm/s. If the springtime across-Sound gradient were to be near geostrophic balance, then the lateral variation in the along-Sound current in the spring would have to be on the order of 1 m/s. Since this would be evident in the most primitive current measurements, the barotropic pressure gradient and frictional stresses must also be significant in the lateral dynamic balance.

3.3 Residual Circulation

The residual circulation in LIS was first characterized by Riley (1952) by summarizing drift bottle observations and measurements made by the US Coast and Geodetic Survey using current poles and current log lines (Le Lacheur and Sammons 1932). He created a general view of residual currents near the surface and described large-scale gyres in each of the three basins, augmented by many smaller-scale features. In CLIS, he observed a general clockwise rotation, and he found counterclockwise surface currents in the eastern and western basins. These observations were augmented by those of Larkin and Riley (1967), Gross and Bumpus (1972), Hollman and Sandberg (1972), Gordon and Pilbeam (1975), and Paskausky (1976) to include near bottom drift estimates in the central Sound. These revealed a two-layer east–west exchange flow consistent with the estuarine circulation described by Pritchard (1956), except nearshore in less than 10 m of water where mixing occurred throughout the water column. Large-scale nontidal events were found to correlate with maximum daily wind values. These events were typically on the order of 5–20 days in the winter and less than 3 days in the summer, and so they concluded that a 10-day record in the summer and a 20-day record in the winter should be sufficient to characterize the mean flow. General trends included westward flow mid-Sound, northward flow in shallower waters off the Connecticut coast, and some southward flow closer to the Long Island shore.

Even now, observations of the long-term mean circulation in the Sound are very limited, so the theoretical models are necessary to sensibly interpolate what is available. There is a hierarchy of complexity in theories. The earliest and simplest ones have focused on two driving mechanisms, the density gradients (Hansen and Rattray 1965; Wilson 1976) and the nonlinearity of the tidal flow (Ianniello 1977a; Murphy 1979). Though a large fraction of the fresh water in LIS comes from the Connecticut River and is delivered to the northern side of the Sound, the early theories for the residual circulation in LIS (Wilson 1976 and Ianniello 1977a) assume that the estuary is laterally homogenous. Only recently have measurements been available that resolve lateral variations and motivated the need for more sophisticated models. For completeness, we comment on the early models and then describe the more recent model results that yield a comprehensive view of the circulation that is largely consistent with the available observations.

Ianniello (1977a) developed an analytic model of the residual circulation in an estuary with weak density gradients to evaluate the magnitude and distribution of the tidally driven residual circulation. His model predicted that the Lagrangian residual circulation had a strong vertical structure: westward at the surface and eastward at depth. Note that this pattern of circulation is counter to the traditional notion of estuarine circulation in which the baroclinic pressure gradient is balanced by turbulent friction. In a complementary study, Wilson (1976) developed a numerical model of the buoyancy-driven circulation in LIS that adopted the baroclinic-friction balance of Hansen and Rattray (1965) but specified the density field using observations from east–west transects along the center of LIS.

The predictions of the model showed westward motion at depth and eastward motion at the surface as expected and with magnitudes that were consistent with the data available. Murphy (1979) expanded on the dynamics used in Ianniello's horizontally averaged model and studied the effect of more realistic geometry and bathymetry on the across-Sound structure of the circulation using a numerical model. He neglected the density-driven motion. Murphy found an extremely complex Eulerian residual circulation pattern with several large eddies in the eastern Sound. At the time, there was little observational evidence with which to discriminate the relative value of these models.

Schmalz (1993) developed a complex three-dimensional model that included both density variations and nonlinear effects. The prediction of the distribution of the mean velocity at the surface showed similar patterns and orders of magnitude velocities to those of Murphy (1979). Though complex, the dominant pattern in both models showed a westward motion on the north side of the Sound and eastward motion along the Long Island shore with a large cyclonic (counterclockwise) gyre dominating the central basin as was proposed by Riley (1956). The near bottom circulation was predicted to be to the west everywhere except in the vicinity of the Mattituck Sill and Stratford Shoals where topography complicated the flow. Valle-Levinson and Wilson (1998) studied the dynamics in the vicinity of the Mattituck Sill in more detail with a similar model and Valle-Levinson et al. (1995) noted the role of the interaction of the exchange flow through the East River, wind, and tides on the rate of vertical mixing in WLIS. Blumberg et al. (1999) developed a three-dimensional model to assist in the prediction of water treatment plant upgrades on water quality and Signell et al. (2000) developed a similar model that also included the effect of surface gravity waves on the bottom stress in order to understand the distribution of bottom sediments in the Sound.

The most comprehensive model prediction of the circulation in the Sound available to date is that of Crowley (2005) and Wilson et al. (2005). They implemented a data assimilating version of the ROMS three-dimensional circulation model for LIS. They performed four 1–3 month simulations using meteorological and sea level observations collected in 1988 to include the effects of coupling to the atmosphere and adjacent ocean. T and S observations from an intensive campaign in 1988 were incorporated through data assimilation to simulate the effects of river discharge fluctuations and seasonal heating rate cycles. This enabled examination of seasonal variability in the circulation. The model demonstrated the amplitude and phase of the principal tidal harmonics well and predictions also compared favorably with the S and T observations. They also provided a qualitative comparison to the moored current meter program reported by Vieira (2000), which included approximately 10 sensors on six transects across LIS between March and October 1988. The locations are shown in Fig. 3.24. These observations were not synoptic. Each transect was occupied for approximately 30 days and then the instruments were recovered and redeployed on the next transect to the east. Transects 5 and 6 were occupied simultaneously in both June and September. Figure 3.24 shows a very complex current pattern in both speed and direction. The near surface flow, shown in red, is generally eastward and the deeper flow is westward as expected from the results of the simple baroclinic pressure gradient

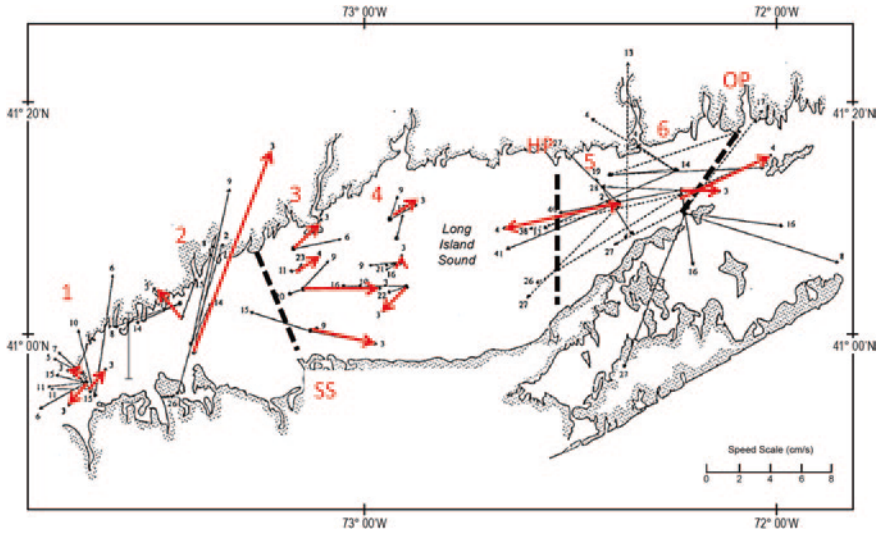

Fig. 3.24 A map the coastline of LIS showing the mooring locations and the mean flow estimates reported by Vieira (2000). The *dashed vectors* show the results of the June deployments. Sections are labeled 1–6 increasing to the east and the small numbers at the tip of the arrows indicate the depth of the measurement. Measurements above 5 m are shown in *red*. The *dashed lines* labeled SS and HP show the approximate locations of O'Donnell and Bohlen (2003) measurements and the OP shows the ferry transect described by Codiga and Aurin (2007). Section 3 is similar to that of Bennett (2010). Modified from Vieira (2000)

balancing turbulent friction theories of Hansen and Rattray (1965) and Wilson (1976). However, there are very large across-channel velocity components at all depths and a coherent pattern is difficult to extract. The extent to which this is due to the nonsynoptic sampling plan is unclear. For this reason, a model that is consistent with these and other measurements, and also with our understanding of the dynamics, is likely to yield a better estimate of the circulation and its variability.

The Crowley (2005) predictions of the mean along-Sound velocity at the Vieira sections labeled 3, 4, and 6 in Fig. 3.24 are shown in Fig. 3.25. The general structure of the velocity component distributions at Section 3, Fig. 3.25a and b, have some similar characteristics. The model predicts in the deeper parts of the cross-section that near the surface (above 15 m), the flow is eastward (positive) and westward below that and in the shallower areas near the Connecticut shore. The observations in Fig. 3.25b are sparse but do show the surface layer moving eastward. The magnitudes appear to be half of that predicted. At Section 4, shown in Fig. 3.25c, the eastward flowing layer in the model is much shallower than at Section 3 across most of the section, but fills almost the entire water column near the Long Island shore. The observations shown in Fig. 3.25d were only obtained in the region of slow westward flow, but are largely consistent with the predictions. At Section 6, the model predicts a very large eastward flow above 20 m in the southern half of the section (see Fig. 3.25e) and a strong westward flow elsewhere.

Only six moorings were available on Section 6; however, Fig. 3.25f shows that they do reveal the strong westward motion in the deep area and substantial lateral and vertical shears that are similar to that predicted. As at Section 3, the magnitude of the observed eastward motion is substantially less than that predicted.

Observations from the vessel mounted 600 kHz ADCP aboard the Bridgeport to Port Jefferson Ferry resolve the lateral structure of longitudinal residual currents along Section 3 of Vieira (2000) and Crowley (2005). As Fig. 3.25 shows, this is slightly to the east of Section SS of O'Donnell and Bohlen (2003). Figure 3.25g shows the mean east velocity component observed between August 6 and September 28, 2004. Westward flow (blue) is confined to the main channel with a zero crossing at approximately 7 m. Eastward flow (red) is confined to the water column above approximately 7 m and to the shallow northern flank of the section. Note that the center of the first bin is at approximately 5 m. The structure of the flow is remarkably consistent with that predicted by Crowley (2005) and shown in Fig. 3.25a.

Hao (2008) has reported more detailed analysis of aspects of the dynamics of the tides and residual circulation in the Crowley (2005) and Wilson et al. (2005a) model. Figure 3.26a and b show maps of the coastline of the Sound with the predicted mean flow vectors near the surface and at mid-depth, respectively. Some very large velocities appear in the model predictions that are likely to be associated with abrupt topographic and coastal irregularities, and are therefore very sensitive to model resolution.

The near surface circulation (Fig. 3.26a) shows a vigorous flow in the eastern Sound that is very similar to that predicted by the barotropic nonlinear layer model of Murphy (1979). To the east of the Hammonasset Point (HP in Fig. 3.26b) section, there is a strong (5–10 cm/s) current along the north shore of Long Island to the east and a westward flow of comparable magnitude on the north side of the Sound. These two features of the residual circulation appear to be connected by a southward flowing current to the east of the HP section to form the eastern Sound gyre (ESG). To the west of the HP section, the northeastward flowing surface waters from the central Sound are predicted cross the HP section near its center at approximately 10 cm/s, and then converge with the southward flowing waters on the western side of the ESG.

The across-Sound survey campaign of O'Donnell and Bohlen (2003) included ship-mounted acoustic Doppler current profiler measurements that allowed estimation and removal of the tidal period currents from their measurements. The red arrows in Fig. 3.26c show their estimates of the residual circulation at 5 m below the surface on April 26–28, 1995 at the HP section. Slow westward currents are present on the southern half of the section, and the strong eastward flow predicted by the model is evident in the central part of the section. The agreement between the location, width, and magnitude of this feature is excellent. O'Donnell and Bohlen (2003) show two other sets of observations from the HP section in April 1995 that display the same structure but with variation in the magnitude of the maximum currents of approximately 30 %.

Figure 3.26b shows Hao's (2008) prediction for mid-depth, approximately 10–15 m over most of the eastern Sound. To the east of the HP section, the general pattern of the predicted circulation is flow to the south and west though there is a northeastward motion between the HP section and the Connecticut River. On the southern half of the HP section, the model predicted mid-water flow is westward

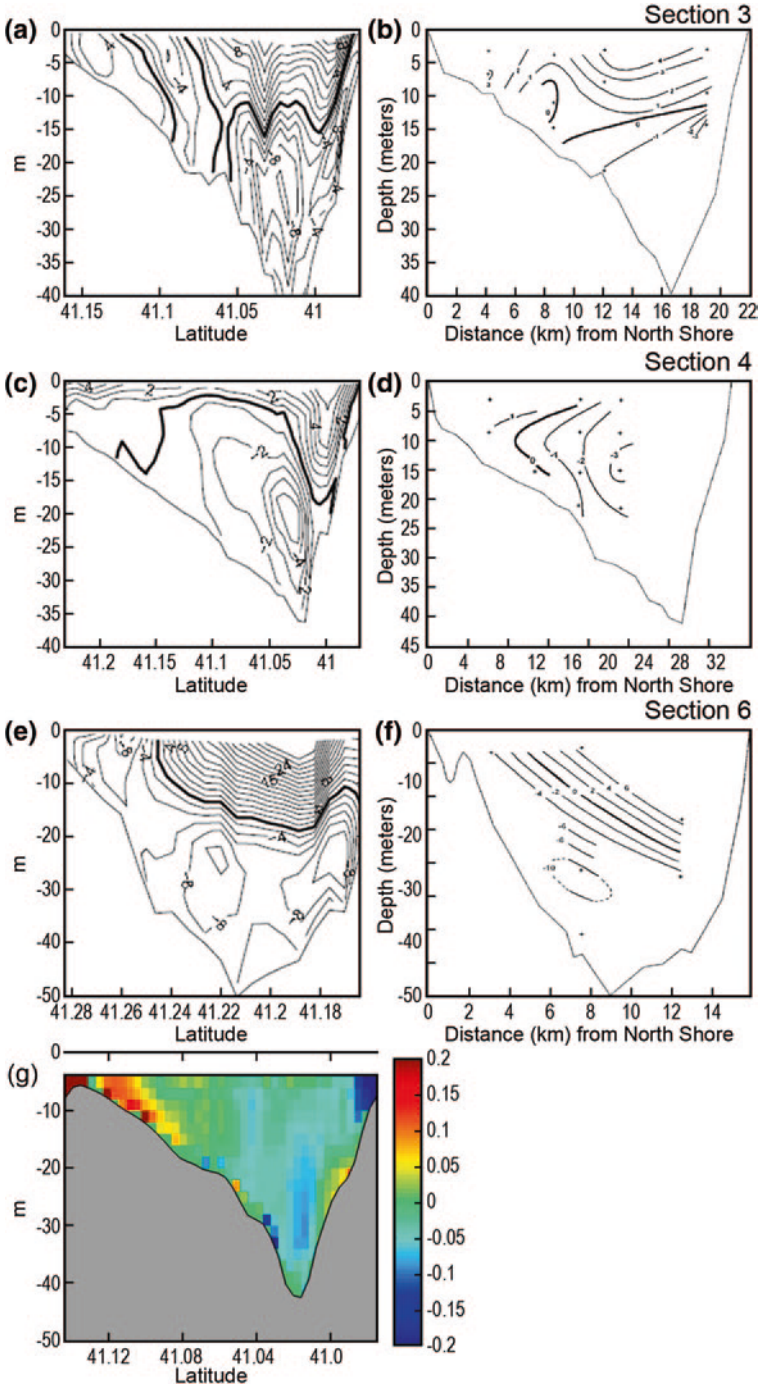
(a)
(b)
Section 3
Depth (meters)
Distance (km) from North Shore
(c)
(d)
Section 4
Depth (meters)
Distance (km) from North Shore
(e)
(f)
Section 6
Depth (meters)
Distance (km) from North Shore
(g)
m
Latitude
41.15 41.1 41.05 41
41.2 41.15 41.1 41.05 41
41.28 41.26 41.24 41.22 41.2 41.18
41.12 41.08 41.04 41.0
0.2
0.15
0.1
0.05
0
-0.05
-0.1
-0.15
-0.2

◀ **Fig. 3.25** Comparison of the mean along-Sound flow at sections 3, 4 and 6, (shown in Fig. 3.24) predicted by Crowley (2005) with the currents measured by Vieira (2000). **a**, **c** and **e** show the observations at sections 3, 4 and 6. These should be compared to the observations shown in **b**, **d**, and **f**. **g** shows the easterly component of velocity at, approximately, section 3 from the Bridgeport Ferry ADCP observations

at approximately 5 cm/s. The blue arrows in Fig. 3.26c show the O'Donnell and Bohlen (2003) observations at 15 m are consistent with the model predictions across most of the section. However, the observations indicate a westward motion at the northern end of the section that does not appear in the predictions. Other observations reported by O'Donnell and Bohlen (2003) suggest that this feature is more variable than the westward flow at the southern end of the section. Of course it may also be a consequence of wind or hydrographic variability not captured in the model.

Between the Stratford Shoals (SS in Fig. 3.26b) and HP sections, the near surface flow pattern predicted by the model (see Fig. 3.26a) is eastward along the southern shore with weak southwesterly flow elsewhere. A similar pattern appears at mid-depth in Fig. 3.26b. A more vigorous across-Sound circulation appears slightly to the east of the SS section, where the bathymetry shoals and the Sound narrow. At the southern end of the SS section a strong near surface current to the east is predicted

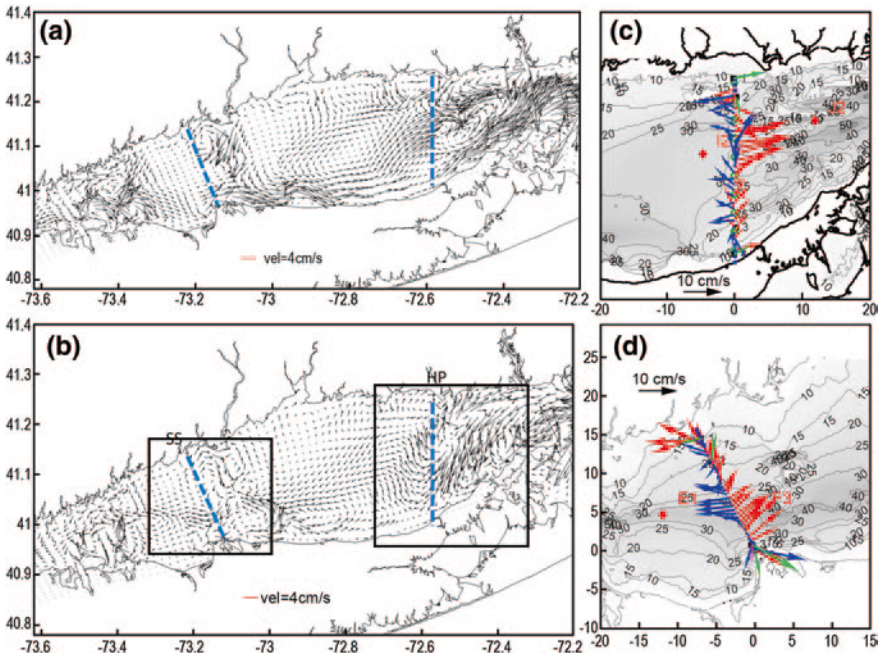

Fig. 3.26 **a** and **b** Show the near surface and mid-depth mean current vectors from the model of Hao (2008). The *black rectangles* and *dashed lines* show the location of the observations displayed in **c** and **d**. **c** and **d** Show the mean currents estimated by O'Donnell and Bohlen (2003). *Red shows* the vectors at 5 m and *blue* shows those at 15 m

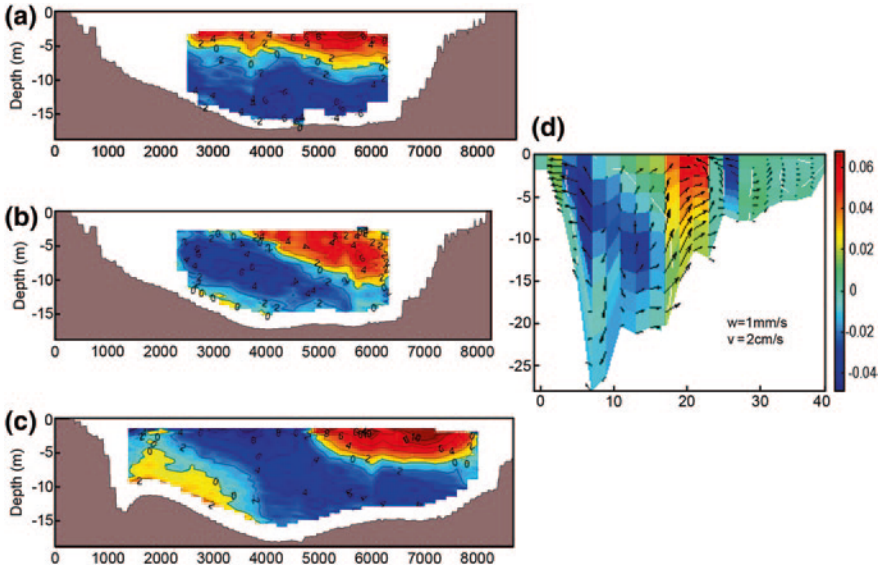

Fig. 3.27 Residual along-Sound velocity components at the LISICOS section (near Vieira's Sect. 3.1 in Fig. 3.21) observed in **a** March 2005, **b** July 2005, and **c** March 2006. Positive (*red*) values indicate eastward along-Sound flow and units are cm/s. The Connecticut coastline is on the left. Section (**c**) is located 3 km to the east of (**a**) and (**b**) where the Sound is wider. **d** shows predictions of Hao's (2008) model slightly to the east of Sect. 3.1. The *arrows* show the across-channel and vertical components. **a**–**c** are from Bennett (2010) and **d** is adapted from Hao (2008)

with a counter flow at mid-depth. Comparison of the red arrow in Fig. 3.26d with 3.26a, and the blue arrows in 3.26d with 3.26b, demonstrates that the model is reasonably successful in simulating the flow structure. Again there are discrepancies between the observations and predictions at the northern end of the section.

Bennett (2010) also used a ship-mounted ADCP to measure the velocity field during the hydrographic surveys described in Fig. 3.20. The along-Sound component of the mean flow for three intervals, (a) March 2005, (b) July 2005, and (c) March 2006, are shown in Fig. 3.27. The velocity components in Fig. 3.27c were obtained 3 km to the east of those in Fig. 3.27a and b where the Sound is slightly wider. In all three sections, the red colors show an eastward flow at 4–8 cm/s that is confined to a near surface layer adjacent to the Long Island shore. A westward flow (blue) fills the rest of the section. Though there are significant differences in the structure of the hydrography observed during these three transects, the structure of the velocity fields is quite consistent.

3.4 Seasonal Variability in the Circulation

The observations of O'Donnell and Bohlen (2003) and Bennett (2010) show that there is a tendency for eastward flow on the southern side of the Sound. However, their measurements were obtained only during light winds and for periods of a

few days at a time. More sustained observations of the lateral and vertical structure of the velocity field are available from two ferry-mounted ADCP systems. Codiga and Aurin (2007) report the analysis of the observations obtained from the New London to Orient Point Ferry along the section labeled OP in Fig. 3.24 at the eastern end of LIS. Stony Brook University operates a similar system on a ferry between Bridgeport, CT and Port Jefferson, NY in the central Sound along line 3 in Fig. 3.24. Using approximately eight sections per day during the period November 2002 to January 2005, Codiga and Aurin (2007) computed the average nontidal current in the lateral bins shown in Fig. 3.23a to reveal the seasonal variation of the nontidal flow shown in Fig. 3.28. In these figures, the coast of Connecticut (north) is on the right side, and the shaded areas indicate westward flow into the Sound. Note that the arrows show the across-channel velocity components and that the values above 7 m are not sampled by the ADCP because of the deep draft of the vessel.

There is a distinct lateral-vertical structure of the ELIS exchange flow, consisting of an eastward outflow that is concentrated in the south and near the surface together with a westward inflow that is concentrated near the bottom and toward the north (Codiga and Aurin 2007). This lateral-vertical structure is consistent with the predictions of the models of Kasai et al. (2000) and Valle-Levinson et al. (2003) in which the Coriolis acceleration modifies the exchange flow driven by the horizontal pressure gradient and resisted by bed stress. Codiga and Aurin (2007) address the dynamics in this area.

Subtle seasonal fluctuations in the along-Sound velocity components are evident in Fig. 3.28. The maximum inflow and outflow velocities of 25 cm/s are observed between May and August. In the winter, the maximum falls to 20 cm/s. This suggests that the rate of volume exchange between LIS and BIS is seasonally modulated; however, the areas of the inflow and outflow also vary, so Codiga and Aurin (2007) integrated the measured velocity component over the area of the section where it was directed inward and obtained 25,000 m^3/s from May to August, and 13,000 m^3/s from November to February. Since the bottom 10 % of the water column is not accessible to ship-mounted ADCPs, they extrapolated the measurements to the bottom and estimated the unmeasured transport. This adds approximately 5,000 m^3/s to the inflow flux estimate. The best estimate of the annual mean volume inflow is then 23,300 m^3/s. The model of Lee (2009) is consistent with this. The annual mean outflow must be comparable since the mean flux of fresh water from rivers and through the East River is an order of magnitude smaller. A very large fraction of the outflow occurs in the unmeasured near surface layer, so the net exchange remains uncertain. It is clear, however, that the volume flux may be much larger than inferred from the salt budget of Gay et al. (2004). These recent volume transport estimates must now be reconciled with the heat and salt budgets of the Sound.

Due to sampling limitations, observations alone do not provide an adequate description of the mechanisms that control the seasonal evolution of bottom T and S. Models provide an important adjunct to data interpretation and guide prioritization of additional measurements. For example, Crowley (2005) noted the presence

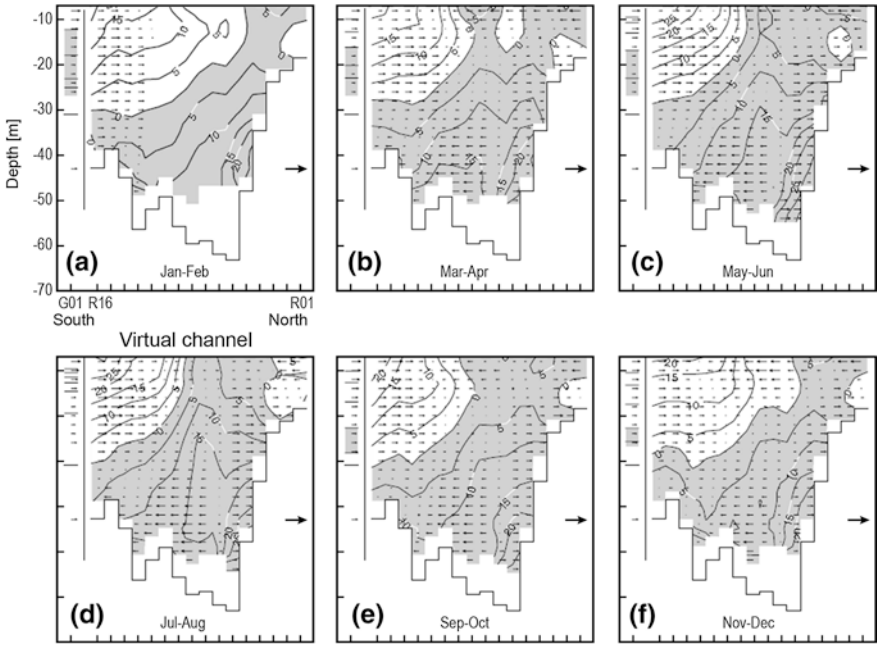

Fig. 3.28 Seasonal variation of the along-Sound residual flow observed by Codiga and Aurin (2007) averaged in two-month intervals. Note that the southern coast of the Sound is on the left and that the *shaded areas* indicate flow into the Sound (westward). Values above were not measured. The *vertical line* on the left side of each frame represents Plum Island and flow through Plum Gut, and segment G01 in Fig. 3.23a, appears to its left

of a pool of cold bottom water in the central Sound between Mattituck Sill and Hempstead Sill in her analysis of the CTDEP hydrographic archive. Figure 3.29a and b show the mean spring (April 12 through June 8) T and S distributions along the thalweg of the Sound (see Fig. 3.29c). Note that Fig. 3.16 shows that the cool pool warms through the summer but remains cold relative to the waters over the Mattituck Sill to the east and Hempstead Sill to the west. Crowley's (2005) model points to the importance of horizontal advection of warm saline bottom waters from Mattituck Sill to the warming of this pool and to the seasonal evolution of both bottom T and bottom S in the Sound. Crowley's (2005) Fig. 3.20 (not shown) emphasizes that this intrusion accelerates in July.

To examine the processes further, we analyze the seasonal variation in longitudinal density gradient across the sill from model results at stations on either side of the Mattituck Sill (Sect. 200 and 240 in Fig. 3.29c). Figure 3.30a shows the evolution of the haline and thermal contributions to the baroclinic pressure gradient across the sill. We see a period of maximum density gradient in July (days 180–200). The haline contribution (shown in green) is dominant and is associated primarily with an elevation in eastern boundary S. The thermal contribution to the baroclinic pressure gradient begins to increase through July as the basin warms

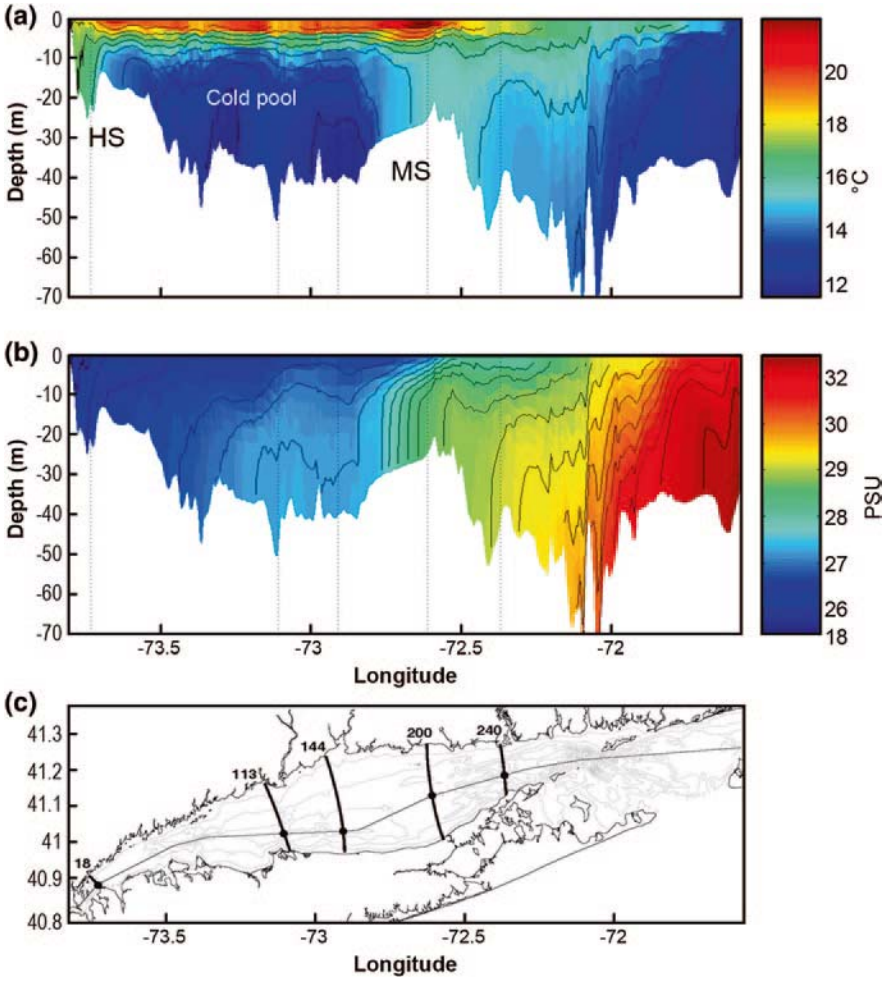

Fig. 3.29 Sections of seasonally averaged values of **a** temperature and **b** salinity along the thalweg of LIS for spring. MS and HS show the locations of Mattituck Sill and Hempstead Sill. **c** shows the coastline of the Sound and the location of the thalweg (from Crowley 2005)

due to surface heating (see red line in Fig. 3.30a) and it significantly augments the salt-induced stratification. Between days 100 and 200, stratification over the sill increases in June (days 160–180) as a consequence of heating (see red line in Fig. 3.30b). Though stratification is strongly modulated by monthly variations in the tidal mixing rate, it is clear that stratification increases significantly in July because the thermal-induced stratification is augmented by haline stratification. A more complete analysis of the interaction of the circulation and stratification can be pursued following the approaches of Holt and Proctor (2003) and Horsburgh et al. (2000) by computing from numerical solutions the rate of heat delivered by horizontal advection and that due to vertical turbulent diffusion. This calculation

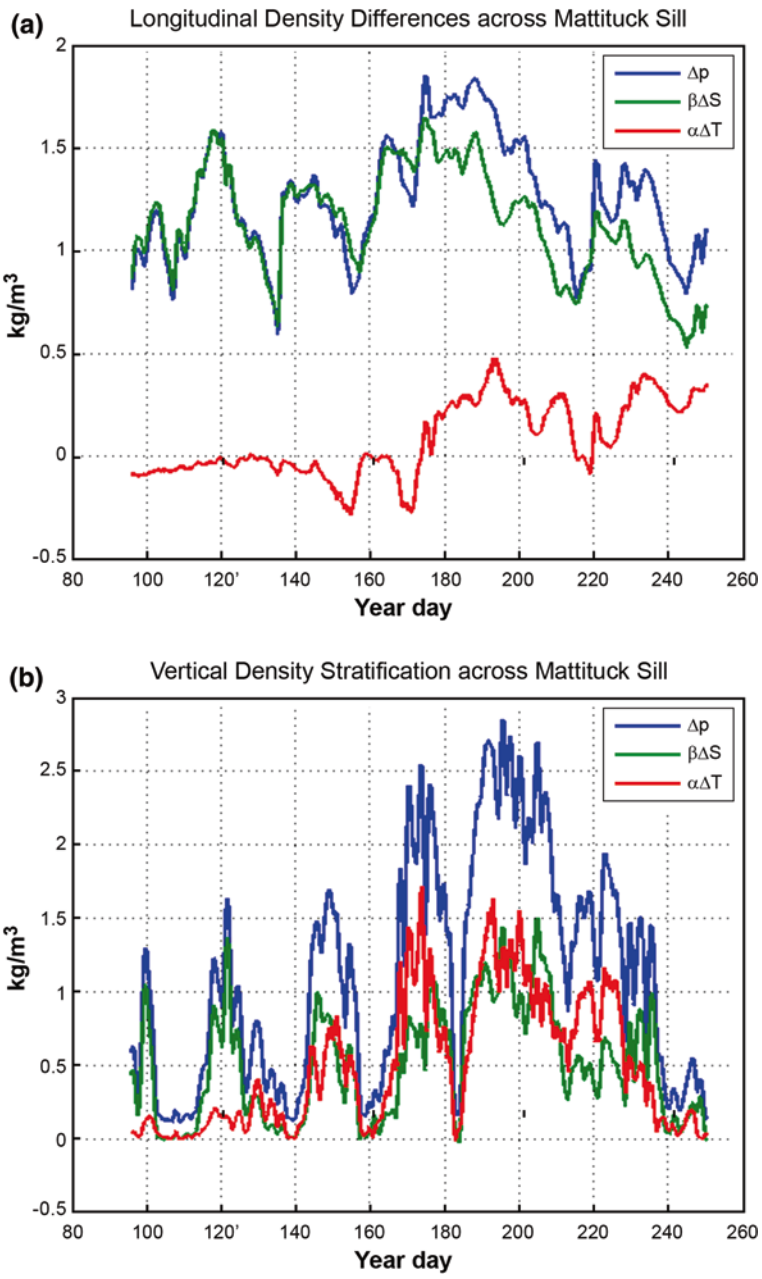

Fig. 3.30 **a** Contributions to difference in depth mean density at channel stations Sections 240 and 144, and **b** Contributions to surface to bottom density difference in density at the thalweg station on Sect. 200 (see Fig. 3.29c)

confirms that advection makes the dominant contribution to changes in sub-pycnocline *T* in the late summer. A similar analysis of the terms in the *S* budget also confirms the dominance of the advective contribution to the changes in the lower water column *S*.

It is important to note that the influence of topographic structures of 20–40 km scale, like the Mattituck Sill, can have an important role on the evolution of the Sound as a whole. Though the extensive archive of hydrographic observations upon which we relied for a description of the seasonal cycles in hydrography (Sect. 3.1.2) is very valuable, it is inadequate to resolve these important smaller scale structures. In Fig. 3.31a, we show a map of the bathymetry of the eastern Sound with the locations of seven stations occupied by a cruise in August 2002 and sampled in approximately a 6 h period. Figure 3.31b and c show the vertical structure of the *S* and *T* distribution observed along the cruise track. There is clearly an abrupt surface *S* front over the eastern side of the shoal with a *S* change of 1 over 5 km. A similar gradient is also evident near the bottom. The *T* field is similar on the eastern side of the shoal but there is also a near bottom *T* front on the western side between the waters of the central Sound cold pool and the warmer waters over the shoal. Codiga et al. (2002) observed similar behavior. The pressure gradients created by these fields are likely to drive significant across-Sound circulation and may play an important role in the enhancement of dispersion in the eastern Sound.

3.5 Synoptic-Scale Wind Forced Circulation

As in other estuaries, sea level varies due to winds blowing locally over the estuary (local effects) and due to wind-induced variations along the continental shelf (remote effects). Beardsley and Butman (1974) analyzed current and water level response to winter extra-tropical cyclones in the section of the Mid-Atlantic Bightfrom Nantucket Shoals to Sandy Hook, NJ. They showed that for cyclones passing to the south of Long Island, the current and sea level response could be described as a relatively simple Ekman response. Northeasterly winds contributed to an onshore Ekman transport and a rise in coastal sea level, and alongshore wind-driven currents were in approximate geostrophic balance with the pressure gradient associated with the across-shore sea level slope. Winds blowing axially along the estuary generate the largest local effects, while winds blowing along the continental shelf coast create the largest remote effects (Garvine 1985). During westerly winds in LIS, sea level is lower at the head and the surface is inclined upward toward the mouth (east) due to local effects and sea level is lowered throughout the estuary and along the shelf coast due to coastal upwelling dynamics (Bokuniewicz and Gordon 1980b; Wong 1990). During easterly winds, sea level is higher at the head and the surface is inclined upward toward the head (west) due to local effects and sea level is increased due to coastal downwelling dynamics along the shelf. Consequently, coastal flooding can occur when set-up from easterly wind events coincides with astronomical high tides. This was

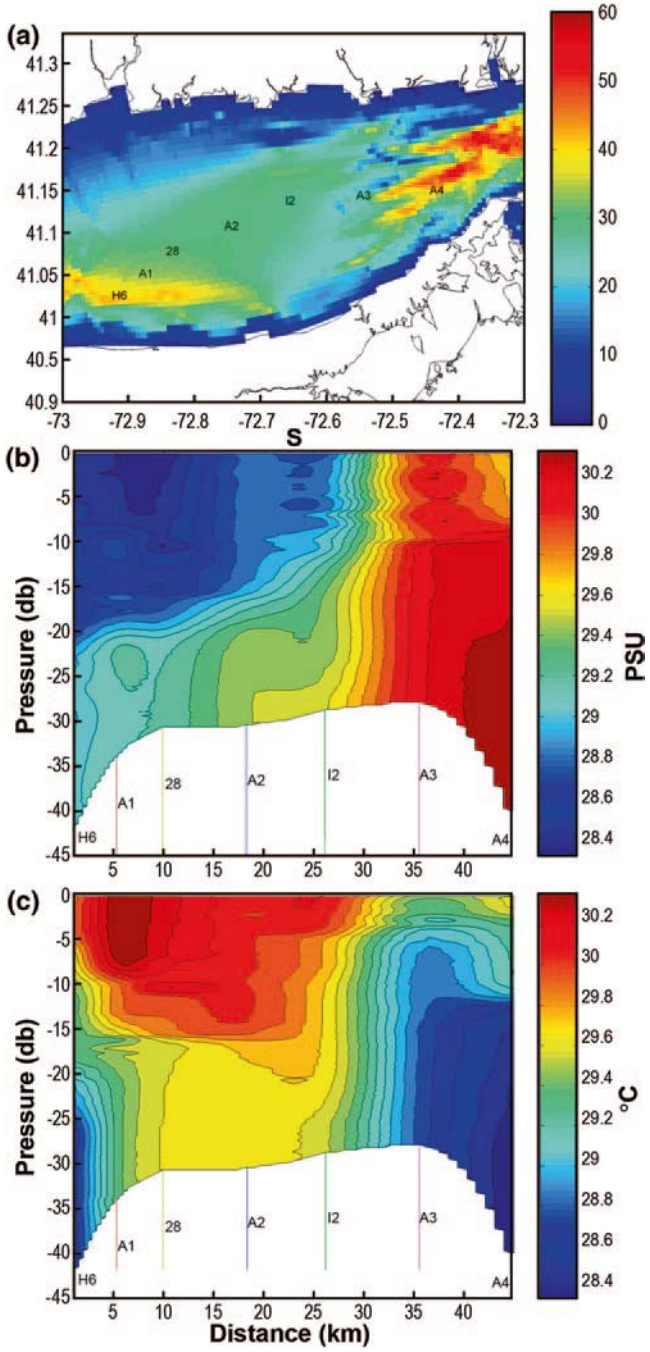

Fig. 3.31 **a** Bathymetry and Station positions for August 2002 SoMAS cruise across Mattituck Sill and the vertical cross-section of **b** salinity and **c** temperature

clearly demonstrated by Wong (1990) who used a year of observations of wind and sea level at stations in LIS to show that more than 80 % of the subtidal sea level variance was correlated with the east–west component of wind stress. Strong easterly and westerly winds (15 m/s, 0.37 Pa) associated with a winter storm passage generated sea level set-up and set-down with approximately 1 m amplitude (Bokuniewicz and Gordon 1980b). The relative importance of remote and local effects can be assessed by comparing sea level at Montauk Point on the shelf to the difference between sea levels at LIS stations and Montauk Point. Wong (1990) found the remote effects (with 0.12 cm standard deviation) are 2–3 times larger than the local effects, which are smaller in C LIS than WLIS (with 0.04 and 0.07 cm standard deviations, respectively). A section-averaged analytical model with wind stress, an along-estuary sea level gradient, and bottom friction compares favorably to observations and indicates the remote effect has a spatially constant amplitude, while the local response increases almost linearly toward the estuary head (Wong 1990).

It has been considerably more difficult to isolate the current response to wind events in LIS. These difficulties are due to the horizontal and vertical variability in currents, other subtidal signals (e.g., gravitational circulation and tide-generated residuals), the limited spatial coverage of moored observations, and the limited temporal coverage of shipboard observations. Gordon and Pilbeam (1975) found no correlation between near bottom currents from multiple locations in CLIS and wind speed and direction, though testing correlation with wind stress components may have helped. Ullman and Wilson (1984) concluded that subtidal currents through a lateral section in WLIS (south of Norwalk, CT) are significantly correlated with the along-estuary wind stress and sea level gradient; each variable is individually correlated with 36 % of the variance of the first spatial mode. Their analysis indicates a westward (up-estuary) flow at depth in response to the along-estuary pressure gradient generated by eastward (down-estuary) winds. Subsequent observations over the deepest area of this section (Schmalz 1993) also indicate an upwind flow response for near bottom currents. For this observational record, 62 % of the subtidal variance is correlated with along-Sound wind velocities and a 1 m/s wind corresponds to a 0.01 m/s current response (Signell et al. 2000).

Recently, Whitney and Codiga (2011) have used several years of data from the ferry-mounted ADCP on the section OP (see Fig. 3.24) to reveal the wind-event velocity anomaly fields. They identified period of westward and eastward wind with stress in excess of 0.1 Pa and averaged the de-tided and de-meaned along-Sound current components during those times to depict the effect of wind directions in the circulation patterns. Figure 3.32a shows the anomaly during intervals of eastward winds. Westward current anomalies (shaded blue in the figure) with 0.19 and 0.03 m/s maximum and mean values occupy most of the section. There is also evidence for downwind anomalies in the shallow areas on the south side of the section. The response to westward stress is shown in Fig. 3.32b. Again upwind current anomalies of similar magnitudes are evident in the center of the section, and these are flanked by near-surface downwind flow anomalies on both sides. Though there are no observations in the upper 7 m of the water column, it seems likely that current anomalies are

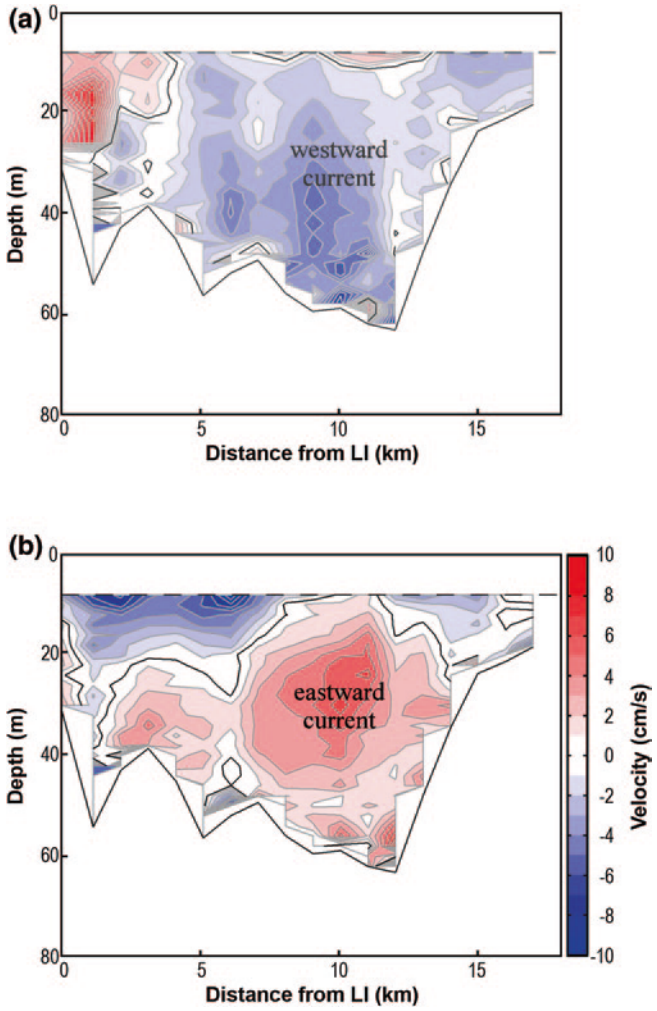

Fig. 3.32 Cross-section of observed wind-driven along-estuary velocity along the eastern LIS ferry transect: **a** wind-event velocity anomaly during westerly winds, and **b** wind-event velocity anomaly during easterly winds. The south side of the estuary is shown on the left. Eastward velocities are *shaded red* and westward velocities are *shaded blue*. The *dashed line* indicates the surface-most level observed

downwind close to the surface. The magnitude of the wind-driven anomalies is several times smaller than the total subtidal velocities at this location (see Fig. 3.28). The wind response tends to augment the mean subtidal flow and increase exchange with BIS during westerly winds and partially counters the background flow and reduces exchange during easterly winds (Whitney and Codiga 2011).

Numerical simulations are useful for studying the spatial structure of wind response throughout the LIS and diagnosing the controlling dynamics. Whitney

and Codiga (2011) analyzed model runs with tides, river discharge, and 0.1 Pa eastward and westward wind events to isolate the spatial structure of current vector anomalies. In Fig. 3.33a, we show that the current anomalies during eastward winds are downwind at the surface in most areas and fastest along each coast. Maximum magnitudes vary along the estuary from 0.15 to 0.42 m/s. The near-bottom velocity anomaly field is shown in Fig. 3.33b and is consistent with previous modeling results (Signell et al. 2000) that show downwind flow along each coast flanking upwind anomalies that are strongest in the deepest areas. The relatively weak wind response in the CLIS explains why Gordon and Pilbeam (1975) were unable to identify the wind response in observations, while the stronger response to the west accounts for the significant correlations in WLIS (Ullman and Wilson 1984; Signell et al. 2000).

The spatial structure of wind response is qualitatively consistent with analytical models including wind stress, sea level gradients, and friction developed by Csanady (1973), applied to estuaries (e.g., Wong 1994), and modified to include rotation by Winant (2004). The main features of surface-intensified downwind flow along the coasts flanking a deeper central upwind flow are present in analytical models and the wind-event anomalies in numerical simulations

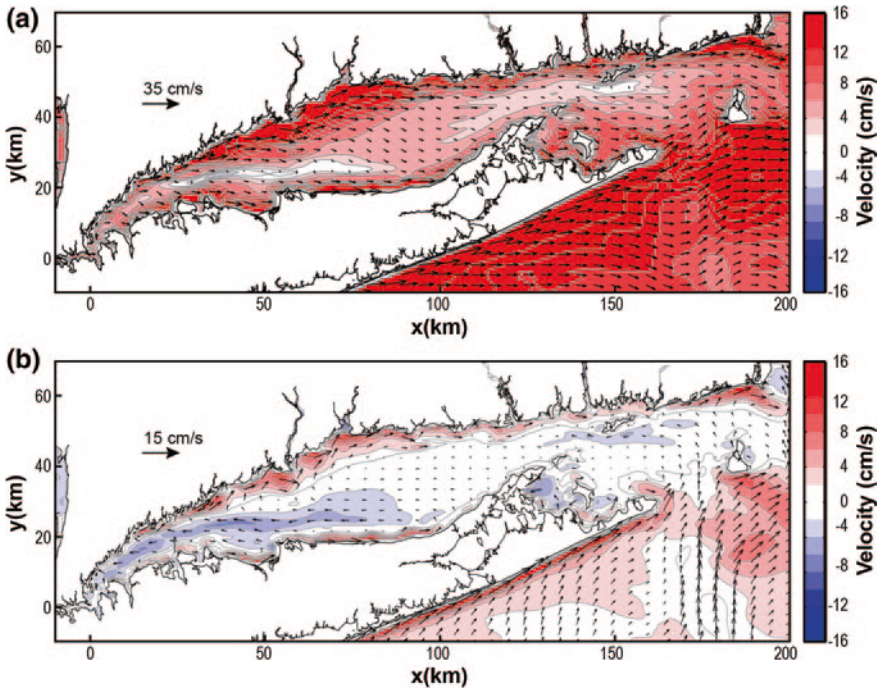

Fig. 3.33 Simulated wind-event anomalies during eastward (westerly winds) at the surface (**a**) and near the bottom (**b**). Velocity vectors are shown as arrows and the East–West velocity component is color-contoured with eastward velocities in *red* and westward velocities in *blue*

and observations. Simulation diagnostics of the section-averaged along-estuary momentum balance indicate the barotropic pressure gradient has the largest wind response. The response in bottom stress is significant, but responses in the Coriolis acceleration, advection, and the baroclinic pressure gradient (all typically neglected in analytic solutions) are equally important. The ratio of the maximum depth across a lateral section to the Ekman depth ranges from 1.7 to 4.8 in LIS, suggesting moderate importance of rotational effects (Winant 2004; Whitney and Codiga 2011). The cross-estuary flow in simulation results is due to this rotational influence (Fig. 3.33). The Wedderburn number (W) measures the relative magnitude of the along-estuary baroclinic pressure gradient and the wind stress (Imberger and Parker 1985). The estuary averaged W magnitude (0.5) indicates that dynamics are strongly wind influenced for 0.1 Pa events that are frequently experienced in the LIS (Whitney and Codiga 2011).

The mean structure of the density field and stratification are significantly modified by wind-induced advection, stirring, and isopycnal straining (Whitney and Codiga 2011). The Sound is characterized by large spatial variations in the sign and magnitude of horizontal density gradients and the intensity of stratification because of the location of rivers, the bathymetry, the subtidal circulation patterns, and variations in tidal mixing conditions. In many parts of LIS, wind-driven stirring, advection of stratification, and isopycnal straining (the change of vertical stratification by vertically sheared currents in a fluid with horizontal density gradients) work together to reduce stratification. In other areas, advection and/or straining work against stirring to limit the stratification reduction or actually increase stratification during wind events. The interplay between these factors changes considerably with wind direction and leads to asymmetries in the response to wind and makes the character of the response highly site-specific. It is likely, therefore, that the response described by O'Donnell et al. (2008a, b) in WLIS area will not be the same throughout the estuary. Additional observational and modeling research is needed to resolve the wind response throughout the LIS and to study wind influence on Lagrangian particle transport and exchange pathways.

3.6 Physical Processes Influencing Hypoxia

Hypoxia, or very low concentrations of DO, occurs in the bottom waters of the western Sound and East River in the summer (Welsh and Eller 1991; Kaputa and Olsen 2000). Two metrics have been adopted by LIS water quality managers to quantify the severity of hypoxia: the duration and the areal extent of hypoxic conditions. Observations from the survey program described Sect. 3.2 and Fig. 3.14 are used to monitor their trends. CTDEP (2009) has described sampling protocols, instrumentation, and methods for defining the two metrics from the data and the metric time series themselves. The New York City Department of Environmental Protection (NYCDEP) has executed a similar program and their station E10, the easternmost sampling location in the deepest part of the channel in the East

River (see Fig. 3.14), exhibits severe summertime hypoxia. Figure 3.34 shows the evolution of the mean May–October DO concentration computed using the CTDEP dataset. The 3 mg/l and 5 mg/l contours are shown. In April and May, the DO begins to drop below saturation in the waters deeper than 10 m and by May (Fig. 3.34a), the signal is evident between A4 and I2. The mean June DO is significantly depressed below 10 m in the western half of the Sound and the 5 mg/l contour then moves eastward to approximately 80 km in August. The bottom waters between A4 and C1 are below 3 mg/l. In the record of CTDEP observations, the earliest date of onset of hypoxia (DO less than 3.5 mg/l) in LIS was June 20 and the latest end date was September 26. The mean start and end dates were July 4 and September 9. Observations by the NYCDEP in the East River show similar start dates for the hypoxic period and a slightly longer duration.

To reduce the extent and duration of hypoxia, the States of Connecticut and New York developed a plan to reduce the amount of nitrogen (N) delivered to the Sound by wastewater treatment facilities (WWTFs) and agricultural runoff, which the US Environmental Protection Agency (USEPA) approved in 2001. Lee and Lwiza (2008) studied the CTDEP measurements obtained during the interval 1993–2004 and found that long-term changes in the extent and duration of seasonal hypoxia in LIS were not statistically significant. Since N discharges had been reduced, they proposed that they had not yet reached levels during late winter and spring that limit primary production. However, they did find that the inter-annual variability of hypoxic volume (the volume of water below the hypoxic threshold) was weakly correlated with variations in summer wind speed, spring total N, spring Chlorophyll *a*, and maximum springtime river discharge. The spring values for total N and Chlorophyll *a* were used because that is when maximum phytoplankton biomass concentrations occur and these were thought to determine the size of the organic carbon pool. The maximum river discharge was used to represent the fluctuations in vertical density stratification. Using multivariable linear regression, Lee and Lwiza (2008) found that these variables *S*, had a strong correlation with hypoxic volume fluctuations, but since the springtime total N explained the lowest fraction of the variance, they questioned the potential effectiveness of the N reduction strategy.

Torgersen et al. (1997) outlined a simple DO budget for the hypoxic region of the Sound and argued that there must be a substantial vertical or horizontal flux of DO to explain the difference between measured respiration rates and the rate of decline of near bottom DO over the summer. McCardell and O'Donnell (2009) used buoy observations to infer the magnitude of the vertical flux of heat and DO across the pycnocline and concluded that it was comparable to the vertically integrated water column respiration rates estimated by Goebel and Kremer (2007). O'Donnell et al. (2006 and 2008) also examined DO, and *T* series from moored instruments at the EXRK and WLIS sites shown in Fig. 3. These are near CTDEP stations A4 and C1 shown in Figs. 3.14 and 3.34, which are in the region of persistent summertime hypoxia. These records showed that the seasonal decline of DO in the bottom waters was intermittently interrupted by increases that they termed ventilation events. By correlating these periods with wind stress, they noted that

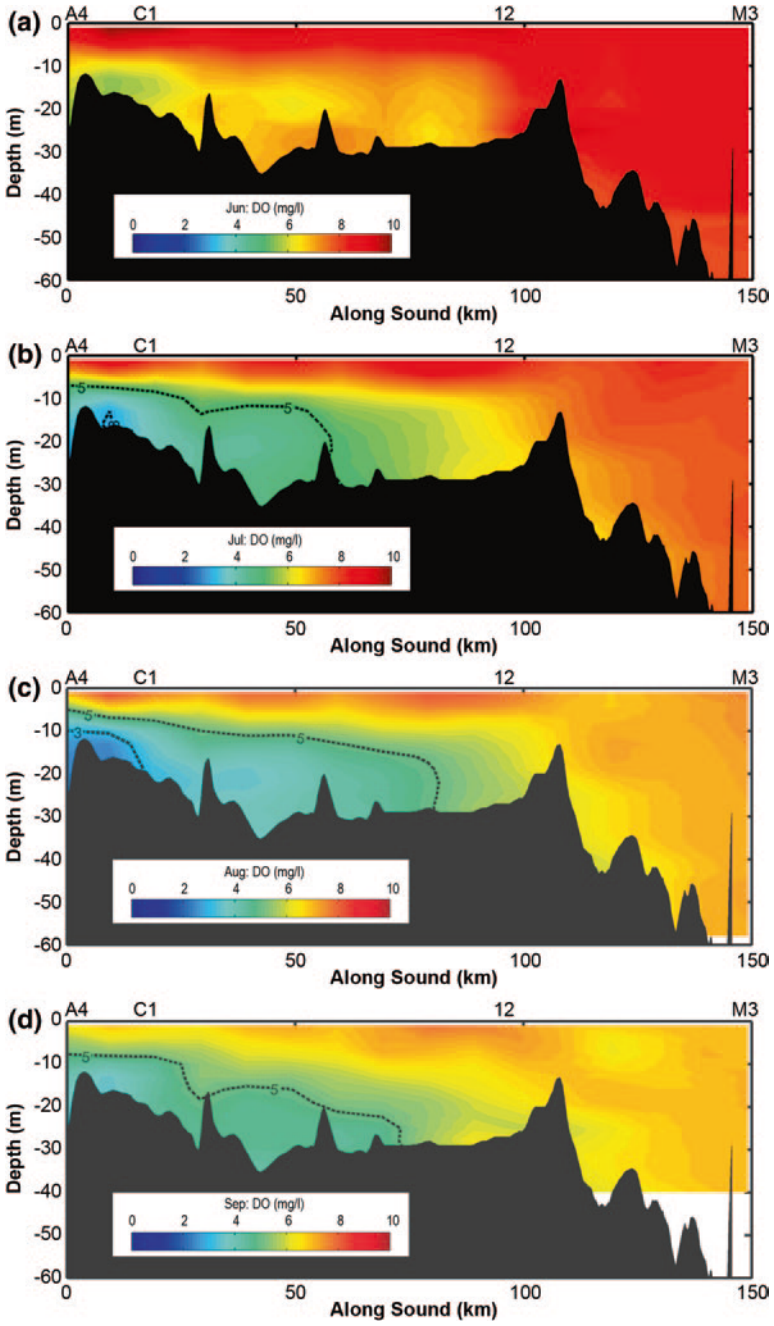

Fig. 3.34 Along-Sound cross sections of the distribution of dissolved oxygen concentration along the *dot-dash line* in Fig. 3.14 during **a** June, **b** July, **c** August, and **d** September computed by monthly averaging the CTDEP dataset and objective analysis

winds from the northeast generally coincided with ventilation. They proposed that the northeast winds modulated the buoyancy-driven circulation that brings fresh water from the East River into LIS to maintain the stratification that is constantly being reduced by tidal shear induced mixing. Scully et al. (2005) noticed the influence of wind on stratification in another estuary and referred to it as wind-induced straining. Contemporaneously, Wilson et al. (2008) used DO observations in the East River and a numerical model like that of Crowley (2005) to investigate the sensitivity of the stratification and DO in the western Sound to wind direction and also demonstrated quantitatively that straining was potentially important.

More recently, Scully (2010a) has demonstrated that inter-annual variations in the summertime volume of hypoxic water in the Chesapeake Bay are positively correlated with the duration of westerly winds and negatively correlated with the duration of southeasterly winds. Scully (2010b) then used a numerical model to investigate the mechanisms through which the extent of hypoxia in the Chesapeake is influenced by wind direction. He found that interactions between vertical mixing over shoal areas and lateral flows driven by winds from the south dominate the supply of DO to the hypoxic regions, whereas winds from the west are the least effective. Lateral advection was shown to be the most important mechanism producing ventilation rather than simple longitudinal or lateral straining suggested by O'Donnell et al. (2008a, b) and Wilson et al. (2008) as the important mechanism in LIS.

Wilson et al. (2008) used the NYCDEP observations at station E10 at the eastern end of the East River (see Fig. 3.14) to compute the time that bottom DO was below 3.5 mg/l using linear interpolation between samples. This is the hypoxia duration metric used by the CTDEP. The CTDEP summer hypoxia duration times series from 1991 to 2009 and the E10 duration time series when Winkler titrations were employed (1988–2006) were both 19 years in length with an overlap of 16 years. The correlation coefficient between the CTDEP hypoxia duration estimates for stations in CLIS and WLIS for 1991–2009 and the percent of hourly summer winds (in 40° bins) from different directions are shown in Fig. 3.35a. Experimentation showed that using wind data from June 1 to September 10 for each year and wind speeds above 3.25 m/s maximized correlations and minimized p-values, the measure of statistical significance (see Wunsch 2006). Using wind data from this period each year produced the same directional relationships as data from the extreme or mean range described above but with higher correlations. The high negative correlation for winds from the northeast (40–60°) is remarkable. For winds in the 40° bin centered on 50°, the correlation with hypoxia duration is -0.83 with a $\log_{10}(p$ value) of -5.03. High positive correlations and low p-values for winds from the northwest are evident in Fig. 3.35a. For winds in a 40° bin centered on 300°, correlation with hypoxia duration is $+0.74$ with a $\log_{10}(p$ value) of -3.53. Correlations with winds from other quadrants are not significant.

The correlation between hypoxia duration for 1988–2006 at NYC DEP station E10 and winds from different directions (Fig. 3.35b) affords a comparison between directional response at this western Sound station and that inferred from the distributed CTDEP stations (Fig. 3.35a). For this single station in WLIS,

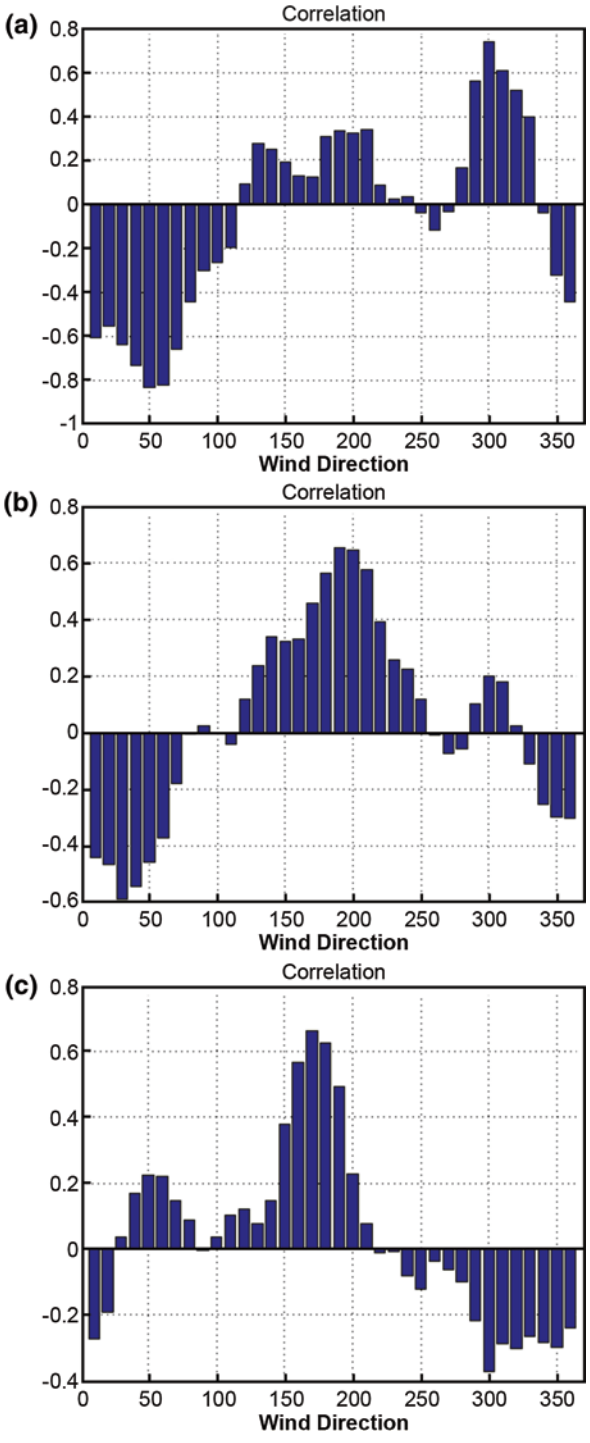

Fig. 3.35 Correlation between **a** CTDEP hypoxia duration, **b** NYCDEP E10 hypoxia duration, and **c** CTDEP hypoxia areal extent, and percent of winds in 40° bins from different directions for 1991–2009

results showed that using wind data from July 5 to September 1 for each year and wind speeds above 3.0 m/s maximized correlations and minimized *p*-values (increased statistical significance). High negative correlations and low *p*-values were found for winds from the north-northeast (20–40°). For winds in the bin centered at 30°, the regression coefficient was –0.60 with a $\log_{10}$(*p*-value) approximately −2.20. Very high positive correlations and low *p*-values were found for winds from the south. For winds from approximately 185° correlations are approximately +0.69 with a $\log_{10}$(*p*-value) of approximately −2.96. Correlations with winds from other quadrants are not significant.

The correlation between hypoxia areal extent for 1991–2009 for the distributed CTDEP stations and winds from different directions (Fig. 3.35c) affords description of the directional response for this metric. Analyses showed that using wind observations from June 20 to August 20 for each year and wind speeds above 3.0 m/s maximized correlation with areal extent and minimized *p*-values. High positive correlations and low *p*-values are found for winds from the south. For winds from approximately 165° correlations are approximately +0.67 with a $\log_{10}$(*p*-value) of approximately −2.75. Correlations with winds from other quadrants are not significant.

Correlations in Fig. 3.35a point to a statistically significant relationship between inter-annual variations in summertime hypoxia duration at the CTDEP stations in CLIS and WLIS and wind direction. Winds in a 40° (all compass directions are true north) bin centered on 50° are strongly negatively correlated with variations in duration and so influence the ventilation of bottom waters. At the NYCDEP station E10 in the far western Sound, winds in a bin centered on 30° are strongly negatively correlated with variations in duration (Fig. 3.35b). To interpret the variations in directional response, it is useful to consider the orientation of the thalweg developed from gridded bathymetry used in numerical simulations by Crowley (2005) and Hao (2008). The thalweg heading varies between 60° and 70° with the west central Sound, and it decreases rapidly toward the far western Sound. Winds from 50° are rotated counterclockwise approximately 15° from the thalweg in the west central Sound; winds from 30° have the same orientation relative to the thalweg near E10. The directional response is not inconsistent with wind-induced straining of a longitudinal density gradient, and the 15° deflection could indicate an influence of rotation causing some transport to the right of the wind. The 15° deflection could also indicate that straining of a lateral *S* gradient is important or that lateral advection as described by Scully (2010b) contributes to ventilation of bottom waters. It is useful to note that exactly the same directional relationships are obtained if only the overlapping 16-year period of 1991–2006 between the CTDEP and NYCDEP data is considered.

At NYCDEP station E10, winds in a bin centered on 190° are strongly positively correlated with inter-annual variations in duration (Fig. 3.35b). This is consistent with the straining of a longitudinal density gradient, although at this station winds are again deflected counterclockwise relative to the thalweg orientation. Unlike the response at E10, Fig. 3.35a indicates that for the CTDEP stations, winds in a bin centered on 300° are strongly positively correlated with variations

in duration and so presumably contribute to the rate of restratification. In the more open waters represented by the CTDEP duration metric, winds from the northwest contribute to the maintenance of stratification. This is consistent with straining of a longitudinal density gradient, but winds from 300° do have a significant component normal to the thalweg. This directional response in these open waters is more distinct from that in the constricted waters of the far western Sound.

The inter-annual variations in areal extent of summertime hypoxia are positively correlated with winds from the south-southeast (Fig. 3.35c). Because of longitudinal variations in the orientation of the channel, these winds would contribute to straining of the longitudinal density (S) gradient in the western narrows near E10. In the west central Sound, winds from this direction would contribute to straining of the lateral density (S) gradient.

Figure 3.35a shows that hypoxia duration in the more open waters of the west central Sound is reduced when synoptic winds are from the northeast. Winds from the northwest are associated with an increase in duration. In the far western Sound (E10), winds from the northeast reduce hypoxia duration, while winds from the south contribute to increased duration. Southerly winds also contribute to increased hypoxia areal extent in the west central Sound. Inter-annual variations in synoptic period variability have significant influence on both duration and areal extent.

Further insight into the response of water column structure and mixing to synoptic events, specifically to summertime northeasters and northwesters, can be obtained by analyses of three-dimensional hind-cast numerical model simulations. The model used is described by Crowley (2005), Wilson et al. (2005a), and Hao (2008). We focus here on a description of transient water column structure in a single lateral section in the western Sound centered on −73.51°. This section is close to that of Bennett (2010), shown in Fig. 3.14b. At this section, the orientation of the thalweg is approximately 67 °T. To the west, the basin becomes narrower and the thalweg orientation becomes more northerly.

The summertime northeaster described by Wilson and Swanson (2005) is known to have produced significant mixing. Hindcast simulations for the wind forcing shown in Fig. 3.36 illustrate the evolution of water column structure during the event (Fig. 3.37). The most distinctive feature is downward tilting of the isopycnals on the south side (left) of the transect and the advection of deep water from the channel up into the shallows on the north side of the transect where it is mixed vertically. The low-pass filtered lateral velocity (not shown) is consistent with this advection of bottom waters toward the north side of the transect. This is consistent with mechanisms described by Scully (2010b). At the same time, the low-pass filtered longitudinal velocity (not shown) shows clear evidence of a destratifying strain with bottom velocities directed toward the east and surface velocities directed toward the west. This combination of processes contributes to very significant water column destratification and produces strong lateral density gradients that then adjust under gravity. So winds from the northeast can promote both lateral advection and a destratifying longitudinal strain.

Analyses of hindcast simulations for a number of northwesters show a similar evolution of water column structure. The northerly component of wind stress again

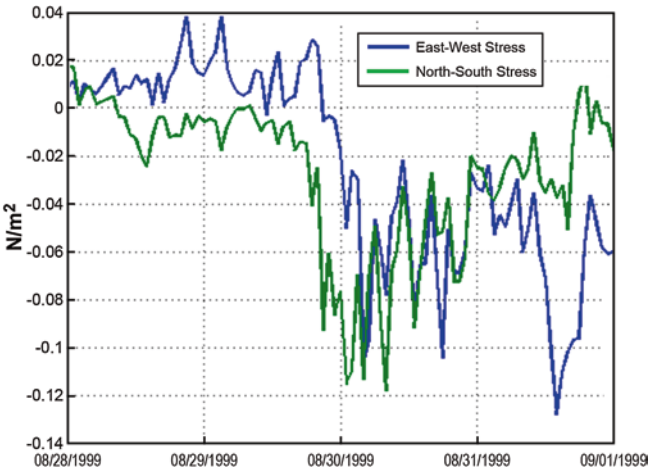

Fig. 3.36 Wind stress components for summertime northeaster simulation

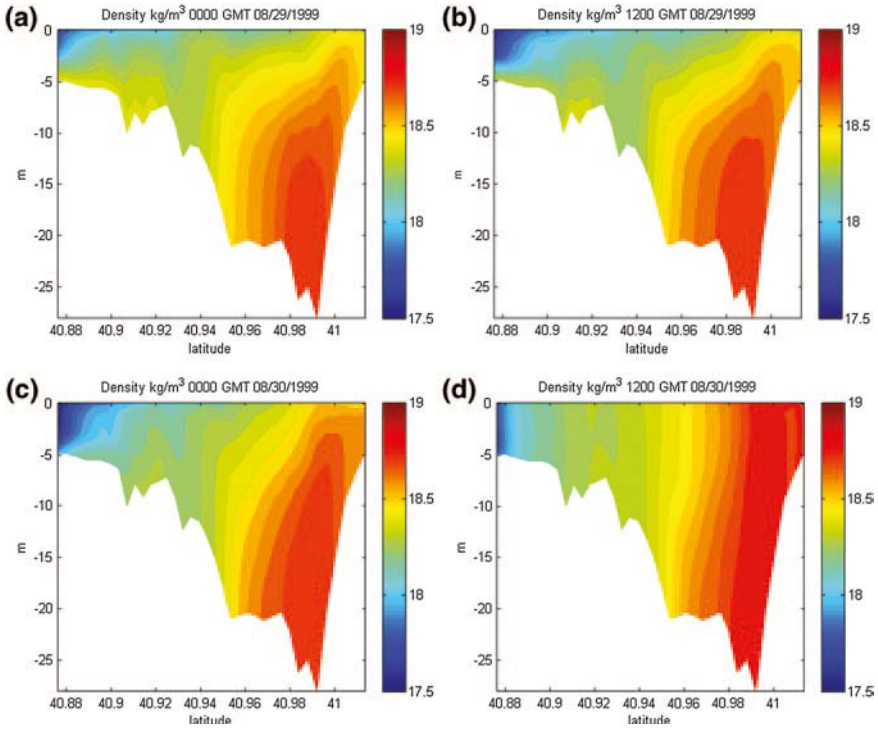

Fig. 3.37 Lateral density structure at **a** 0000 GMT 08/29/1999, **b** 1200 GMT 08/29/1999, **c** 1200 GMT 08/30/1999, and **d** 1200 GMT 08/30/1999. Note that the low density fluids and the south shore of the Sound are on the left of the figure

contributes to the lateral advection of the bottom waters in the channel toward the north side of the transect. The westerly component of wind stress apparently contributes to a stratifying longitudinal strain so the water column doesn't undergo the destratification that occurs under a northeaster. Hindcast simulations for periods with southerly winds characterized by diurnal sea breeze show relatively little response of water column structure to this type of forcing. This prediction must be assessed by comparison with observations and the response of embayments must be investigated.

3.7 Climate Change and Inter-Annual Variability

We have reviewed our understanding of the processes that influence the circulation and structure of LIS and affect hypoxia. It is clear that there are long-term variations in the large scale forcing mechanisms. However, much of our observation database is short-term. It is, therefore, very important that we consider the impact of climate change and inter-annual variability on our understanding.

Recently Whitney (2010) showed that annual cycles in S at the eastern end of LIS do not have the same characteristics as other LIS stations. Lee and Lwiza (2005) also commented on this. For example, there is a similar trend of S variability between stations F3 and M3 (see Fig. 3.14) on a longer time scale (>2 years), but their characteristics on shorter time scales (i.e., subseasonal) are different. This is explained very well in Gay and O'Donnell (2007 and 2009) who argue that the runoff distribution and the geometry of LIS drive a net flux of salt toward the west, which explains the negative curvature of the S profile at the western end of LIS. Lee and Lwiza (2005) have shown that on an inter-annual scale, direct precipitation in LIS does not significantly affect the S in LIS.

The river runoff, on the other hand, can influence the S in LIS with most of it coming from Connecticut River discharge, as it comprises 70 % of the total freshwater discharge into the Sound (see Fig. 3.1). Compared to depth-averaged S, the surface S of LIS is more influenced by river discharge (see Whitney 2010). Salinity records in LIS are too short to draw an unequivocal conclusion about its relationship to climatic processes that operate on longer time scales, decadal to multidecadal such as the NAO. Preliminary evidence from the Chesapeake Bay seems to indicate there might be some correlation to NAO. It is not yet clear whether NAO is manifested through its weak relation with river discharge or by directly affecting the adjacent shelf water. Whitney (2010) found that positive correlations between shelf and LIS surface S are stronger than with rivers, and can explain up to 82 % of the low-passed data with time lags of 0–2 months.

T in LIS is mainly dominated by seasonal variation with the minimum T occurring in February and the maximum in September. The annual range of the minimum and maximum T is higher in the western Sound (~0.7°–22.6 °C) than in the eastern part (1.0°–20.5 °C). The depth-averaged T contains larger inter-annual variability in winter than in summer. For example, the variance of depth-averaged T in the CLIS is 1.9 $°C^2$ in February and 0.2 $°C^2$ in September (Lee and Lwiza 2005).

The magnitude and the timing of the inter-annual variations of *T* in ELIS do not appear to be correlated with those in WLIS. For example, negative anomalies from the summer of 1992 to early 1994 seen at station F3 are larger than at station M3, and strong negative anomalies at station M3 in the winter of 1996 are hardly noticeable at station F3. This uncharacteristic differential heating has yet to be fully explained. Based on a seasonal time scale, Crowley (2005) showed that the estuarine circulation makes a relatively large contribution to the net heat transport during the stratified period and thus the exchange heat transport represents a loss of heat in LIS. Recently Lee (2009) used a numerical model, ROMS, to demonstrate the importance of horizontal advection, which cools the water column during spring-summer. The model results also indicate that spatial patterns of heat flux due to horizontal advection are driven by the longitudinal mean current whose momentum balance is between pressure gradient and advection, agreeing with the results of Hao (2008). In addition, Lee's (2009) results indicate that the net surface heat flux is the major mechanism that controls the heat storage during fall-winter. Evidently, further research is required to understand the mechanisms that control the inter-annual variability and longer time scales of evolution of *T* in LIS.

Since *T* in LIS is mainly affected by surface heat fluxes in fall-winter (Lee 2009), then the winter warming trend that has been reported (e.g., Stachowicz et al. 2002) is most likely driven by the regional climate change. Horizontal advection plays a minor role transporting the relatively warm water from BIS into LIS. During spring–summer, the role of horizontal advection is reversed (heat loss) and becomes important in the variability of *T* is possibly associated with adjacent shelf sea water. Long-term *T* changes also tend to affect trophic structures of the ecosystem. Although there has not been a systematic analysis done in the whole of LIS, evidence from neighboring habitats seems to point in that direction. In Narragansett Bay, taxonomic diversity has increased over time as the community shifted from fish to invertebrates of several phyla. The shifts in species composition correlate most strongly with spring-summer sea surface *T*, which increased 1.6 °C between 1959 and 2005 (Collie et al. 2008). Species composition is also correlated with the winter NAO index and the chlorophyll concentration, which has declined since the 1970s. Triggered primarily by rising *T*, these decadal changes have altered the trophic structure of the nekton community, resulting in a shift from benthic to pelagic consumers. Keser et al. (2005) have shown that the *T* in ELIS increased by 1 °C between 1979 and 2002, favoring the growth of knotted wrack (*Ascophyllum nodosum,* also commonly called bladder wrack)—an intertidal brown alga. However, their study also indicates that if the *T* continues to rise past 25 °C knotted wrack will die. Invertebrates are also affected by *T* variability; for example, the population of the tunicate *Diplosoma listerianum* only thrives if winter *T* stays above 4 °C. Recruitment failure occurs when *T* falls below 4 °C.

Long-term changes in surface *T* in LIS differ markedly between winter and summer. While winter temperatures have been shown to increase, the change for summer has been almost negligible (Lee and Lwiza 2005). Wilson et al. (2008) reported that the increase in thermal stratification in the WLIS during summer months (July and August) from ~0.5 to 2 °C between 1946 and 2006 was mainly

due to the decrease in bottom T (see Fig. 3.38). It is proposed that the bottom T decrease is associated with the change in the wind regime. The change in the dominant wind direction during summer time has increasingly favored wind-induced straining as described by Scully et al. (2005) and O'Donnell et al. (2006). Since 1946, the mean wind direction has gradually been approaching 203 °T, which is the optimal direction for producing vertical stratification.

Light availability plays a critical role in triggering the initiation of spring blooms in marine ecosystems (Townsend et al. 1994; Iriarte and Purdie 2004). The inter-annual variations of surface irradiance are influenced by atmospheric conditions, especially cloud cover. Recent literature shows that there is significant inter-annual and decadal variability of the Earth's albedo, which is influenced by changes in cloud location, amount, and thickness (Palle et al. 2006). Figure 3.39a shows the 21-year average of the mean cloud cover over the continental US and the surrounding oceans during the winter months of January, February, and March (JFM) from 1984 to 2004. The Great Lakes effect on cloud cover can be clearly seen, and the northwest Atlantic region is characterized by high cloud cover of approximately 90 %, with a sharp gradient toward the coast. As the cold continental air moves over the warm sea surface, it rises to form the stratocumulus clouds over the Atlantic. The rest of the northeast region follows the continental climatology.

Figure 3.39b shows the sum of the three leading modes of the empirical orthogonal function (EOF) of cloud cover, which represents inter-annual variability. The Middle Atlantic States, and particularly the southern New England region, exhibit

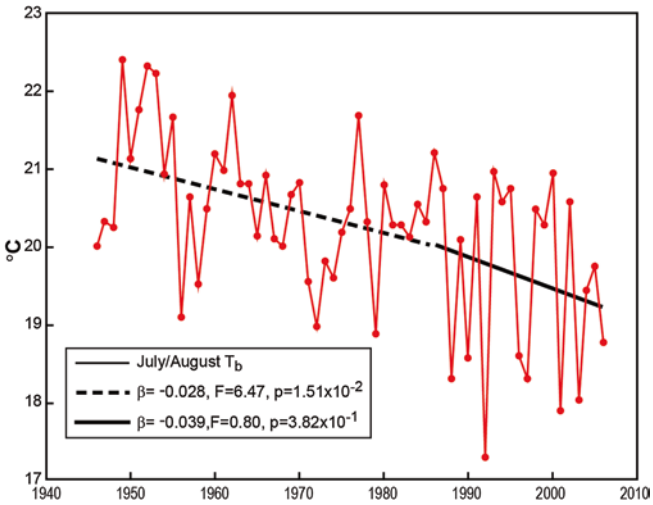

Fig. 3.38 Time series for bottom temperature at NYCDEP E10 averaged over July and August (Wilson et al. 2008)

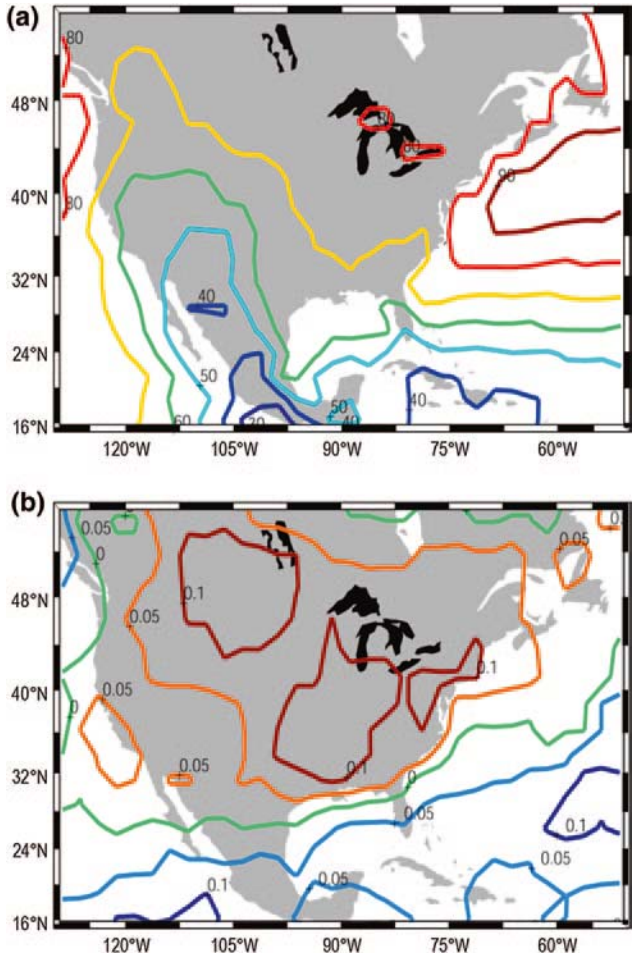

Fig. 3.39 **a** Winter mean cloud cover (%) for the months of Jan–Mar (1984–2004). Note the high cloud cover off the northeast US where there is a permanent stratocumulus cloud and **b** Sum of the three leading modes of the EOF of cloud cover shown in (**a**). Data source: ISCCP from NASA

high variability, which is likely to influence the amount of shortwave radiation reaching the surface. Shortwave radiation can be reduced by as much 16 % during winter months with high cloud cover (Fig. 3.39b). Such a significant decrease will affect the amount of solar radiation available for photosynthesis, particularly in the period of the spring bloom. One might expect that increases in shortwave radiation result in increases in surface air T. However, analysis of long-term datasets tends to suggest the opposite response. Warm winters lead to high cloud cover and low shortwave radiation, e.g., 1971, 1974, 1982, and 1988.

3.8 The Influence of Severe Storms on LIS

Extra-tropical cyclones (northeasters) are the major weather makers in New England. Most extra-tropical cyclones develop as low-pressure systems in the southern States that are then drawn to the northeast by the jet stream. The northeast track brings the system along the east coast past the mid-Atlantic and New England coastal states. Divergence in the upper atmosphere disburses the rising air at a faster rate than it is replaced at the surface, which, in conjunction with the Coriolis effect, causes the cyclone to intensify. In the lower atmosphere, the cyclonic winds bring warm, moist oceanic air over land where it meets colder, drier continental air. The greater the T differences between these two air masses, the more severe the storm can become. Though they occur throughout the year, they are usually more intense in fall and winter because of the large T differences between the converging tropical and continental air masses.

To guide analyses of the oceanic response to such storms, a model of the evolution of the meteorological forcing fields during an east coast extra-tropical winter cyclone has been developed by Mooers et al. (1976) as a composite of 34 extra-tropical cyclones affecting the area during the 1972–1973 and the 1974–1975 winter seasons. The model cyclone passes across the east coast between Cape May and Kiptopeake Beach. It then travels over open water toward the northeast at a speed of approximately 11.8 m/s; the central pressure drops from 1,002 mb to 995 mb over a period of 36 h and the size of the system increases.

The highest wind speeds observed in the LIS area are associated with hurricanes, or tropical cyclones. These form in the tropical North Atlantic and drift westward in June to October. Occasionally, they intensify in the Caribbean Sea, Gulf of Mexico, or over the Gulf Stream off the Carolinas, and then track northeastward across New England. Figure 3.40 shows the tracks of hurricanes identified by Colle et al. (2010) that led to surges of between 0.6 and 1 m at The Battery, NY. Only 13 named hurricanes have tracks that crossed LIS in the last 50 years so the structure and evolution of the wind fields and the sea level responses are only well resolved for a few major events. However, Phadke et al. (2003) have developed a parametric representation of hurricane wind fields that is useful for model sensitivity studies and engineering design applications. It requires specification of the storm track, forward speed, center pressure, and the radius at which maximum wind occurs. This allows simulation of the ocean response to infrequent major storms.

The most damaging aspects of tropical and extra-tropical cyclones are the flooding resulting from the combination of storm surge, freshwater accumulations, and wind wave set-up. Of these, the storm surge is usually the major culprit. Storm surge is a rise in water level along the coast due to the action of wind stress in combination with an inverted barometer effect and, as outlined in Sect. 3.5, this is sensitive to regional coastline geometry and bathymetry. The extent of flooding is also sensitive to storm timing of the storm surge relative to high tide. Much of the developed coastline around LIS, New York, and New Jersey is less than 3 m

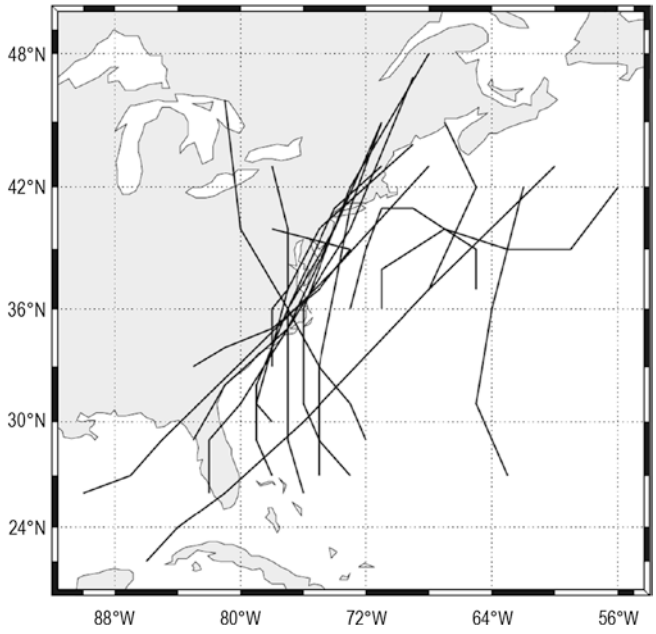

Fig. 3.40 The 48 h tracks of tropical cyclones that led to surge heights of 0.6–1.0 m at the battery between 1959 and 2007. From Colle et al. (2010)

above mean sea level making the region highly vulnerable to storm surge flooding from both extra-tropical and tropical storms. For example, the yellow shade in Fig. 3.41 shows the area of land in the altitude range 0–3 m above mean high water. Clearly the densely populated region of the western Sound is very vulnerable to inundation.

Zhang et al. (2000) have analyzed historical storm activity associated with both extra-tropical and tropical cyclones as it is reflected in storm surge records in century-long sea level series at stations along the east coast of the USA. This analysis is relevant because it includes both Sandy Hook and The Battery. Records are analyzed for storm count, duration, and a measure of intensity. The study affords a description of both seasonal and inter-decadal variability. More recently, Colle et al. (2010) have produced an updated climatology of the characteristics of both extra-tropical and tropical cyclones that produce surge events in New York Harbor as represented by sea level at The Battery. They addressed the complex question of how wind speed and direction evolve in the vicinity of New York Harbor for both weak-surge and moderate-surge events. They also defined the cyclone positions and tracks that favor storm-surge events for the harbor area.

Colle et al. (2010) defined minor surges to be between 0.6 and 1 m above the predicted tide level and showed that there was substantial inter-annual variability in the number of these surges each year and highlighted evidence of a reduction in the frequency of these events. However, the sea level record at The Battery shows

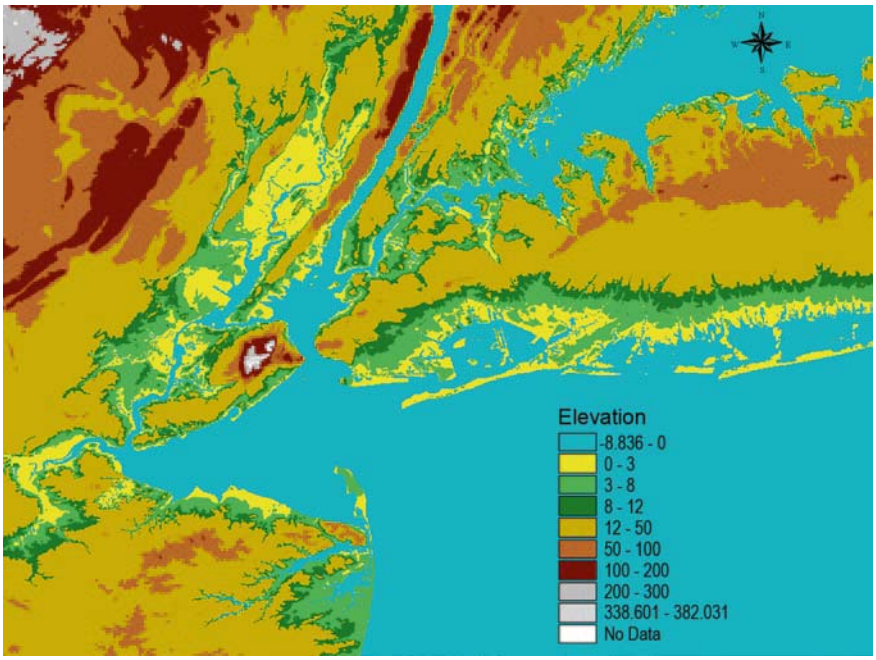

Fig. 3.41 Topographic contour map for the New York metropolitan region; elevations in meters (from Bowman et al. 2005)

that flooding, as measured by the total water elevation above mean high water, has increased. When the effect of long-term sea level rise, 2.8 mm/year at The Battery, was subtracted from the data record, the increasing trend in flooding was eliminated. This shows that a relatively small change in the water level can significantly influence flooding statistics.

The response of sea level in the New York Bight and WLIS to major storm events has been studied recently by Bowman et al. (2005) and Zheng (2006) using numerical simulation. Zheng's analyses confirmed the importance of direct set-up in WLIS, as described by Bokuniewicz and Gordon (1980b), and the coastal Ekman response described by Beardsley and Butman (1974). She found that coastal sea level was highly correlated with the component of wind stress toward 240°, which is essentially coast parallel with zero time lag; a linear relationship between Sandy Hook surge and wind stress toward 240° has a correlation coefficient of 0.89 and a sea level increase per unit wind stress of 1.5 m/Pa. She also found that sea level at Kings Point was highly correlated with the component of wind stress toward 270° with a time lag of approximately 4 h; a linear relationship between Kings Point surge and lagged wind stress toward 270° has an R of 0.92 and a gain of 4.5 m/Pa. A northeaster with this track did not produce any significant westerly winds during its transit and observations showed no evidence of a set-down at Kings Point. Consistent with the response described by

Bokuniewicz and Gordon (1980b), the surge at Montauk lagged that at Kings Point by approximately 2 h. Zheng found that because the Kings Point surge lagged that at The Battery and had significantly greater magnitude, a subtidal sea level slope was maintained across the East River for approximately 12.5 h, producing a subtidal volume flux toward the harbor with peak magnitude of approximately 2×10^5 m^3/s and a total volume transported into New York Harbor by the storm of approximately 4.5×10^9 m^3.

Hurricane Floyd (September 7, 1999) was fast moving with a track directly across western Long Island that was analyzed through hindcast simulations by Bowman et al. (2005). Atallah and Bosart (2003) described the extra-tropical transition of this storm. The sea level response to such a fast moving tropical cyclone exhibits differences both within the Sound and on the open coast from that of a slower moving extra-tropical cyclone with track to the south and approximately parallel to the island. Time series for lowpass filtered sea level at The Battery, Kings Point, and Montauk (Fig. 3.42a) show the character of the surge response during passage of this storm beginning on September 16, 1999. At the beginning of the storm, strong easterly winds created a set-up of approximately 0.6 m. Subsequently strong westerly winds led to a set-down. Maximum surge levels occurred at Kings Point (green line) in the western Sound.

The directional response at Kings Point to LaGuardia winds (Fig. 3.42b) is very well defined; surge level is highly correlated ($R = 0.83$) with the component of wind stress toward 270°, but with a time lag of approximately 7 h. A linear relationship between Kings Point surge and lagged wind stress has a gain of 2.86 m/Pa. The Battery, as representative of coastal sea level, was most highly correlated with winds toward 274° with a time lag of approximately 6 h; a linear relationship between The Battery surge and lagged wind stress has a gain of 2.24 m/Pa. One major difference with surge response for the extra-tropical storm is that coastal sea level is correlated with winds directed more in the across-shore direction. An important caveat in comparing these results on surge response for Floyd with those for the 2002 northeaster relates to the fact that Zheng (2006) based her results on MM5 model winds and not observed coastal winds such as those at LaGuardia.

Forecasts of flooding at the scale of municipalities that include the effects of rivers and stormwater management infrastructure require very high spatial resolution and a bathymetry and topography that have been merged to a common datum. The model of Chen et al. (2006), for example, has the capability to resolve complex coastal geometry, allows flooding and drying in grid cells, and can support several different levels of different resolution (grid nesting). Figure 3.43a shows a large domain with variable grid spacing that has very high resolution (~0.25 km) nearshore. Figure 3.43b shows a segment of this grid in high resolution near the eastern end of the Sound. The red point is the location of the New London tide gauge. Note that the grid has been extended over land up to the 30 m contour. This is the coarsest resolution at which inundation can be simulated. All surge models require meteorological forcing and forecasts have errors. Even hindcast fields are uncertain, especially during the major events. These are generally not very accurate during major events like the hurricane of 1938 that devastated much of the eastern Connecticut shoreline.

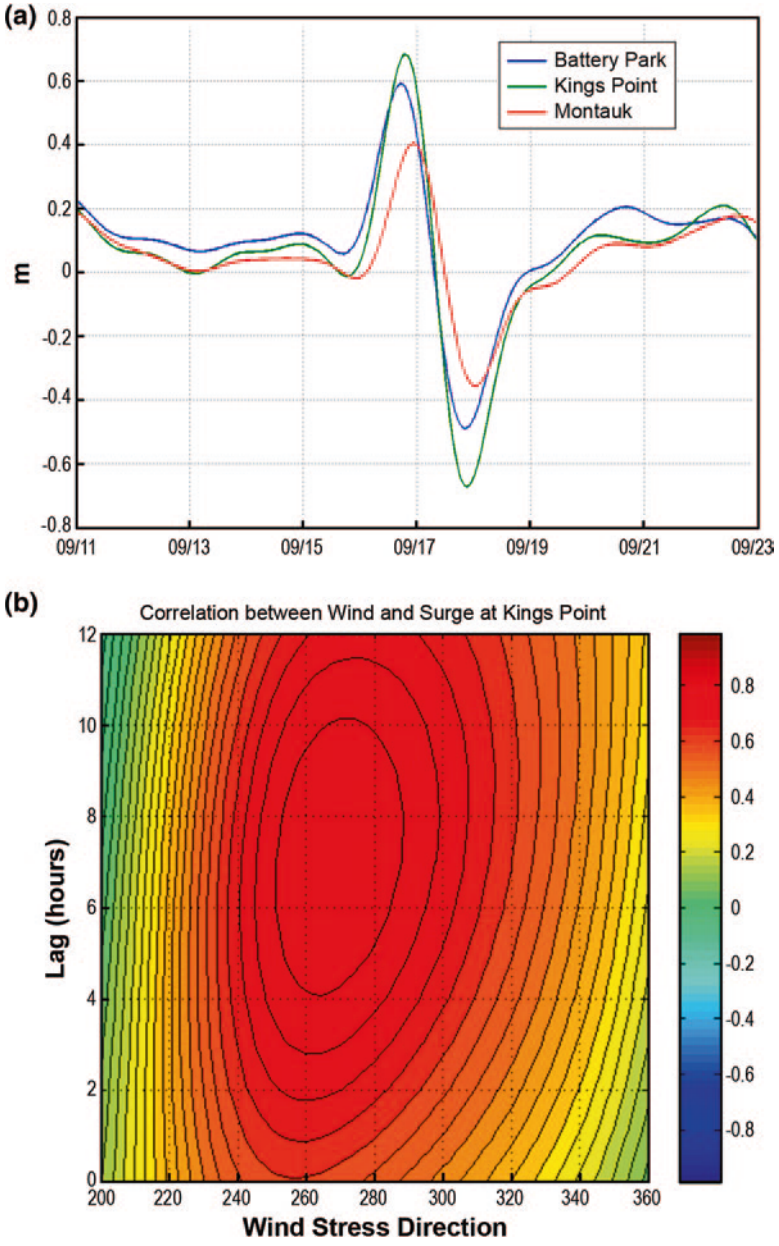

Fig. 3.42 **a** Low-pass filtered sea level at Battery Park, Kings Point and Montauk, NY associated with the storm surge during the passage of Hurricane Floyd (1999) and **b** The correlation between low-pass filtered sea level Kings Point, NY and wind stress estimated from winds at LaGuardia, NY for the storm surge associated with the passage of Hurricane Floyd, September 1999

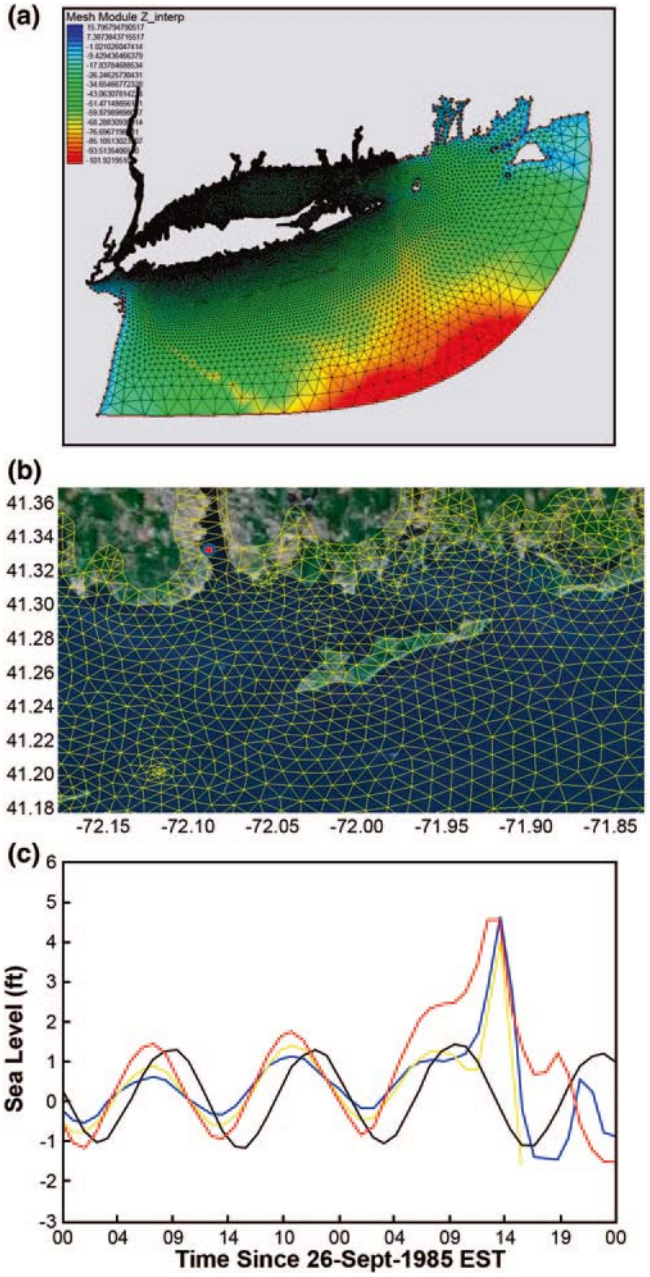

Fig. 3.43 **a** FVCOM model domain and bathymetry. **b** High resolution grid in the eastern Sound. Note the grid extends over land. **c** Sea level observed at New London (*red*), three alternative simulations are shown in *blue*, *black*, and *yellow*

To demonstrate the sensitivity of surge forecasts to the estimate of the wind field and the bathymetry, we compare the results of three simulations to the observations at New London during Hurricane Gloria in September 1985 (Fig. 3.43c). We use the parametric model of Phadke et al. (2003) to represent the wind and pressure field evolution. This allows studies of the sensitivity of solutions to errors in the track, speed, and intensity of the storm. Figure 3.43c, the red line shows the observations of sea level during the storm. The black line shows the solution using the wind field parameterization values suggested by Phadke et al. (2003). This solution produced a substantial error in surge and phase. We then modified the wind field parameters to better match the observations over land and show the sea level solution in yellow. This yielded a much more accurate surge forecast. Further improvement to the model bathymetry resulted in the best peak surge forecast result shown in blue. All three simulations did well in predicting the height of the maximum surge at 4.5 ft. But all had large errors in the evolution of the sea level. This model did not include river flow fluctuations very well and did not have realistic winds. However, diagnosing which of the many weaknesses is the most critical to the improvement of the model skill will require additional high resolution wind and water level measurements during major storm events.

Some important practical aspects of simulating the surge response within LIS have been summarized by Bowman et al. (2005) based on hindcast simulations of surge within the New York metropolitan area to a strong winter northeaster (December 2002) and to Hurricane Floyd. Among these are issues related to the development of high quality topographic and bathymetric databases including the need for:

- seamless transition from bathymetric to topographic datasets
- up-to-date topography and bathymetry
- accurate translation of available bathymetric datasets (NOS, USGS, USACE, and SoMAS) to a common datum (National Geodetic Vertical Data, NGVD)

3.9 Discussion and Conclusions

Physical oceanography is generally used to describe scientific study of the characteristics of waves, currents, and the density distribution in the ocean. These are closely linked to the dynamics and thermodynamics of the atmosphere and, in the coastal ocean, the hydrologic processes in the watershed of the tributaries. A complete description of the structure and variability of currents and water properties requires extensive and frequent sampling since variations occur across scales that range from seconds to decades and microns to hundreds of kilometers. Since this is not practical, we must combine available observations and theoretical models and seek to define the dominant characteristics of the important properties, quantifying the uncertainty in our knowledge.

Wind velocity, wave height, and period observations in the Sound have been measured for more than a decade at a few locations. However, comparison of the

available buoy records at the sites labeled WLIS and CLIS in Fig. 3.3 to those at coastal stations whose records are much longer shows that the seasonal mean vectors are consistent with those over the shelf as summarized by Lentz (2008). The coastal station at Bridgeport, CT (also shown in Fig. 3.3) underestimates the mean over water stress at the WLIS buoy by a factor of two, and by a factor of three at the CLIS buoy. Approximately the same ratios apply to the monthly mean winds. Examination of the frequency spectra of the stress component fluctuations shows that the variance in the along-Sound components is similar at the WLIS and CLIS buoys at all frequencies. However, the across-Sound fluctuations are substantially smaller at the WLIS buoy. The buoy observations allow a first view of the spatial coherence of over water winds. We find that at frequencies higher than approximately 1/day, the winds at the two sites have low coherence and at lower frequencies the coherence is high. This suggests that the local observations will be required in applications in which short time scale meteorological events are important.

Though it is clear that we have not observed the whole range of possible conditions, we present the first statistical summary of long-term observations of buoy measured wave height and period statistics. Using 6 years of data, we show seasonal variation in the probability of exceedance for significant wave heights and periods at the CLIS and WLIS sites. By examining the time series of stress and wave parameters during large events, and the dependence of the differences in the observations of significant wave height at WLIS and CLIS, we find that when the wind is from the east, the wave fields at the two sites are similar. When the winds are from the west, the waves at the CLIS site are much larger. This is validates the idea that waves in LIS are fetch limited as proposed by Bokuniewicz and Gordon (1980b), Signell (2000), and Rivera Lemus (2008).

Sea level fluctuations in LIS due to tides have been well characterized by observations and models. However, there have been few direct current observations with which to evaluate the models. We summarize recent results and since the comparison of observations with simple models show they are not capable of representing the vertical structure, we recommend more detailed evaluations of the predictions of more complex models. Based on analyses of moored hydrographic profiler time series observations and ferry-based current observations, Codiga et al. (2002) and Codiga (2007) have developed strong evidence that straining by tidal currents is active in ELIS. It is, therefore, likely that the relative phase of tidal variations in shear and stratification are important to both horizontal dispersion rates and vertical turbulent diffusion. Bennett et al. (2010) recently reported the existence of large amplitude overtides in the western Sound. These are thought to be due to nonlinear dynamics and replicating the observations will pose a stringent test of the veracity of the simulations.

LIS is an estuary in the sense that it contains seawater that is significantly diluted by the fresh water from rivers. But it is more complex than most estuaries because there are major freshwater sources at each end of the Sound and a mean volume and salt flux through the basin. The Connecticut River enters at the eastern end of the Sound near the connection through which the tide propagates and ocean

water intrudes. The western end is freshened by waters originating in the Hudson River watershed that are transported through New York Harbor to the East River by both natural processes and engineered water systems (WWTFs). We present a view of the seasonal variation in the along-Sound vertical structure of S,T, and density fields based on the data archive developed by the CTDEP survey program (see Kaputa and Olsen 2000). We also show the seasonal variation in vertical stratification and the horizontal baroclinic pressure gradients. The lateral structure is much less well resolved, and we summarize available observations. It appears that the lateral structure can be quite significant, and this needs to be better characterized by observations. Using ferry-based measurements in the eastern Sound where the influence of the Connecticut River discharge is very significant, we highlight the difficulty in observing the structure of the S field in the presence of high gradients and large tidal currents. However, we summarize convincing observational and model evidence that water is persistently fresher in the southern portion of ELIS. In addition, there is evidence that the inflow of brackish water to LIS from the East River is found on the southern side of the Sound.

The nontidal currents in the Sound are also difficult to measure and the data archive is limited. We summarize the available observations and model predictions and provide qualitative comparisons. The three-dimensional models of Blumberg and Pritchard (1997), Crowley (2005), and Hao (2008) have provided estimates of the along-Sound volume fluxes at several across-Sound sections and recent ship survey programs by O'Donnell and Bohlen (2003), Codiga and Aurin (2007), and Bennett (2010) have provided measurements that are generally consistent with the volume flux estimate of the models. However, detailed comparisons remain to be conducted. Gay et al. (2004) inferred exchange rates through The Race at the eastern end of the Sound that turned out to be significantly smaller than those of Codiga and Aurin (2007) at a section a few kilometers to the west. Attention should be paid to resolving this discrepancy through model analyses and additional measurements.

The Codiga and Aurin (2007) measurements from the New London to Orient Point Ferry also provide an estimate of the seasonal variation of the circulation in the eastern Sound and demonstrate a significant increase in the exchange volume flux in the summer. Using a model based on that of Crowley (2005), we provide evidence that there is also seasonal variation in the exchange across the Mattituck Sill that arises from the suppression of vertical friction by thermal stratification, which then allows the intrusion of salty water from the eastern Sound. This further increases stratification, reduces friction, and allows the baroclinic exchange. Near synoptic surveys of the late summer hydrographic structure demonstrate that resolving these mechanisms will require high resolution surveys, and seasonal scale transport fluctuations require persistent observations that resolve the lateral variation. Since the fluxes influence the character of the T and S distributions, they may have substantial influence on ecosystem characteristics.

We summarize the development of our understanding of the fundamental response of the LIS sea level and currents to synoptic period winds. The combination of the direct set-up in the Sound and the Ekman response over the shelf

makes LIS sea level sensitive to winds with a large east component. Recent work by Whitney and Codiga (2011) has described the influence of the bathymetry on the circulation and we summarize their predictions, which include down wind currents in the near surface waters and higher downwind velocities near shore. Near bottom they find upwind currents in the channels. Using conditional averaging of observation from a ferry-mounted current profiler to extract the velocity response in the eastern Sound during strong eastward and westward wind, they found a strong subsurface flow counter to the wind direction. These transient currents may contribute significantly to the mean circulation.

In addition to achieving a more highly resolved view of the temporal and spatial variability of the circulation in LIS, there have also been marked advances in our understanding of the basic seasonal and basin scale features of both hydrography and circulation since the descriptions by Riley (1956). For example, exchange flows that control basin flushing are now understood in light of both models and observations to decrease from approximately 20,000 m^3/s at Orient Point to approximately 10,000 m^3/s at Mattituck Sill, implying substantial re-circulation of waters entering from BIS. Within the central basin west of Mattituck Sill, they remain at approximately 10,000 m^3/s until the vicinity of Hempstead Sill, where they begin to decrease rapidly to less than 2,000 m^3/s in the western narrows. This decrease in exchange flow again implies significant re-circulation of waters entering WLIS from the central basin.

The correlation between increased stratification and the development of hypoxia in the western Sound is well established, and the fundamental DO budget is described by Torgersen et al. (1997). Recently, the buoy observations of O'Donnell et al. (2006 and 2008a, b) revealed synoptic period variations in the near bottom DO concentration in the western Sound that occurred during periods of wind from the northeast. They conjectured that this was a consequence of modification of the rate of restratification by straining of the along-Sound S gradient by the exchange flow through the East River. Wilson et al. (2008) used a sophisticated circulation and mixing model and showed the sensitivity of mean mixing rates to wind directions. We summarize these results and present an analysis of the correlation between wind direction (measured at LaGuardia Airport) and the duration of hypoxia in the western Sound and in the East River. The role of the wind on the straining rate theory remains viable since the orientation of the topography is different at the two locations. New observations in the Chesapeake Bay suggest that lateral winds may play a large role in modulating the seasonal DO trend and we also present results of preliminary model calculations that explore this possibility in LIS. We find a strong response in the S and T field but the effect on the DO budget remains to be assessed.

The availability of long-term datasets now allows an assessment of decadal scale changes in the environment. We summarize the results of several studies including Lee and Lwiza (2005), Gay and O'Donnell (2007 and 2009), Wilson et al. (2008), and Whitney (2010) who examined T and S variations and looked for links to global scale forcing. Wilson et al. (2008) reported that the increase in thermal stratification in the WLIS during summer of between 0.5 and 2 °C between

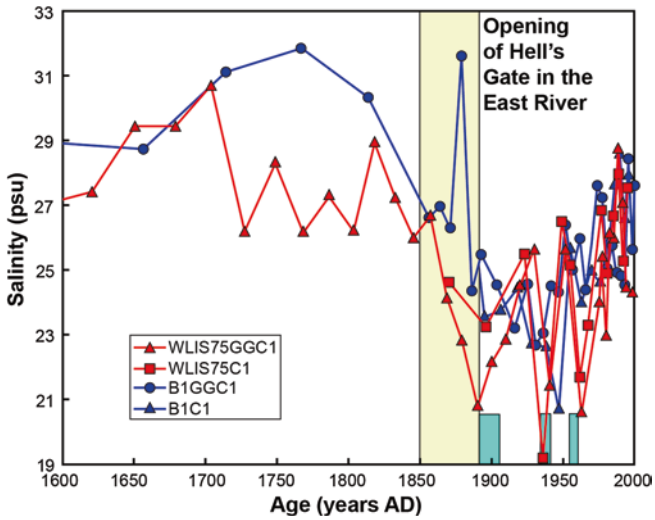

Fig. 3.44 The salinity in western LIS derived from oxygen isotope ratio measurements in shell fossils in cores obtained in western LIS near Execution Rocks

1946 and 2006 was mainly due to the decrease in bottom T (see Fig. 3.38). It is proposed that the bottom T decrease is associated with the change in the wind regime. However, Palle et al. (2006) have analyzed the cloudiness statistics and these show substantial inter-annual variability. The local effects of global changes remain uncertain and additional research is required.

Humans have greatly modified LIS. The development of the water delivery and disposal system for New York City and the surrounding municipalities has diverted water from the Hudson to the East River. Dredging of the Hell Gate in the East River in the late 19th century to make navigation safer is also likely to have increased the exchange with the Hudson and may have changed the S in the Sound. Varekamp (personal communication) has sampled and dated cores obtained near the EXRK buoy (see Fig. 3.3a) in the western Sound and analyzed the oxygen isotope ratio in fossil shells. Since the rate of accumulation of heavy isotopes depends on S, the history of S in the area when the shells were being formed can be inferred. Figure 3.44 shows the time series of "paleosalinity" between 1,600 and 2,000, and there appears to be a large decline between 1,800 and 1,900. While the uncertainty in these estimates is unknown at the moment, it is clearly important to attempt to understand in a quantitative way the impact of historical engineering work on the western Sound.

Currently, coastal development around LIS is very sensitive to severe weather. We summarize the characteristics of storms that influence the region with particular emphasis on sea level set-up and flooding. Colle et al. (2010) have provided a concise summary of observation and have highlighted recent trends in storm character and the impact of even modest sea level rise. Predictions about future flooding require simulation and we summarize some recent work in that area. It is

clear that to make useful forecasts at the scale of individual buildings, circulation models must allow flooding of land, and topography and bathymetry maps must be aligned to a common data and merged. Models must then be tested at these scales and this will require high-resolution sampling in both the atmosphere and ocean.

In all aspects of this review a central theme resonates. Understanding of LIS requires sustained observations and the complementary development of mathematical models. Together these allow the quantitative evaluation of theoretical links between processes and variables, and the development of forecasts.

Acknowledgments We are grateful to the USEPA LIS Office and the LIS Study for motivating this article. During the preparation of the manuscript, the lead author was supported by the US IOOS office through a grant to the Northeast Regional Association of Coastal Ocean Observing Systems (NERACOOS) and the Connecticut Sea Grant College Program. REW acknowledges support from NY Sea Grant LIS project R/CE-30-NYCT.

References

Atallah EH, Bosart LF (2003) The extratropical transition and precipitation distribution of Hurricane Floyd (1999). Monthly Weather Rev 131:163–1881

Beardsley RC, Butman B (1974) Circulation on the New England continental shelf: response to strong winter storms. Geophys Res Lett 1:181–184

Bennett DC (2010) The dynamical circulation of a partially stratified, frictional estuary: Long Island Sound. PhD Dissertation, University of Connecticut, Groton, p 168

Bennett DC, O'Donnell J, Bohlen WF, Houk AE (2010) Tides and overtides in Long Island Sound. J Mar Res 68(1):21–35

Blumberg AF, Pritchard DW (1997) Estimates of the transport through the East River, New York. J Geophys Res 102(C3):5685–5703

Blumberg AF, Khan LA, St. John JP (1999) Three-dimensional hydrodynamic simulations of the New York Harbor, Long Island Sound and the New York Bight. J Hydraulic Eng 125:799–816

Bogden PS, O'Donnell J (1998) Generalized inverse with shipboard current measurements: Tidal and nontidal flows in Long Island Sound. J Mar Res 56(5):995(3)

Bokuniewicz HJ, Gordon RB (1980a) Sediment transport and deposition in Long Island Sound. Adv Geophys 22:69–106

Bokuniewicz HJ, Gordon RB (1980b) Storm and tidal energy in Long Island Sound. Adv Geophys 22:41–67

Bowman MJ, Colle B, Flood R, Hill D, Wilson RE, Buonaiuto F, Cheng P, Zheng Y (2005) Hydrologic feasibility of storm surge barriers to protect the metropolitan New York-New Jersey region. Technical Report, Marine Sciences Research Center, Stony Brook University, Stony Brook, NY, 98 pp

Bretschneider CL (1952) Revised wave forecasting relationships. In: Proceedings of second conference on coastal engineering, Chapter I:1–5

Buxton HT, Smolensky DA (1999) Simulation of the effects of development of the ground-water flow system of Long Island, New York. In: US geological survey water-resources investigations report 98-4069, 57 pp

Chen C, Beardsley RC, Cowles G (2006) An unstructured grid, finite-volume coastal ocean model (FVCOM) system. Oceanography 19(1):78–89

Codiga DL (2007) FOSTER-LIS gridded data products: observed current profiles and near-surface water properties from ferry-based oceanographic sampling in eastern long Island sound. Graduate School of Oceanography, University of Rhode Island, Report 2007–2001,

Narragansett, 14 pp http://www.po.gso.uri.edu/~codiga/foster/files/FOSTERLISGriddedDataProductsMay2007.pdf
Codiga DL, Rear LV (2004) Observed tidal currents outside block Island sound: offshore decay and effects of estuarine outflow. J Geophys Res 109, C07S05. doi:10.1029/2003JC001804
Codiga DL, Aurin DA (2007) Residual circulation in eastern long island sound: observed transverse-vertical structure and exchange transport. Cont Shelf Res 27:103–116
Codiga DL and Ullman DS (2010) Characterizing the physical oceanography of coastal waters off Rhode Island, Part 1: Literature review, available observations, and a representative model simulation. Technical report 2, Appendix to Rhode Island Ocean special area management plan, 169 pp
Codiga DL, Waliser DS, Wilson RE (2002) Observed evolution of vertical profiles of stratification and dissolved oxygen in Long Island Sound. In: Proceedings of the New England estuarine research society/long island sound research Conference Groton, CT, 7–12
Colle BA, Rojowsky K, Buonaiuto F (2010) New York City storm surges: climatology and an analysis of the wind and cyclone evolution. J Appl Meteorol Climatol 49:85–100
Collie JS, Wood AD, Jeffries HP (2008) Long-term shifts in the species composition of a coastal fish community. Can J Fish Aquat Sci 65:1352–1365
Connecticut Department of Environmental Protection (2009) Long Island Sound hypoxia season review 2009. Hartford, 23 pp
Crowley H (2005) The seasonal evolution of thermohaline circulation in Long Island sound. PhD Dissertation, Marine Sciences Research Center, Stony Brook University, Stony Brook, NY, 142 pp
Csanady GT (1973) Wind-induced barotropic motions in long lakes. J Phys Oceanogr 3:429–438
Emery WJ, Thompson RE (1997) Data analysis methods in physical oceanography. Elsevier, San Diego 400
Garvine RW (1974) Physical features of the Connecticut river outflow during high discharge. J Geophys Res 79:831–846
Garvine RW (1975) The distribution of salinity and temperature in the Connecticut river estuary. J Geophys Res 80:1176–1183
Garvine RW (1977) Observations of the motion field of the Connecticut river plume. J Geophys Res 82:441–454
Garvine RW (1985) A simple model of estuarine subtidal fluctuations by local and remote wind stress. J Geophys Res 90(C6):1945–1948
Gay P, O'Donnell J, Edwards CA (2004) Exchange between long Island sound and adjacent waters. J Geophys Res 109:C06017. doi:10.1029/2004JC002319
Gay PS, O'Donnell J (2007) A one-dimensional model of the salt flux in estuaries. J Geophys Res 112:C07021. doi:10.1029/2006JC003840
Gay PS, O'Donnell J (2009) Comparison of the salinity structure of the Chesapeake Bay, the Delaware Bay and long Island sound using a linearly tapered advection-dispersion model. Estuaries Coasts 32:68–87. doi:10.1007/s12237-008-9101-4
Geyer RW, Chant R (2006) The physical oceanography processes in the Hudson River estuary. In: Levinton JS, Waldman JR (eds) The Hudson River Estuary, Cambridge University Press, New York, p 472
Goebel NL, Kremer JN (2007) Temporal and spatial variability of photosynthetic parameters and community respiration in Long Island sound. Mar Ecol Prog Ser 329:23–42
Gordon RB, Pilbeam CC (1975) Circulation in central long island sound. J Geophys Res 80:414–422
Gross MG, Bumpus DF (1972) Residual drift of near bottom waters in long island sound. Limnol and Oceanogr 11:636–638
Hansen DV, Rattray DM (1965) Gravitational circulation in straits and estuaries. J Mar Res 23:104–122
Hao Y (2008) Tidal and residual circulation in Long Island Sound. PhD Dissertation, Marine Sciences Research Center, Stony Brook University, Stony Brook, NY, 70 pp

Hardy CD (1972) Hydrographic data report: long island sound, 1970, Part II. Marine Sciences Research Center, State University of New York, Stony Brook, p 20
Hodgkins GA, Dudley RW, Huntington TG (2003) Changes in the timing of high river flows in New England over the 20th century. J Hydrol 278:244–252
Hollman R, Sandberg GR (1972) The residual drift in eastern long island sound and block island sound. New York Ocean Sci Lab Tech Rept 15, 19 pp
Holt JT, Proctor R (2003) The role of advection in determining the temperature structure of the Irish Sea. J Phys Oceanogr 33:2288–2306
Horsburgh KJ, Hill AE, Brown J, Fernand L, Garvine RW, Angelico MMP (2000) Seasonal evolution of the cold pool gyre in the western Irish Sea. Prog in Oceanogr 46:1–58
Howard-Strobel MM, Bohlen WF, Cohen DR (2006) A year of acoustic doppler current meter observations from central long island sound. In: 8th Biennial Long Island Sound Research Conference Proceedings 2006, pp 26–31
Hurrell JW (1995) Decadal trends in the North Atlantic oscillation regional temperatures and precipitation. Science 269:676–679
Ianniello JP (1977a) Non-linearly induced residual currents in tidally dominated estuaries. PhD Dissertation, The University of Connecticut, 250 pp
Ianniello JP (1977b) Tidally induced residual currents in estuaries of constant breadth and depth. J Mar Res 35(4):755–785
Imberger J, Parker G (1985) Mixed layer dynamics in a lake exposed to a spatially variable wind field. Limnol and Oceanogr 30:473–488
Iriarte A, Purdie DA (2004) Factors controlling the timing of major spring bloom events in an UK south coast estuary. Est Coast Shelf Sci 61:679–690
Isemer H-J, Hasse L (1985) Observations Vol 1. The bunker climate atlas of the North Atlantic Ocean. Springer, London 218
Jay DA, Bowman MJ (1975) The physical oceanography and water quality of New York Harbor and western Long Island Sound. Technical Report 23, Ref # 75-7, Marine Sciences Research Center, State University of New York, Stony Brook
Kaputa NP, Olsen CB (2000) State of Connecticut department of environmental protection, long Island sound ambient water quality monitoring program: summer hypoxia monitoring survey '91-'98 Data Review, CTDEP Bureau of Water Management, 79 Elm Street, Hartford, CT 06106-5127, p 45
Kasai A, Hill AE, Fujiwara T, Simpson JH (2000) Effect of the Earth's rotation on the circulation in regions of freshwater influence. J Geophys Res-Oceans 105:16961–16969
Kenefick AM (1985) Barotropic M2 **tides** and tidal currents in **Long Island** Sound: A numerical model. J Coast Res 1:117–128
Keser M, Swenarton JT, Foertch JF (2005) Effects of thermal input and climate change on growth of Ascophyllum nodosum (Fucales, Phaeophyceae) in eastern Long Island Sound (USA). J Sea Res 54:211–220
Klink K (1999) Climatological mean and interannual variance of United States surface wind speed, direction, and velocity. Int J Climatol 19:471–488
Koppelman LL, Weyl PK, Gross MG (1976) The urban sea: long Island sound. Praeger, New York 223 pp
Krug WR, Gebert WA, Graczyk DJ, Stevens DL, Rochelle BP, Church MR (1990) Map of mean annual runoff for the northeastern, southeastern, and mid-Atlantic United States water years 1951–1980. US Geological Survey Water Resources Investigations Report 88–4094, p. 11
Large WG, Pond S (1981) Open ocean momentum flux measurements in moderate to strong wind. J Phys Oceanogr 11:324–336
Larkin RR, Riley GA (1967) A drift bottle study in long Island sound. Bull Bingham Oceanogr Coll 19:62–71
Lee YJ (2009) Mechanisms controlling variability in Long Island Sound. PhD Dissertation, School of Marine and Atmospheric Sciences, Stony Brook University, New York, 147

Lee YJ, Lwiza K (2005) Interannual variability of temperature and salinity in shallow water: Long Island Sound, New York. J Geophys Res 110 doi:10.1029/2004JC002507
Lee YJ, Lwiza KMM (2008) Characteristics of bottom dissolved oxygen in Long Island Sound, New York. Estuar Coast Shelf Sci 76:187–200 doi:10.1016/j.ecss.2007.07.001
Le Lacheur EA, Sammons JC (1932) Tides and currents in long island and Block Island sounds. US coast and Geodetic survey. Special Publication, 174
Lentz SJ (2008) Seasonal variations in the circulation over the Middle Atlantic Bight continental shelf. J Phys Oceanogr 38:1486–1500
Li CY, O'Donnell J (1997) Tidally driven residual circulation in shallow estuaries with lateral in shallow estuaries with lateral depth variation. J Geophys Res 102:27915–27929
Li C, O'Donnell J (2005) The effect of channel length on the residual circulation in tidally dominated channels. J Phys Oceanogr 35:1826–1840
Mau J-C, Wang D-P, Ullman DS, Codiga DL (2008) Model of the long Island sound outflow: comparison with year-long HF radar and Doppler current observations. Cont Shelf Res 28(14):1791–1799. doi:10.1016/j.csr.2008.04.013
McCardell GM, O'Donnell J (2009) A novel method for estimating vertical eddy diffusivities using diurnal signals with application to western long Island sound. J Mar Syst 77:397–408
McDougall TJ (1987) Neutral surfaces. J Phys Oceanogr 17:1950–1964
Mooers CNK, Fernandez-Partagas J, Price JF (1976) Meteorological forcing fields of the New York Bight. University of Miami (RSMAS) Technical Report TR76-8, Miami, 151 pp
Mountain DG (2003) Variability in the properties of shelf water in the Middle Atlantic Bight, 1977–1999. J Geophys Res Oceans 108(C1):3014
Murphy DL (1979) A numerical investigation into the physical parameters which determine the residual drift in Long Island Sound. PhD Dissertation, Dept of Marine Sciences, The University of Connecticut, 362 pp
O'Donnell J (1997) Observations of near surface currents and hydrography in the Connecticut River plume with the SCUD array. J Geophys Res 102:25021–25033
O'Donnell J, Bohlen WF (2003) The structure and variability of the residual circulation in Long Island sound. Final Report, Connecticut Department of Environmental Protection, Hartford, CT. Grant CWF 325-R, 303 pp (http://www.lisrc.uconn.edu/DataCatalog/DocumentImages/pdf/Odonnell_Bohlen_2003.pdf http://www.lisrc.uconn.edu/DataCatalog/DocumentImages/pdf/Odonnell_Bohlen_2003.pdf)
O'Donnell J, Marmorino GO, Trump CL (1998) Convergence and downwelling at a river plume front. J Phys Oceanogr 28:481–1495
O'Donnell J, Bohlen WF, Dam HG (2006) Wind stress and the ventilation of the hypoxic zone of western Long Island Sound. In: Proceedings of the 8th Biennial Long Island Sound Research Conference, CT Sea Grant Program, New London
O'Donnell J, Dam HG, Bohlen WF, Fitzgerald W, Gay PS, Houk AE, Cohen DC, Howard-Strobel MM (2008) Intermittent ventilation in the hypoxic zone of western Long Island Sound during the summer of 2004. J Geophys Res 113 doi:10.1029/2007JC004716
O'Donnell J, Ackleson SG, Levine ER (2008b) On the spatial scales of a river plume. J Geophys Res-Oceans 113:C04017. doi:10.1029/2007JC004440
O'Donnell J, Morrison J, Mullaney J (2010) The expansion of the Long Island Sound Integrated Coastal Observing System (LISICOS) to the Connecticut River in support of understanding the consequences of climate change. Final Report to the CTDEP, LIS License Plate Fund, 20 pp
Palle E, Goode PR, Montañes-Rodriguez P, Koonin SE (2006) Can Earth's albedo and surface temperatures increase together? EOS Trans 87(4):37
Parker BB (1984) Frictional effects on the tidal dynamics of a shallow estuary. PhD Dissertation, The Johns Hopkins University, 304 pp
Paskausky DF (1976) Seasonal variation of residual drift in Long Island Sound. Est Coast Mar Sci 4:513–522
Pawlowicz R, Beardsley B, Lentz S (2002) Classical tidal harmonic analysis including error estimates in MATLAB using t_tide. Comput Geosci 28:929–937

Phadke AC, Martino CD, Cheung KF, Houston SH (2003) Modeling of tropical cyclone winds and waves for emergency management. Ocean Eng 30(4):553–578
Pritchard DF (1956) The dynamic structure of a coastal plain estuary. J Mar Res 1:33–44
Redfield AE (1950) The analysis of tidal phenomena in narrow embayments. Pap Phys Oceanogr Meteorol XI(4):36
Riley GA (1952) Hydrography of the long island and Block Island sounds. Bull of the Bingham Oceanographic Collection 13, Article 3, Peabody Museum of Natural History, Yale University, New Haven
Riley GA (1956) Oceanography of Long Island Sound: 1952–1954. II. Phys Oceanogr Bull of the Bingham Oceanographic Collection 15, Peabody Museum of Natural History, Yale University, New Haven
Rivera Lemus ER (2008) Wind waves in central Long Island Sound: a comparison of observations to an analytical expression. Masters Dissertation, Department of Marine Sciences, The University of Connecticut, 77 pp
Scully ME (2010a) The importance of climate variability to wind-driven modulation of hypoxia in Chesapeake Bay. J Phys Oceanogr 40:1435–1440
Scully ME (2010b) Wind modulation of dissolved oxygen in Chesapeake Bay. Estuaries Coasts 33:1164–1175
Scully M, Friedrichs C, Brubaker J (2005) Control of estuarine stratification and mixing by wind-induced straining of the estuarine density field. Estuaries 28(3):321–326. doi:10.1007/BF02693915
Schmalz RA (1993) Numerical decomposition of Eulerian circulation in long island sound. In: Proceedings of the 3rd International Estuarine and Coastal Modeling Conference. ASCE, Chicago, pp 294–308
Shchepetkin AF, McWilliams JC (2005) Regional ocean model system: a split-explicit ocean model with a free-surface and topography-following vertical coordinate. Ocean Model 9:347–404
Signell R, List J, Farris A (2000) Bottom currents and sediment transport in Long Island Sound: a modeling study. J Coast Res 16:551–566
Simpson JH, Brown J, Matthews JP, Allen G (1990) Tidal straining, density currents and stirring in the control of estuarine stratification. Estuaries 12:129–132
Soulsby RL (1990) Tidal-current boundary layers. In: Le Mehaute B, Hanes DM (eds) The sea, ocean engineering science 9A. Wiley-Interscience, New York, pp 523–566
Stachowicz JJ, Terwin JR, Whitlatch RB, Osman RW (2002) Linking climate change and biological invasions: Ocean warming facilitates nonindigenous species invasions. Proc Nat Acad Sci US Am 99(24):15497–15500
Sverdrup HU, Monk WH (1946) Empirical and theoretical relations between wind, sea and swell. Trans Am Geophys Union 27(6):828–836
Swanson RL (1976) Tides. MESA New York Bight Atlas Monograph, 4, New York Sea Grant Institute, Albany, pp 34
Torgersen T, DeAngelo E, O'Donnell J (1997) Calculations of horizontal mixing rates using 222Rn and the controls on hypoxia in western Long Island Sound. Estuaries 20:328–343
Townsend DW, Cammen L, Holligan PM, Campbell DE, Pettigrew NR (1994) Causes and consequences of variability in the timing of spring phytoplankton blooms. Deep Sea Res I 41:747–765
Ullman DS, DL Codiga DL (2010) Characterizing the physical oceanography of coastal waters off Rhode Island, Part 2: New observations of water properties, currents, and waves. Technical Report 3, Appendix to Rhode Island Ocean Special Area Management Plan, 108 pp
Ullman DS, Wilson RE (1984) Subinertial current oscillations in western Long Island Sound. J Geophys Res 89:10,579–10,587
Valle-Levinson A (2008) Density-driven exchange flow in terms of the Kelvin and Ekman numbers. J Geophys Res 113:C04001. doi:10.1029/2007JC004144

Valle-Levinson A, Wilson RE (1994a) Effects of sill bathymetry, oscillating barotropic forcing and vertical mixing on estuary ocean exchange, J Geophys Res 99 (C3):5194–5169
Valle-Levinson A, Wilson RE (1994b) Effects of sill processes and tidal forcing on exchange in eastern Long Island Sound. J Geophys Res 99 (C6):12667–12681
Valle-Levinson A, Wilson RE, Swanson RL (1995) Physical mechanisms leading to hypoxia and anoxia in western Long Island Sound. Environ Int 21(5):657–666
Valle-Levinson A, Wilson RE (1998) Rotation and vertical mixing effects on volume exchange in eastern Long Island Sound. Estuarine Costal and Shelf Science 46:573–585
Valle-Levinson A, Reyes C, Sanay R (2003) Effects of bathymetry, friction, and rotation on estuary-ocean exchange. J Phys Oceanogr 33:2375–2393
Vieira MEC (2000) The long-term residual circulation in Long Island Sound. Estuaries 23(2):199–207
Wang YH, Bohlen WF, O'Donnell J (2000) Storm enhanced bottom shear stress and associated sediment entrainment in a moderate energetic estuary. J Oceanogr 56:311–317
Welsh BL, Eller FC (1991) Mechanisms controlling summertime oxygen depletion in western Long Island Sound. Estuaries 14:265–278
Whitney MM (2010) A study on river discharge and salinity variability in the Middle Atlantic Bight and Long Island Sound. Cont Shelf Res 30:305–318
Whitney MM, Codiga DL (2011) Response of a large stratified estuary to wind events: Observations, simulations, and theory for Long Island Sound. J Phys Oceanogr 41:1308–1327
Wilkin JL, Bowen MM, Emery WJ (2002) Mapping mesoscale currents by optimal interpolation of satellite radiometer and altimeter data. Ocean Dyn 52:95–103
Wilson RE (1976) Gravitational circulation in Long Island Sound. Estuar Coast Mar Sci 4:443–453
Wilson RE, Swanson RL (2005) A perspective on bottom water temperature anomalies in Long Island Sound during the 1999 Lobster Mortality event. J Shellfish Res 24:825–830
Wilson RE, Crowley HA, Brownawell BJ, Swanson RL (2005) Simulation of transient pesticide concentrations in Long Island Sound for late summer 1999 with a high resolution coastal circulation model. J Shellfish Res 24:865–875
Wilson RE, Swanson RL, Crowley HA (2008) Perspectives on long-term variations in hypoxic conditions in western Long Island Sound. J Geophys Res 113:C12011. doi:10.1029/2007JC004693
Winant CD (2004) Three-dimensional wind-driven flow in an elongated, rotating basin. J Phys Oceanogr 34:462–476
Winant CD (2007) Three-dimensional tidal flow in an elongated, rotating basin. J Phys Oceanogr 37:2345–2362
Wong K-C (1990) Sea level variability in Long Island Sound. Estuaries 13:362–372
Wong K-C (1991) The effect of the East River on the barotropic motions in Long Island sound. J Mar Res 49:321–337
Wong K-C (1994) On the nature of transverse variability in a coastal plain estuary. J Geophys Res 99:14209–14222
Wunsch C (2006) Discrete inverse and state estimation problems with geophysical fluid applications. Cambridge University Press, Cambridge 371
Zhang K, Douglas BR, Leatherman SP (2000) Twentieth-century storm activity along the US East Coast. J Climate 13:1748–1761
Zheng Y (2006) Diagnosis of extra-tropical storm surge response in New York Harbor. Masters Dissertation, Marine Sciences Research Center, Stony Brook University, Stony Brook, 84 pp

View publication stats